Computer-Aided Process Planning for Extrusion-based Additive Manufacturing of Concrete

A thesis submitted

in partial fulfillment of the requirements

for the degree of

Doctor of Philosophy

by

Akshay Sahu

(206103103)

Under the Supervision of

Dr. Biranchi Panda

Department of Mechanical Engineering

Indian Institute of Technology Guwahati

Guwahati - 781039, Assam, India

January 2026

Department of Mechanical Engineering
Indian Institute of Technology Guwahati
Guwahati 781039, Assam, India

Certificate

This is to certify that the work presented in the thesis entitled ***"Computer-Aided Process Planning for Extrusion-based Additive Manufacturing of Concrete"***, submitted by **Akshay Sahu** (Roll No. 206103103), to the Indian Institute of Technology Guwahati for the award of the degree of **Doctor of Philosophy**, has been carried out under my supervision in the Department of Mechanical Engineering, Indian Institute of Technology Guwahati.

I further certify that this work has not been submitted elsewhere, in part or in full, for the award of any other degree or diploma.

Date: 19/03/2026

Dr. Biranchi Panda

Department of Mechanical Engineering

Indian Institute of Technology Guwahati

Guwahati-781039, Assam, India

Declaration

I hereby declare that this thesis is the outcome of my own work carried out under the guidance of my supervisor. The content of this submission represents my ideas expressed in my own words, and wherever I have used ideas, results, or words of others, due credit has been given through proper citation and referencing. I affirm that I have maintained academic honesty and integrity throughout the preparation of this thesis, and I have not fabricated, falsified, misrepresented, or plagiarized any idea, data, fact, or source. I further understand that any violation of the above principles may invite disciplinary action from the institute and, where applicable, legal consequences from the original authors or copyright holders if proper permission has not been obtained.

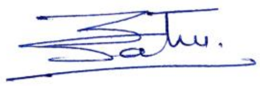

Date: 19/03/2026

Akshay Sahu

Roll No: 206103103

Dedicated to

Shiv & Shakti, My Teachers and Parents

Acknowledgement

I would like to take this opportunity to express my profound respect and sincere gratitude to my supervisor, ***Dr. Biranchi Panda***, Department of Mechanical Engineering, Indian Institute of Technology Guwahati, for his invaluable advice, resourceful guidance, inspiring instructions, active supervision, and constant encouragement, without which it would not have been possible for me to reach this stage of my research journey.

I extend my heartfelt thanks to my doctoral committee members from IIT Guwahati, India, ***Prof. Shrikrishna Nandkishor Joshi***, ***Prof. Subashisa Dutta***, and ***Dr. Sajan Kapil***, for their constructive feedback, moral support, and encouragement of my ideas in both my research and other innovative endeavors.

I also thank ***Prof. Deepak Sharma,*** IIT Guwahati, India, for his invaluable guidance on Finite Element Analysis and for collaborating with me on this work.

I express my sincere gratitude to ***Prof. Adewumi John Babafemi***, Stellenbosch University, South Africa, and ***Prof. Janakarajan Ramkumar***, IIT Kanpur, India, for serving as thesis examiners and for their valuable insights, constructive feedback, and suggestions that greatly enhanced the quality of this thesis.

I gratefully acknowledge *Dr. Dodda Srinivas*, *Dr. Dhrutiman Dey, Mr. Shubham Maurya, Mr. Lalit Kumar,* and *Mr. Sujit Rajbhar* from the SReAM Lab for their continued assistance in resolving material, machines, and simulation-related challenges. I am sincerely grateful to *Dr. Ambrish Singh*, *Mr. Kanak Jindal, and Mr. Ch. Kapil Ror* from the Fabrication Lab, Department of Mechanical Engineering, IIT Guwahati, for their valuable assistance with the travelling salesman problem and non-planar analysis work. I thank the Product Development Lab assistants, *Ms. Priya Kemprai* & *Ms. Ashima Medhi*, for their assistance.

I am deeply grateful to *Mr. Subhojit Jash* and *Mr. Darshan Dange* for their kind support, thoughtful guidance, and many constructive discussions that helped me navigate several research-related challenges along this journey.

I am truly thankful to my friends — *Ms. Shruti Agrawal, Mr. Shubham Sahu, Mr. Mayank Wagdre, Mr. Nikhil Bedre, Mr. Rahul Suryawanshi, Mr. Manish Gawande, Mr. Harshit Soni, Mr. Lalit Nirmale, Mr. Himanshu Gupta, Mr. Akash Pawar, Ms. Bhavika Sakre, Mr. Pankaj Singh, Mrs. Pragya Thakre Deshmukh, Ms. Arti Jhade, Mrs. Nikita Sarawagi Aggarwal, Mr. Yash Kushwah, Dr. Kokila Verma Gour, Mrs. Mahima Dhote, Mr. Vishal Nagle, Mr. Akshay Jhod, Mr. Akshay Pawar, Mr. Mahesh Pawar, Mr. Satyendra Prajapati, Mrs. Syeda Mariya Eram, Mrs. Yojana Chadokar, Ms. Shreya Agrawal, Mr. Shantanu Vyas,* and *Ms. Tejal Agrawal* for their friendship, laughter, encouragement, and motivation, which made this long and demanding journey lighter and more meaningful. I am equally grateful to all other friends who stood by me in their own ways during this time.

I would also like to sincerely thank my institutional friends and colleagues — Mr. Rakesh Panda, Mr. Ramalingaiah Boda, Mr. Bhanu Prakash Bonthala, Mr. Avinash Chetry, Dr. Lipika Boruah, Mrs. Nilanjana Chowdhury Jash, Ms. Puspanjali Ghoshal, Mr. Lakshmi Vara Prasad, Ms. Syed Bustan Fatima Warsi, Ms. Palak Kaushik, Mr. Amit Kumar Chaurasiya, Mr. Jagannath Verma, Mr. Deepak Rathor, Ms. Antara Sarkar, Mr. Suraj Kumar, Mr. Deep Arya, Mr. Praveen Chauhan, Mr. Kishor Kumar Nath, and others—who were not only colleagues but also friends, confidants, and, at times, my therapists. Their support, conversations, humor, and empathy helped me stay grounded and resilient throughout this journey.

I would also like to express my sincere gratitude to *Ms. Vaishnavi Vyas* for her constant encouragement, understanding, and unwavering support, which meant more to me than words can express.

My heartfelt thanks also go to my grandfather, *Dr. B. D. Sahu*; my uncles, *Mr. Adarsh Sahu, and Mr. Sanjay Sahu;* my aunts, *Mrs. Chaya Sahu, and Mrs. Seema Sahu;* and my brother, *Mr. Vinay Sahu,* for their constant faith in me throughout my PhD journey. I would like to thank all the relatives who supported me during this period.

I would also like to express my gratitude to my wonderful cousins — *Mr. Kunal Sahu, Mrs. Shilpa Rahul Sahu, Ms. Shaily Sahu, Ms. Ashi Sahu, Mr. Satyam Sahu, Ms. Riyashri Sahu, Mr. Anchal Sahu, Mr. Deshmukh Sahu, Mr. Bhoopendra Sahu, Mrs. Vaishali Satyam Sahu, Mr. Rishi Sahu, Mr. Ashutosh Sahu,* and *Mr. Harshit Sahu*—for their constant support and for bringing so much fun and happiness into my life.

I would like to express my deepest gratitude to my sister*; Mrs. Aakanksha Sahu Golhani,* and brother-in-law*; Mr. Sandeep Golhani* for their unwavering love and support. My heartfelt thanks to my adorable niece, *Iksha*, and my nephew, *Ikshit*, whose love and enthusiasm have been a constant source of motivation for me.

I am sincerely grateful to ***Mr. Motilal Kushwah*** *(Acharya Ji),* ***Mr. Dinesh Kudbe*** *(Sir)*, and all my teachers for their invaluable guidance and encouragement since my childhood.

Above all, I owe my deepest appreciation to my ***Mother (Smt. Rekha Sahu)***, whose immeasurable sacrifices have made it possible for me to pursue my dreams. I also remember my ***Father (Shri Jairam Sahu)*** with love and respect, whose blessings and memories continue to inspire me on this journey.

Akshay Sahu

Abstract

Additive Manufacturing of Concrete (AMoC), also referred to as 3D concrete printing, is revolutionizing construction through layer-by-layer fabrication, enabling the creation of complex, customized geometries with reduced material use and construction time. Its advantages—geometric freedom, design flexibility, and tunable mechanical properties—have attracted attention across industries such as architecture, construction, and aerospace. AMoC employs gantry, robotic, and hybrid extrusion systems for large-scale construction, yet its widespread implementation remains limited by toolpath discontinuity, material rheology challenges, and lack of design standardization. Effective process planning—specifically toolpath generation—is essential to achieving high-quality printed concrete components. Toolpath design directly affects geometric accuracy, print continuity, and interlayer bonding, which influences the overall structural integrity and sustainability of printed parts. Unlike polymer or metal AM, there is a critical need for the development of Computer-Aided Process Planning (CAPP) systems specific to extrusion-based concrete printing. The main objective of this research is three-fold: (1) Development of systematic Design for Additive Manufacturing of Concrete (DfAMoC) framework—integrating design and manufacturing principles for contour-based toolpath generation, (2) Utilization of Travelling Salesman Problem (TSP) solver for generating continuous toolpath strategy to improve path continuity, isotropy, and printing efficiency in AMoC (3) Development of a growth curve-based printing path planning method that optimizes part strength, quality, scalability, computational efficiency, and further extending this approach to non-planar area filling addressing curved and complex geometries.

Firstly, DfAMoC framework is explored that integrates three design and two manufacturing principles: surface offsetting (half-bead width) to ensure dimensional accuracy, functional surface design defining overhang limits and print heights to prevent collapse, sharp junction elimination using a 2 mm fillet radius to minimize nozzle jerks and clogging, orientation and modularity to enhance scalability and continuity, and "As Continuous As Possible" (ACAP) toolpaths to reduce nozzle lifts and printing interruptions. Experiments on planar, non-planar, and embossed/debossed geometries demonstrated superior accuracy (±6 mm deviation) and improved interlayer bond strength (1.42–1.52 MPa). The DfAMoC workflow also surpassed commercial slicers (Cura, Simplify3D) in terms of surface finish, print continuity, and dimensional precision.

Secondly, a Traveling Salesman Problem (TSP)-based approach was implemented to generate optimized continuous toolpaths for solid area filling. The workflow involves contour offsetting, grid generation, and TSP optimization using the Lin–Kernighan–Helsgaun algorithm, followed by boundary trimming and smooth curve fitting. Experimental validation on geometries such as square, rhino, human face, chair, and bridge using a gantry-based printer with a 20 mm nozzle confirmed only one discontinuity per layer (compared to 20-118 in conventional paths), a reduction in printing time by up to 60%, underfilling reduced by 72–93%, improved isotropy by about 30–42%, and scalability up to 600% with maintained quality. The TSP-based method provided a robust, material-aware planning strategy suitable for large-scale, topology-optimized concrete structures.

To overcome the computational limitations of TSP, a growth curve-based continuous toolpath algorithm was developed. It iteratively grows a user-defined input curve inside a target area following a growth function, maintaining constant spacing and avoiding path crossings, producing a fully continuous Hamiltonian-like circuit. Parametric analyses revealed that a step-over of 20 mm reduced print time by 40–50% while maintaining less than 1.5% underfilling, scaling had minimal impact on quality, and a growth factor of 2 minimized computation time with excellent print quality. Analytical and experimental validation across numerous geometries demonstrates the method's scalability, robustness, and adaptability. The CAPP system achieves optimized toolpath by carefully adjusting important parameters, particularly step-over and growth factor, which reduces printing time, minimizes sharp turns, eliminates unnecessary interruptions, improves print quality (underfilling <0.015, overlapping <0.03), and computation efficiency.

The feasibility of non-planar fabrication using the growth curve toolpath was demonstrated using sand–sodium silicate support beds, shaped and cured with CO_2. Various surfaces (cylindrical concave, convex, and complex coral-like forms) were printed successfully. Dimensional analysis using laser scanning revealed mean deviations of –0.43 mm for the sand bed and +0.65 mm for printed parts, with overall deviations within ±6 mm—acceptable for AMoC applications, particularly for bio-inspired architectural structures. These results demonstrate the successful printing of functional curved structures using the proposed CAPP system along with recyclable, reusable materials.

Table of Contents

List of Figures

List of Tables

Nomenclature

S_o	Surface offset
w	Bead width
s	Step-over
r	Radius
β	Reduction factor
α	Reduction factor
Ø	Azimuthal
d	Spillage
I_{3D}	Anisotropic coefficient
I_X	Anisotropic coefficient in X-direction
I_Y	Anisotropic coefficient in Y-direction
I_Z	Anisotropic coefficient in Z-direction
f_X	Force in X-direction
f_Y	Force in Y-direction
f_Z	Force in Z-direction
A	Actual area
L	Length of the toolpath
A_T	Target area
$R(t)$	Growth function
G	Growth factor
t	Number of iterations
N	Number of segments
l	Segment length
A_{Gc}	Area filled by growth curve
d_i	Infill density
N_d	Necessary Segments based on infill density

Acronyms

3D	Three Dimensional
3DCP	3D Concrete Printing
ACAP	As Continuous As Possible
AM	Additive Manufacturing
AMoC	Additive Manufacturing of Concrete
ASTM	American Society for Testing and Materials
CAD	Computer-Aided Design
CAPP	Computer-Aided Process Planning
CC	Contour Crafting
C.G.A.D.	Circular Grid Azimuthal Direction
C.G.R.D.	Circular Grid Radial Direction
DfAM	Design for Additive Manufacturing
DfAMoC	Design for Additive Manufacturing of Concrete
DfMA	Design for Manufacturing and Assembly
DfX	Design for Excellence
FDM	Fused Deposition Modelling
LK	Lin-Kernighan
LKH	Lin-Kernighan-Helsgaun
R.G.H.D.	Rectangular Grid Horizontal Direction
R.G.V.D.	Rectangular Grid Vertical Direction
STL	STereoLithography
TSP	Travelling Salesman Problem

Chapter 1: Introduction and Literature Review

This chapter introduces the motivation, scope, and objectives of the research. It also provides a comprehensive literature review on digital construction methods, with a focus on AMoC. Key aspects of design for AMoC, including area-filling strategies and continuous toolpath generation for planar and non-planar applications, are critically examined to highlight existing gaps and define the research directions pursued in this work.

Additive Manufacturing (AM) has transformed traditional manufacturing processes by employing a generative approach. In contrast to subtractive manufacturing, which removes material from a workpiece to get the desired form, AM involves selecting and strategically adding material layer by layer to build the finished component. Originally designed for quick prototyping, AM has grown into a full manufacturing process capable of series production of operational components (Foust et al., 2012; Murr et al., 2010). ASTM (American Society for Testing and Materials) ISO/ASTM 52900 classifies AM methods into seven categories. However, these categories are broad terms that cover different variations of each technique. AM covers a variety of processes; each adapted to specific applications and material needs.

Additive Manufacturing of Concrete (AMoC), also called 3D concrete printing (3DCP), is an extrusion-based AM process, enabling the creation of complex architectural concrete forms through incremental fabrication directly from Computer-Aided Design (CAD) model. Compared to traditional manufacturing methods, AM allows for greater design flexibility and yields tunable mechanical properties without the need of molds/ formwork (Gibson et al., 2021). Consequently, it has garnered significant attention in diverse fields, including automotive (Leal et al., 2017), biomedical (Gonçalves et al., 2017), architecture (Pajonk et al., 2021), construction (Anton et al., 2021; Mechtcherine et al., 2019), and aerospace (Blakey-Milner et al., 2021; Steuben et al., 2016).

1.1. AMoC for infrastructure and construction

Historically, the construction industry has relied on traditional methods that are time-consuming, resource-intensive, and often rigid when faced with intricate design specifications. For example, formwork, scaffolding, and a large crew are essential for traditional concrete building, particularly for casting, placing, and finishing (Mechtcherine et al., 2020). An estimated 10–40% of the total project cost is attributed to formwork alone (Shin et al., 2012; Sai & Aravindan, 2020) and the cost further exacerbated when projects include highly customized or architecturally unique designs requiring complex molds.

Several fabrication techniques have been explored for producing complex concrete geometries, including conventional cast-in-place construction, precast modular systems, slip-forming, and CNC-milled formwork. While these methods are mature and structurally reliable, they are inherently constrained by formwork dependency, high labor intensity, geometric rigidity, and significant material wastage. For example, complex freeform concrete construction using CNC-milled formwork typically results in 30–60% additional material consumption due to the use of disposable molds, whereas precast modular approaches often require geometric simplification and extensive post-processing, which increases assembly time and cost (Lowke et al., 2024; Liu et al., 2022; Mata Falcon et al., 2023). Quantitatively, AMoC has been shown to achieve material savings of 20–50% through optimized topology (Lin et al., 2025) and controlled deposition, alongside construction time reductions of 30–70% (Buswell et al., 2018; Lin et al., 2025) by eliminating formwork fabrication and manual placement steps. Furthermore, the ability to control bead placement and infill density enables the functional distribution of materials, which is difficult to achieve using subtractive or mold-based techniques (Dey et al., 2023).

In contrast to traditional techniques, AMoC eliminates the requirement for formwork, which saves labour cost and materials while enabling design flexibility in terms of freeform geometry (Bi et al, 2022). The potential of AMoC in printing complex freeform facades, housing prototypes, and pedestrian bridges has also been as shown in a few academia projects in Europe and Asia (Leschok et al., 2023; Takva et al., 2024; 3D printed bridge, 2016). The digitalization of the construction process via AM combines fabrication, simulation, and computational design into a single framework, (Hernández Vargas, 2023; Zhang & Sanjayan, 2025) that enhances overall sustainability of AMoC structures (Vantyghem et al., 2020; Breseghello & Naboni, 2022; Bi et al., 2022). The advantages of the AMoC process are illustrated in *Figure 1.1*.

(a) and (b) Examples of Freeform structures (Vertico, 2023; Architizer, 2024)

(c) Framework free construction (XtreeE, 2017)

(d) Sustainable Additively manufactured structure (Hyperion robotics, 2021)

Figure 1.1 Advantages of additive manufacturing of concrete

Compared to traditional construction, AMoC has some drawbacks in terms of printable material requirement, variable interlayer bonding, the integration of reinforcement, ability to scale to multi-story buildings, and building code provisions (Ambily et al., 2024; Lin et al., 2025). These challenges are now being addressed by continued research and development via development of hybrid reinforcing techniques, printable concrete combinations, and testing guidelines (Gamage et al., 2024; Zaid & El Ouni, 2024).

1.2. Classification of extrusion-based AMoC

AMoC has garnered worldwide attention as a revolutionary construction technology that has the potential to address the long-standing challenges of formwork dependency, high labor demand, and material waste in conventional construction. Extrusion-based approaches have proven to be the most mature, scalable, and industrially applicable among the various process families in digital construction. Within the larger extrusion category, two major domains of development can be identified, i.e. Contour Crafting (CC) originated in the United States and 3D Concrete Printing (3DCP). While they both use the same core principle of layering fresh cementitious material, their design philosophies, technological implementations, and application regions differ significantly. Understanding this classification is crucial for assessing the progress of extrusion-based AMoC and coordinating future research and industrial adoption. *Figure 1.2* illustrates the shared characteristics among three construction technologies: Concrete Printing, Contour Crafting, and d-Shape. The central overlap shows that all three are additive manufacturing processes. The diagram further details specific shared traits between pairs: 3DCP and CC both fall under extrusion-based AMoC.

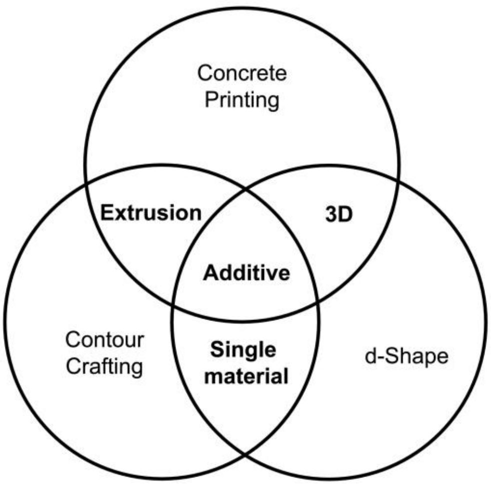

Figure 1.2 Similarities between different AMoC processes (Buswell et al., 2020).

1.2.1. Contour crafting (CC)

Behrokh Khoshnevis and his team at the University of Southern California pioneered and developed CC in the early 2000s (Khoshnevis, 2004; Hwang & Khoshnevis, 2005). It was designed primarily as a construction automation system for manufacturing large-scale housing and infrastructure components on-site. The incorporation of troweling mechanisms beside the extrusion nozzle is what sets CC apart. As layers of cementitious material are produced, a robotic trowel smooths the surfaces, eliminating the staircase effect characteristic of AM processes. This method enables the rapid production of vertical parts with smooth walls and minimal post-processing requirements. *Figure 1.3* shows the CC process.

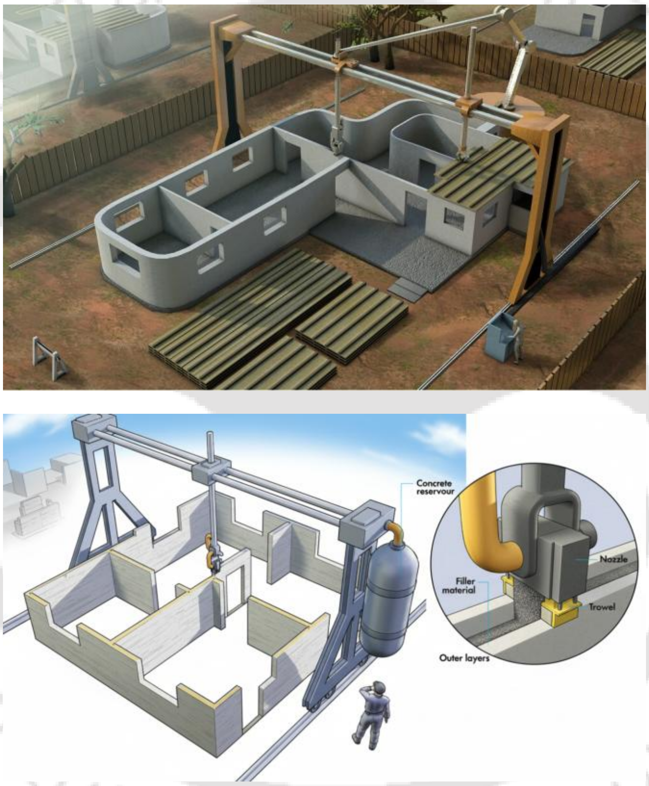

(a)

(b)

Figure 1.3 (a), and (b) Contour crafting technology (Khoshnevis, 2004)

From a material standpoint, CC often uses mortar- or clay-like mixes with rheological qualities optimized for shape retention and quick build-up. The emphasis is not always on precise geometric detailing, but rather on maintaining adequate green strength to support succeeding layers at a rapid deposition rate. Unlike other methods, CC prioritizes large bead widths and thicker layer heights to maximize speed, enabling the rapid processing of large amounts of material. This feature makes CC appropriate for full-scale printing of monolithic walls, shells, and other structural components (Zhang, 2009). The applications of CC have been focused on automated housing solutions, rapid shelter construction, and infrastructure. Demonstrations have shown that entire wall systems and even complete housing units can be printed in a short period of time (Khoshnevis et al., 2006). However, CC is not suitable for freeform parts or highly detailed architectural components and reinforcing techniques are also challenging in this process.

1.2.2. 3D concrete printing (3DCP)

3DCP is an AMoC method that emphasizes precision material extrusion and design freedom, initially studied at Loughborough University, United Kingdom (Buswell et al., 2005).

3DCP is distinguished by its ability to construct a variety of internal structures, including those beyond monolithic walls. The extrusion process can be configured to produce solid components, contoured components, lattice structures, curved layer components, and topology-optimized designs, as illustrated in *Figure 1.4.*

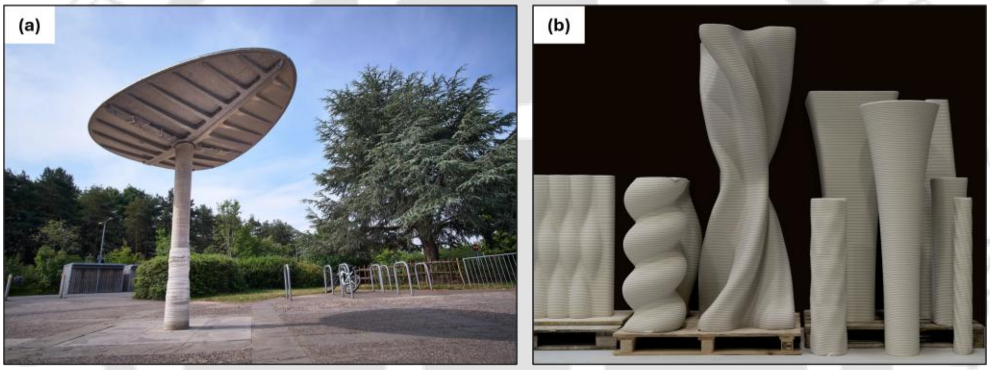

(a) Solid component, A canopy (Loughborough University, 2025) (b) Contoured components (Sika Groups, 2025)

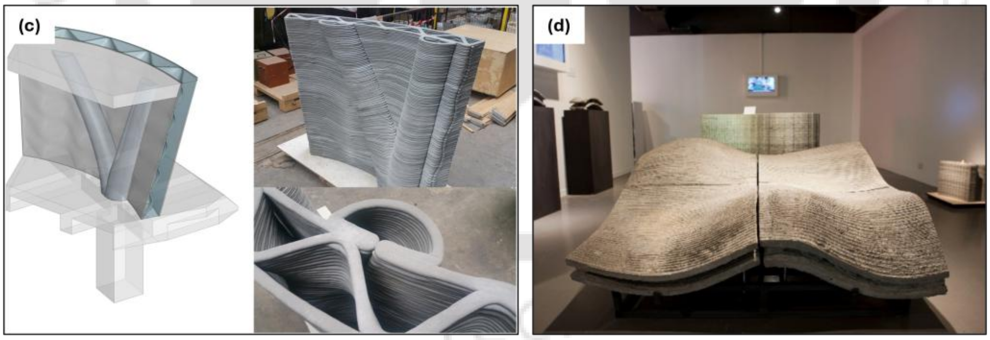

(c) Lattice wall (Gosselin et al., 2016) (d) Curved component (Loughborough University, 2011)

(e) Topology optimized bridge (Vantyghem et al., 2020)

Figure 1.4 Application of the 3DCP process

This adaptability enables weight reduction, material savings, and functional customization within a single manufacturing process. Designers can modify structural performance, thermal insulation, and even the acoustic behavior of printed pieces by adjusting the infill density and pattern, thereby eliminating the need for formwork or secondary operations.

The 3DCP systems have undergone significant advancements in terms of hardware. Different configurations are currently available: gantry-based systems offer large, rectangular build volumes that are ideal for structural components; multi-axis robotic arms enable more complex and freeform deposition paths; delta systems provide high-speed printing with less mechanical mass; and hybrid systems, like robotic arms mounted on gantries, combine the geometric freedom of robotics with the scalability of gantries. The different configurations of machines used in 3DCP are shown in *Figure 1.5*.

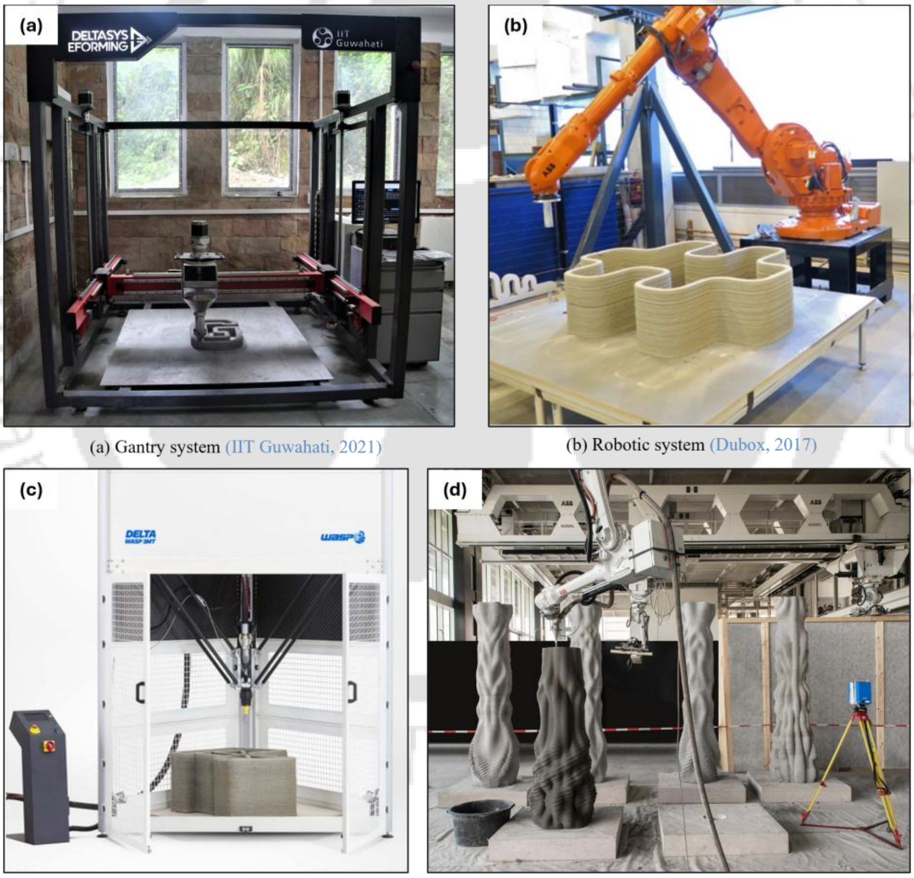

(a) Gantry system (IIT Guwahati, 2021) (b) Robotic system (Dubox, 2017)

(c) Delta system (3DWASP, 2020) (d) Hybrid system (ETH Zurich , 2019)

Figure 1.5 Different configurations of machines used in AMoC

In concrete printing, extrusion is typically achieved using progressive cavity pumps or screw-driven extruders. Screw extruders work well with mixtures that have higher viscosity because they offer fine control over flow and high pressure. They reduce the likelihood of blockages and dead zones by minimizing consolidation and phase separation (Chen et al., 2023).

Conversely, progressive cavity pumps provide a smoother, continuous flow and are more suitable for materials that require gentle handling to retain their workability (Sevcik et al., 2024). The mortar's rheology and the intended balance between flow stability and deposition precision are the primary determinants of the system selection. Due to its emphasis on digital control, 3DCP is well-suited for use with computational design and parametric modeling tools (Banihashemi et al., 2025). Toolpaths can be optimized not just for layer-by-layer deposition, but also for curved-layer printing, adaptive slicing, and hybrid reinforcement methods. This offers possibilities for printing freeform panels, double curved façade elements, custom columns, architectural furnishings, and structurally efficient shells (Vertico, 2025). By using reinforcing techniques such as steel bars, cables, or fibers, this process can overcome the limitations of layered concrete for structural-grade applications.

1.3. Computer-aided process planning for AMoC

Computer-aided process planning (CAPP) for AMoC turns a digital design into a set of machine-executable instructions that take into consideration material, hardware, and on-site constraints. *Figure 1.6* depicts a typical AMoC operation, which comprises a CAD model (left), a planning workstation, a concrete mixing/pumping unit, the gantry/robotic deposition system, and the printed part. In practice, CAPP consists of part modelling and manufacturability checks in CAD, material and hardware selection (mixer/pump, nozzle size, pump pressure), slicing or surface decomposition to produce printable layers, toolpath generation and optimization, and conversion to machine code with embedded process parameters (extrusion rate, print speeds, and pauses).

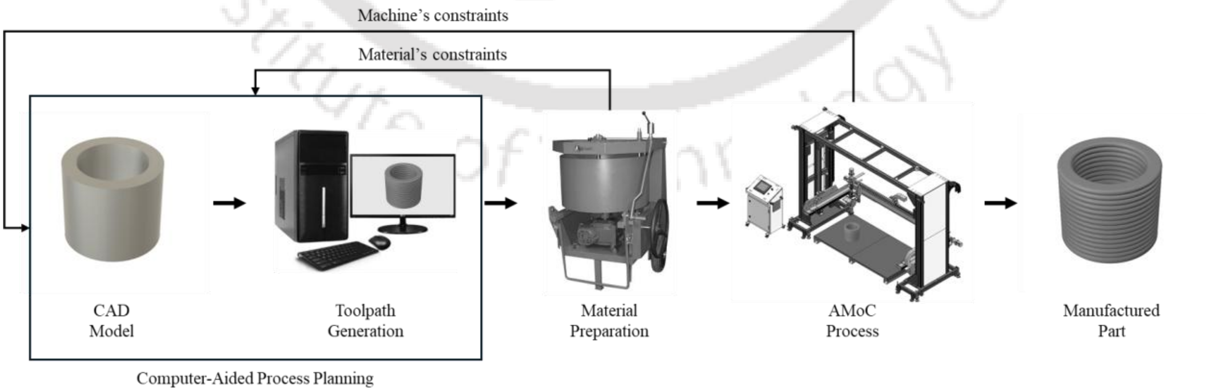

Figure 1.6 Process flow of additive manufacturing of concrete

The most crucial component of CAPP is toolpath planning. A toolpath is the specified path that the printing nozzle takes to deposit concrete and create a three-dimensional object. The efficiency of AMoC is heavily reliant on toolpath, since it influences both dimensional accuracy and mechanical performance of the printed parts.

A number of objectives can be accomplished using efficient toolpath strategies, including reducing printing time, increasing material utilization by eliminating interruptions, improving print quality, and enhancing interlayer bonding for increased structural integrity. Toolpath planning also enables the realization of a wide range of architectural and functional applications, including complex freeform geometries and structural components, as well as furniture, façade panels, and artificial coral reefs for marine habitat restoration (*Figure 1.7*). An efficient toolpath planning allows for a diverse variety of design choices, from artistic textures and lightweight lattice infills to large-scale building parts, broadening the reach of AMoC beyond traditional uses.

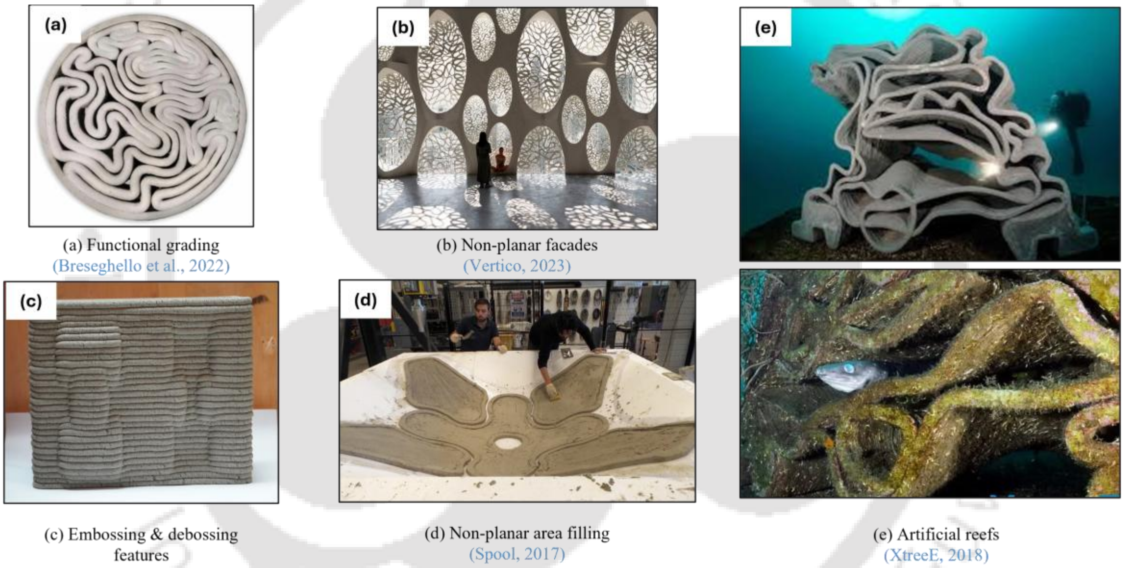

Figure 1.7 Applications of toolpath in AMoC

To provide a comprehensive understanding of its role, the following three sections review the existing literature on various aspects of CAPP. The first part discusses Design for Additive Manufacturing of Concrete (DfAMoC), specifically the slicing approaches currently used in AMoC. The difficulties of using typical fused deposition modelling (FDM)-based slicing tools are highlighted here, as they fail to account for the inherent limitations of concrete extrusion, such as large nozzle sizes, rheological behavior, and time-dependent buildability. The toolpath strategies for area filling are reviewed in the second part, which also covers optimization approaches, continuous path generation techniques, and their effects on material utilization, printing efficiency, and structural isotropy. To overcome the inherent drawbacks of conventional planar slicing, the third section examines the emerging field of non-planar area-filling toolpath techniques, which enable deposition on curved surfaces. These methods create new opportunities for the fabrication of structurally sound and geometrically complicated components.

1.3.1. Literature on design for AMoC

AMoC is transforming the building and construction industry by facilitating formwork-free production of intricate geometries, minimizing material waste, expediting building timelines, and enhancing build quality (Lim *et al.*, 2012; Khoshnevis, 2004; Buswell *et al.*, 2018; Malaeb *et al.*, 2019). AMoC often employs robotic arms or gantry systems to extrude fresh concrete layer-by-layer, adhering to a toolpath generated from the CAD input (Bos *et al.*, 2016). This advancement meets architectural and engineering demands by enabling greater design freedom for freeform structures, enhanced performance, and optimized, customized material usage (ElMaraghy *et al.*, 2012; Cardin *et al.*, 2013; Hannibal & Knight, 2018; Kim *et al.*, 2023). However, its practical implementation is impeded due to the lack of design methodologies considering the process-specific limitations of using concrete as feedstock material (Wu *et al.*, 2016). A study of current literature indicates that, despite significant efforts to build bespoke slicing algorithms for AMoC, a few studies have suggested design methodologies for creating geometries appropriate for AMoC from the outset. The literature pertaining to CAPP for AMoC is summarized in *Table 1.1,* where design for additive manufacturing (DfAM) methodology was not mentioned.

Table 1.1 Summary of Computer-aided process planning methods literature pertaining to AMoC

Authors	Toolpath Strategy / Tool	Key Focus	DfAM methodology mentioned?
Duarte *et al.* (2023).	Ultimaker Cura + HAL plugin (Grasshopper)	Toolpath generation and test sample fabrication	No
Wu *et al.* (2022).	Intersecting curves from non-parallel planes	Non-planar layered printing (software not specified)	No
Diggs-McGee *et al.* (2019).	Linux CNC	Full-scale printing (512 sq. ft.) and delay impact analysis	No
Bi *et al.* (2022).	Grasshopper Python script	G-code generation for area filling	No
Breseghello *et al.* (2023).	Grasshopper	Weaving toolpath to improve beam strength	No
Weng *et al.* (2021).	Dynamo + Revit plug-in	Sinusoidal wall path automation	No
XtreeE (2025)	Custom Grasshopper-based slicer	Industrial-scale printing with proprietary G-code interface	No

It is clear from *Table 1.1* that novel toolpath strategies and G-code generation techniques have been proposed in the past. However, no one offers a systematic DfAMoC methodology including self-supporting geometries, overhang angle constraints, nozzle continuity, and surface-based path design (Shakor *et al.*, 2019; Keating *et al.*, 2017). While representing progress, these approaches remain limited in achieving printable and optimized geometry for AMoC.

Design for Additive Manufacturing (DfAM)

DfAM was initially developed as a more comprehensive Design for Excellence (DfX) framework within the manufacturing industry. In this context, "X" refers to several objectives to improve particular characteristics, and this strategy makes it possible to accomplish specifically targeted improvements through concepts such as Design for Construction Waste Minimization and Design for Deconstruction (Laovisutthichai *et al.*, 2024). DfAM is a methodology that enhances part design to exploit the distinctive advantages of AM. It facilitates the fabrication of intricate geometries, cohesive assemblies, and bespoke components while minimizing production and assembly expenses (Gibson *et al.*, 2021). One of the essential parts of DfAM is design for manufacturing and assembly (DfMA). DfMA has received much interest in the AMoC field due to its potential to streamline construction processes and develop modular (and printable) designs that can minimize operational costs of the construction (Sadakorn *et al.*, 2022).

DfMA ideas are used to build 3D printed load-bearing walls with steel-plate dry joints, resulting in faster assembly with prefabricated systems. Similarly, a design for an assembly procedure through digital models and robotic technology is proposed to fabricate a bridge column that requires precise form optimization (Nguyen *et al.*, 2022). Omrani & Iordanova (2023) observed a clear synergy between modularization and digital design, fabrication, and it effectively addresses both low- and high-frequency changes, thus improving the adaptability and flexibility of buildings. In another study, researchers have highlighted the limitations of traditional 2D/3D technologies in addressing façade constructability and advocated for DfMA-driven digital workflow for enabling scalable and structurally robust 3D printed structures (Montali *et al.*, 2018; Tuvayanond & Prasittisopin, 2023). However, the lack of DfAM integration within commercial CAD software and the reliance on FDM-based toolpath generators hinder the widespread adoption of AMoC for complex, form-optimized structures.

Figure 1.8 depicts a standard AMoC workflow, encompassing the stages from design to fabrication and assessment. The procedure commences with a CAD model of the part, which is processed using FDM-based slicing software to produce the toolpath. A gantry-based 3D printer fabricates the part by depositing fresh concrete following the toolpath, and later, the printed part is examined for any inconsistencies, including distortions or departures from the intended design. This workflow is considered uncontrolled, as using FDM-based slicing software may result in uncontrolled material deposition or an unoptimized AMoC process.

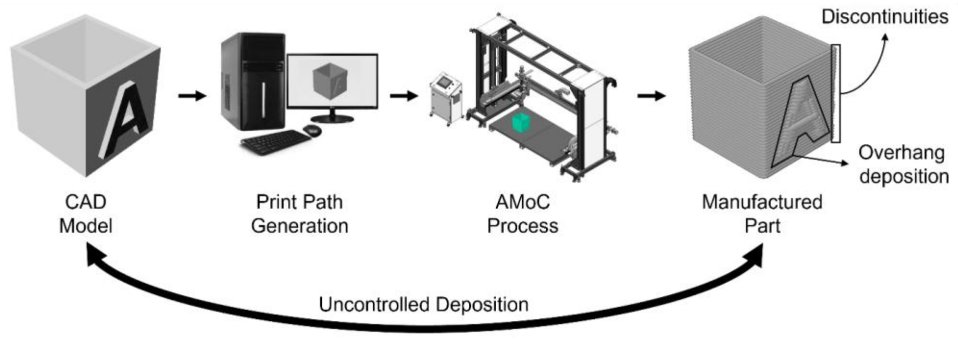

Figure 1.8 Standard process chain for AMoC

Direct implementation of FDM-based toolpath in AMoC causes more challenges due to the unavailability of material-specific properties, as detailed in the *Appendix section A1.1* for various geometries. Incorporating DfAM into Part design and toolpath generators could optimize part design by considering self-supporting design and early-age material properties.

1.3.2. Literature on area-filling strategies for AMoC

Toolpath strategies in AMoC are commonly classified according to geometry: lattice, solid, contour/cell, and topologically optimized structures. This study focuses on solid constructions with 100% infill and controlled infill density. Conventional FDM-inspired techniques, such as paintbrush, zigzag, and contour-parallel toolpaths, are simple but have drawbacks, such as frequent interruptions, underfilling, discontinuities, and inefficient toolpaths (Dunlavey, 1983; Rajan et al., 2001; Park & Choi, 2000; Dolen & Yaman, 2014). Spiral routes improve continuity by connecting contours from the center outward (Ren et al., 2009; Wang et al., 2005); however, there are still restrictions in maintaining uniform infill and reducing discontinuities. These conventional toolpath strategies are shown in *Figure A2.1* (Appendix Section A2). To overcome these issues, hybrid solutions that combine spiral, contour-parallel, and zigzag methods have emerged. Space-filling curves like the Hilbert curve (Kapil et al., 2016) provide a continuous trajectory for efficient infill, but the issue of underfilling is still there. On the other hand, traditional methods still require frequent nozzle lifts and retractions, which are inefficient in AMoC systems that use concrete pumps and cannot be stopped during extrusion. This emphasizes the need for continuous toolpath solutions that minimize print head retractions while enhancing process efficiency. A continuous toolpath based on the Travelling Salesman

Problem (TSP) is employed for complete and customized area-filling with tailored density in AM (Singh et al., 2022; Singh et al., 2024); still, the processing time for larger areas is much higher. In recent years, numerous continuous toolpath solutions have been developed to improve the efficiency and quality of AMoC. These developments seek to reduce nozzle retractions and sharp turns, increase material continuity, and facilitate printing complex shapes. These methods include transfinite mapping, hybrid filling schemes, space-filling curves, and optimization algorithms. Despite their contributions, most techniques have limitations in geometric adaptability, extrusion control, and computing needs. *Table 1.2* provides a quick overview of significant contributions.

Table 1.2 Overview of significant area-filling strategies in AMoC

Reference	Proposed Strategy	Key Limitations
Jin et al. (2017)	A *go-and-back strategy* that generates short, closed sub-paths to eliminate retractions and reduce idle travel. Sub-paths start and end at nearby points to ensure continuity.	▪ Lacks a defined rule for contour-contour joining ▪ Inconsistent linking ▪ Sub-path transitions are unoptimized ▪ Sharp corners remain in complex features ▪ Underfill and overlapping still occur due to offset issues
Wan et al. (2020)	A *transfinite mapping method* that partitions complex shapes into rectangular sub-regions and generates continuous toolpaths based on concrete rheology.	▪ Manual selection of decomposition points ▪ Merging of adjacent regions is complex and error-prone ▪ Extrusion rate adjustments are not integrated, leading to potential material inconsistency ▪ Underfilling is high in the generated toolpaths.
Zhao et al. (2016)	A *Connected Fermat Spirals (CFS)* that fills decomposed sub-regions with smooth, low-curvature spiral paths, later connected to form a globally continuous trajectory.	▪ Not capable of filling sharp corners ▪ Lacks a global strategy to minimize sharp turns ▪ Spiral curves are not stretchable to fit varying regions ▪ Low compatibility with printers ▪ Uniform material deposition increases underfilling & overlapping.
Wan et al. (2022)	A *template-based transfinite mapping (TPTM)* method that maps predefined patterns (zigzag, spiral) onto the geometry with real-time filament width control for gap-free deposition.	▪ Depends on manual region decomposition ▪ Merging of mapped regions can introduce discontinuities ▪ Lacks defined control of extrusion rate under geometric complexity ▪ Underfilling & overlapping defects remain in the toolpath
Bi et al. (2022)	A *hybrid toolpath framework* combining double-offset outward contours and zigzag filling to generate globally continuous paths for large-format and partial infill printing.	▪ Post-processing is time-intensive ▪ Curvilinear toolpaths reduce effective print speed ▪ Residual sharp turns impact motion smoothness in partial infill ▪ Overfilling frequently occurs at corners ▪ Narrow features cannot be filled due to limitations of the double-offset strategy.

Reference	Proposed Strategy	Key Limitations
Sahu & Panda (2025)	To improve deposition quality, a *TSP-based toolpath strategy for AMoC* minimizes discontinuities using optimized grid fitting, boundary trimming, and sharp-turn elimination.	▪ Computationally expensive, especially for large-scale geometries ▪ Post-processing is needed to refine toolpath transitions and fill residual voids ▪ Loss of intricate details in fine or thin features ▪ Visible underfilled areas

1.3.3. Literature on non-planar area-filling strategies

AMoC is revolutionizing construction by enabling the automated creation of freeform structures without the need for traditional formwork. Nonetheless, traditional 3DCP technologies rely heavily on flat, layer-by-layer deposition, which limits geometric complexity and frequently produces the staircase effect on curved surfaces (Lim et al., 2020). This constraint is particularly significant in architectural and structural applications that require surface quality, isotropy, and continuity of material deposition.

Modern studies have sought to address these issues using temporary and adjustable support systems. Costanzi et al. (2018) suggested printing on temporary freeform surfaces utilizing a flexible mold created at TU Delft with a 4-DOF gantry printer from TU Eindhoven. Their study revealed hybrid processes that used 3D printing and casting to create partially printed, partially cast shell structures, emphasizing the versatility of adjustable molds for curved geometries. This notion is consistent with previous studies on Curved Layered Fused Deposition Modelling (Lim et al., 2012), which found that curved slicing procedures enhanced surface quality and mechanical performance compared to flat layers.

Lim et al. (2020) extended the notion of adaptable supports by introducing the Adaptable Membrane Formwork. This pin-supported membrane system enabled the direct 3D printing of doubly curved, non-developable concrete surfaces, such as domes and saddles. Their quantitative study validated excellent geometric accuracy, making it the first practical example of freeform, unsupported concrete surfaces. This builds on previous advances in CC (Khoshnevis, 2004) and flexible formwork systems, such as those developed by Renzo Piano in the 1960s and the ADAPA membrane formwork (Schipper et al., 2017), which were initially designed for casting applications but were later adapted for AM.

In addition to these physical assistance options, new research emphasizes the significance of robust path planning algorithms. Wan et al. (2022) investigated the limitations of traditional zigzag and contour-parallel toolpaths, which often result in discontinuities, abrupt twists, and unfilled zones in geometrically complex locations. They devised a transfinite mapping-based route planning approach that utilizes continuous template pathways to handle complex freeform geometries, leading to zero-gap deposition and reduced defects. Their findings are consistent with other path optimization research that expands offset-based contour approaches (Voronoi-based (Liu et al., 2017); and spiral-based strategies (Xu et al., 2015; Wu et al., 2016)).

1.3.4. Literature summary and motivation

Recent years have seen a significant increase in interest in the development of CAPP for AMoC. Literature currently in publication emphasizes discrete advancements in various fields, but it lacks a comprehensive framework that considers the unique difficulties of the concrete extrusion process.

Research on design for AM focuses on leveraging the unique qualities of AM, such as creating optimized components, modular assemblies, and self-supporting geometries. However, studies reveal that the majority of toolpath solutions in AMoC are obtained from slicers based on FDM, which do not adequately account for the rheological and early-age material properties of concrete. Despite the fact that DfMA principles and modular techniques have been evaluated for walls, joints, and façade systems, no thorough DfAMoC methodology has been developed that takes self-supporting restrictions, overhang angles, or nozzle continuity into account. Complex structural applications become inefficient when this kind of connection is lacking, as it leads to uncontrolled workflows where geometry and toolpath design are divorced from material behavior.

According to the literature on toolpath planning for area filling in AMoC, using traditional FDM-derived techniques, such as spiral, zigzag, and contour infill, has serious drawbacks. Underfilling, overlapping, and sharp bends are common problems with space-filling curves and hybrid solutions, despite their enhanced continuity and decreased retractions. Since stopping a pump in the middle of the process and excessive retractions result in faults, these disadvantages are crucial for concrete extrusion. Although they show improvement, advanced techniques such as transfinite mapping, Fermat spirals, and template-based mapping still have issues with scalability and extrusion control. The TSP has served as the inspiration for recent studies that have added continuous pathways to maximize area-filling for continuity and isotropy. Large-scale geometries still face challenges in terms of post-processing requirements and computational costs. The staircase effect is frequently seen on curved surfaces due to the flat, layer-by-layer deposition used in conventional AMoC. To overcome these mechanical and geometric restrictions, non-planar techniques have been explored, including hybrid casting-3D printing systems, membranes, and flexible supports. For instance, flexible molds and versatile membrane formworks have enabled the successful deposition of freeform surfaces, such as saddles and domes. Smoother deposition and defect reduction have been demonstrated by parallel developments in non-planar toolpath algorithms, such as spiral-based techniques and transfinite mapping.

Based on the above research gaps, it is evident that AMoC lacks an integrated CAPP framework that systematically connects design intent, area-filling optimization, non-planar deposition, and process constraints. Consequently, this study narrows its focus to a specific set of process parameters that directly address these gaps. Rather than considering all possible AMoC variables, the parameters highlighted in light blue in *Figure 1.9* are identified as the primary areas of interest for this research.

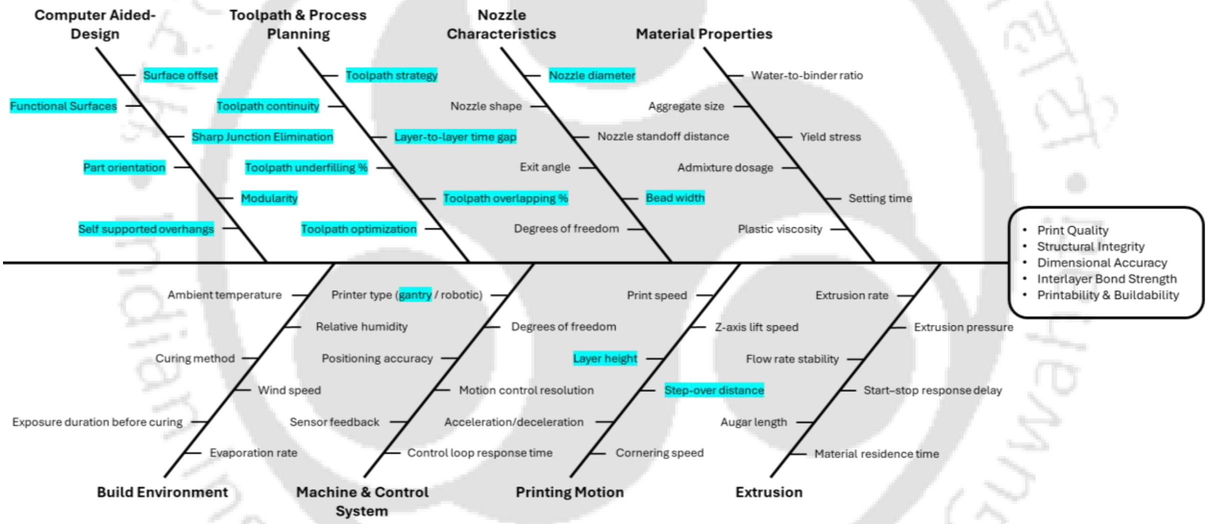

Figure 1.9 Fishbone diagram for process parameters that affects AMoC

These parameters predominantly relate to toolpath strategy and continuity, sharp junction elimination, control of underfilling and overlapping, layer-to-layer time gap, surface offset, geometric considerations such as part orientation and self-supported overhangs, deposition parameters including nozzle diameter, bead width, layer height, and step-over distance, as well as system-level aspects such as gantry configuration. The deliberate selection of these parameters enables a focused investigation into improving toolpath efficiency, extrusion stability, and geometric fidelity in AMoC, while other influencing factors are considered beyond the scope of the present study.

1.4. Research gaps and objectives

1.4.1. Research gaps

The following research gaps are identified:

- Absence of a systematic DfAMoC framework for contour-based toolpath planning.
- Existing area-filling toolpath strategies for AMoC are limited by manual interventions, poor adaptability to complex geometries, and persistent quality issues.
- The high computational cost of optimization-inspired strategies, such as TSP, limits scalability.
- Lack of non-planar area-filling strategies for complex and freeform surfaces in AMoC.

To visually contextualize the identified research gaps and clearly position the contribution of the present study, an Ashby-style schematic representation is introduced. Such a chart enables a comparative mapping of existing AMoC toolpath planning approaches against key performance attributes, including planning complexity, adaptability to geometry, computational demand, and capability for non-planar deposition. As illustrated in *Figure 1.10*, the absence of a structured DfAMoC framework for contour-based toolpath planning is highlighted by the fragmented and application-specific nature of existing methods.

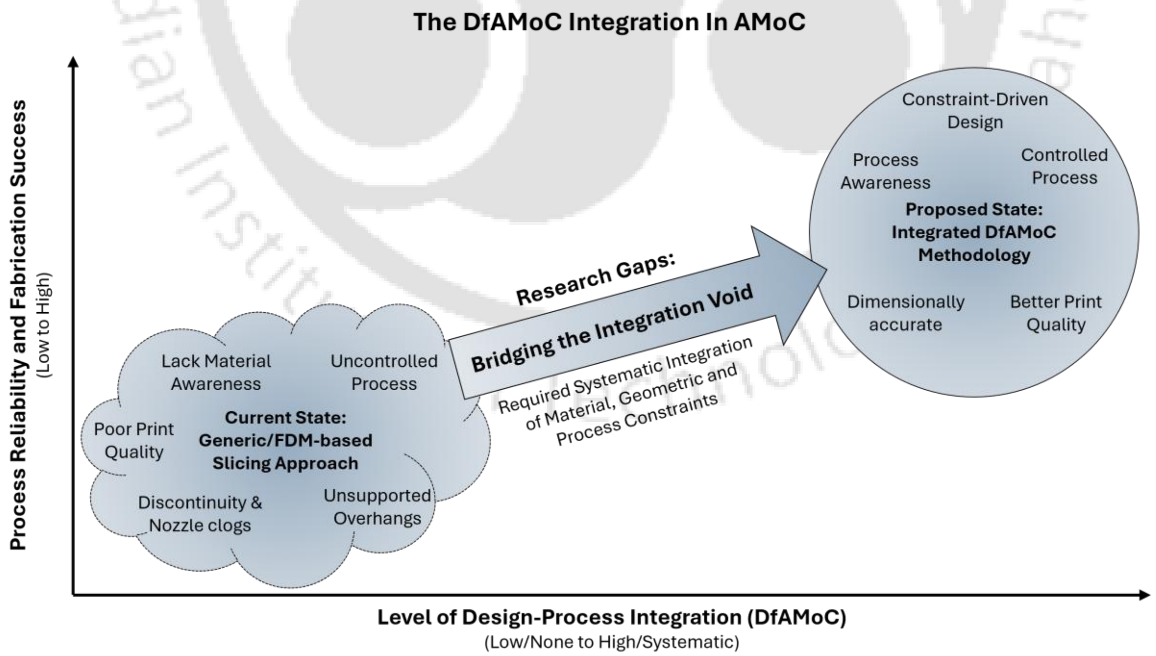

Figure 1.10 DfAMoC integration gap in AMoC

Figure 1.11(a) emphasizes the limitations of conventional FDM-based area-filling strategies, which have poor continuity, print time and print quality and exhibit reduced robustness when applied to different geometries. Furthermore, *Figure 1.11(b)* demonstrates how optimization-inspired approaches, such as TSP-based strategies, occupy a region of high computational cost with limited scalability and applications, while non-planar area-filling solutions for freeform surfaces remain largely unexplored. The proposed study strategically positions itself within this unaddressed region of the schematic, bridging the gap between geometric adaptability, computational feasibility, multiple applications and process robustness. By doing so, the presented framework advances toward a scalable, systematic, and non-planar-capable toolpath planning solution for AMoC, thereby directly addressing the identified research gaps.

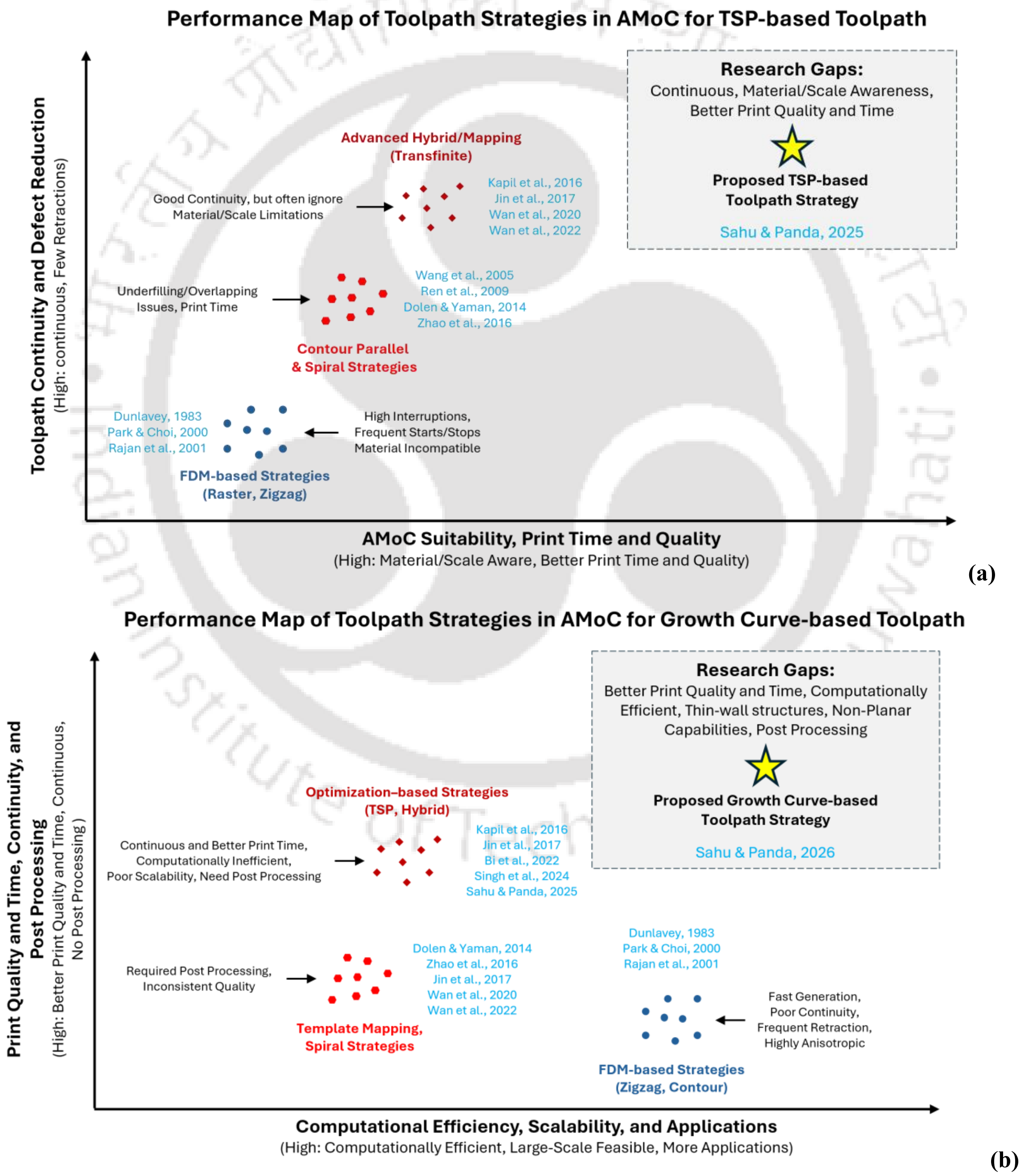

Figure 1.11 Performance map of toolpath strategies in AMoC for: (a) TSP-based toolpath, and (b) Growth curve-based toolpath

1.4.2. Research objectives

Building on these gaps, the following objectives have been identified:

1. **To develop a DfAMoC framework for contour printing**, where additive manufacturing design principles are adapted specifically for the AMoC process.
2. **To investigate a TSP-based toolpath strategy for area filling** to improve isotropy, reduce non-productive travel, and ensure path continuity for solid structures.
3. **To develop a growth curve-based continuous toolpath strategy for area filling**, offering a computationally efficient and scalable solution that overcomes the limitations of TSP-based methods.
4. **To investigate the feasibility of the growth curve-based approach for non-planar area filling**, enabling the generation of continuous deposition paths on arbitrary non-planar meshes.

1.5. Organization

This thesis is organized into six chapters, each addressing specific aspects of CAPP for AMoC, followed by appendices, references, and a list of publications derived from this research.

Chapter 1: Introduction and Literature Review

This chapter introduces the motivation, scope, and objectives of research. It also provides a comprehensive literature review on conventional and digital construction methods, with a focus on AMoC. Key aspects of design for AMoC, including area-filling strategies and continuous toolpath generation for planar and non-planar applications, are critically examined to highlight existing gaps and define the research directions pursued in this work.

Chapter 2: Design for Additive Manufacturing of Concrete (DfAMoC) Framework

This chapter develops a DfAMoC framework tailored for contour printing, where AM design principles are adapted to address the unique challenges of concrete extrusion. The framework emphasizes the integration of geometry constraints, nozzle characteristics, and process parameters to enable effective and optimized contour-based printing.

Chapter 3: Investigation into a TSP-based toolpath strategy for area filling

This chapter investigates the implementation of a TSP-based toolpath strategy for solid structure area filling. The approach is designed to enhance isotropy, minimize non-productive travel, and ensure continuous deposition paths. Comparative analysis with conventional infill strategies demonstrates the benefits and limitations of the TSP approach in the context of AMoC.

Chapter 4: Development of a growth curve-based toolpath strategy for area filling

This chapter proposes a growth curve-based continuous toolpath generation method for area filling. The strategy provides a computationally efficient and scalable solution while overcoming the limitations of the TSP-based method, such as exponential computation time and complexity in large-scale applications. The framework is validated across a range of geometries, highlighting robustness and adaptability.

Chapter 5: Investigation into a Non-Planar Growth Curve-Based Toolpath Strategy

This chapter extends the growth curve-based method to non-planar area filling. It investigates the feasibility of generating continuous deposition paths on arbitrary non-planar meshes, thereby enabling the fabrication of complex surfaces beyond conventional layer-by-layer deposition. The proposed strategy lays the groundwork for non-planar AMoC applications using robotic systems.

Chapter 6: Conclusion and Scope of Future Work

This chapter summarizes the research findings, contributions, and limitations of the developed frameworks and strategies. It also outlines future research directions, including the integration of reinforcement, consideration of interlayer bond strength, and potential applications in architectural and infrastructure-scale projects.

The thesis concludes with the Appendix, which provides supplementary material, followed by the References section containing all cited works. Finally, a Publication List highlights the research outcomes published in journals and conferences during the course of this study.

Chapter 2: Design for Additive Manufacturing of Concrete (DfAMoC) Framework

This chapter develops a DfAMoC framework tailored for contour printing, where AM design principles are adapted to address the unique challenges of concrete extrusion. The framework emphasizes the integration of geometry constraints, nozzle characteristics, and process parameters to enable effective and optimized contour-based printing.

A portion of this chapter has been published:

Sahu, A., & Panda, B. (2025). An additive manufacturing-oriented design approach for digital construction. *Rapid Prototyping Journal*. *https://doi.org/10.1108/RPJ-04-2025-0159*

2.1. Abstract

AMoC offers significant potential for fabricating complex concrete components; however, current designs are often developed without adequately accounting for manufacturing constraints, such as minimum overhang angles, or the material behavior of fresh concrete. This chapter proposes an integrated workflow that combines a surface-based slicing strategy with DfAMoC guidelines to address these limitations. Surface models are generated in accordance with DfAMoC principles and applied to three representative geometry classes: planar surfaces, non-planar surfaces, and geometries incorporating embossed or debossed features. The optimized surface models are subsequently processed to generate custom G-code suitable for extrusion-based concrete 3D printing. The proposed workflow is experimentally validated using a gantry-type AMoC system across both planar and non-planar designs. Results demonstrate that the proposed DfAMoC-driven, surface-based approach enables continuous toolpaths, uniform material deposition, and stable fabrication of self-supporting features, leading to improved print quality compared with conventional fused deposition modeling–based slicing methods. The printed components exhibit consistent interlayer bonding and enhanced dimensional accuracy, confirming the robustness and reliability of the method. Overall, this chapter presents a streamlined and practical end-to-end workflow—from surface modeling to slicing and G-code generation—that effectively exploits the capabilities of AMoC while minimizing common print defects.

2.2. Design for Additive Manufacturing of Concrete (DfAMoC)

2.2.1. AMoC process and materials

This study utilizes a lab-scale 3D concrete printer available at the Indian Institute of Technology Guwahati, India (*Figure 2.1*) for testing DfAMoC guidelines. The gantry-based AM system, with a build volume of 1000 mm × 1000 mm × 1000 mm, is designed for laboratory-scale complex concrete structure. It operates with three degrees of freedom, allowing precise movement of the extruder along the X, Y, and Z axes to continuously deposit the material. The printer supports both screw extrusion and pump-based concrete deposition without any provision for support material. The AMoC process planning consists of three essential stages: (1) DfAMoC, (2) Slicing of the designed surface model, and (3) G-code generation.

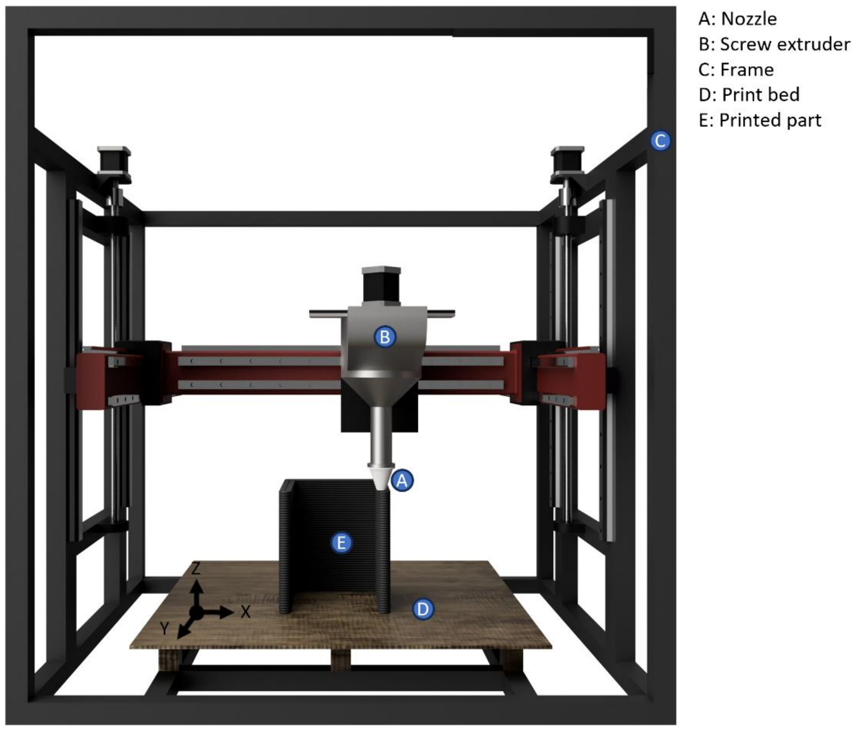

Figure 2.1 Schematic of the extrusion-based 3D concrete printer

Figure 2.2 shows the proposed AMoC process planning, wherein the print head trajectory was first meticulously crafted in the surface form, conforming to new design guidelines specified in Section 2.3. The second phase focuses on generating the necessary instructions for the AMoC process. It begins with user input, where a DfAMoC - enabled surface CAD model in STereoLithography (STL) format is provided, along with parameters such as layer height, nozzle diameter, and slicing data. Essential printing parameters, including layer count, print speed, and mixture density, are also specified, followed by uniform slicing of the surface model using an open-source slicing technique (Bhandari, 2025). A custom MATLAB-written script generates the G-code file and simulates the printing process to verify the toolpath trajectory.

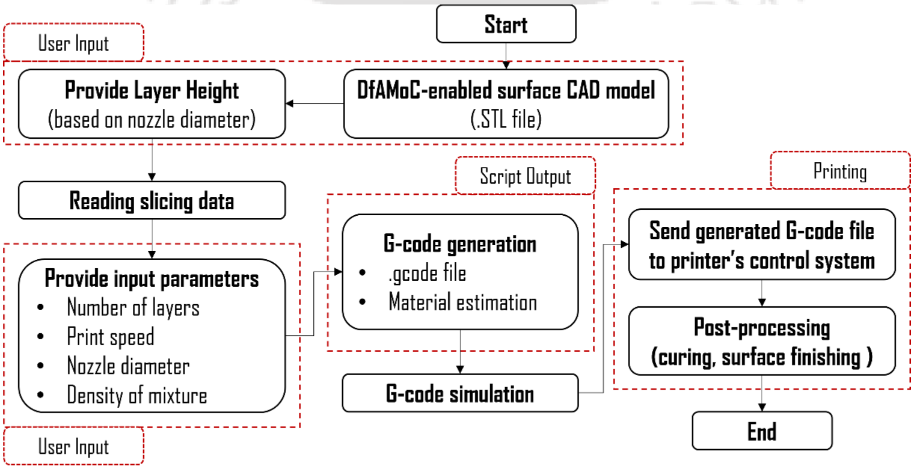

Figure 2.2 Flowchart of stages 2 and 3 of the AMoC process

2.2.2. Materials and printable mixture properties

A cement-based (Binder: 90 wt.% Portland cement and 10 wt.% Micro silica) ***3D mortar material mix*** amenable to 3D printing was selected which has printability and the design details for this 3D mortar material mix are given in *Table 2.1*. The presence of a viscosity-modifying agent (VMA) improved workability, reducing bleeding and segregation during the extrusion. Concurrently, the Superplasticizer (SP) enhanced the fluidity of the mix while maintaining the printed layers' structural integrity. The 3D printable mix demonstrated a compressive strength of ~ 30 MPa and flexural strength between 3.5 - 4 MPa after 28 days, and later, early-age strength of the printed mix was characterized for estimating the part buildability.

Table 2.1 3D mortar material mix design used in this study

Fine sand /Binder	Water /Binder	Cement /Binder	Micro silica /Binder	Superplasticizer /Binder	VMA /Binder
1.5	0.375	0.9	0.10	0.001	0.002

2.3. DfAMoC guidelines

Developing an optimized surface model of the printed part is an important task in CAPP for AMoC, as it enables uninterrupted material deposition, preventing disturbances resulting in printing defects such as voids, weak interlayer adhesion, or excessive material buildup. This optimization markedly decreases frequent print head movements, minimizes material waste, and improves toolpath continuity, thus enhancing the final part quality and mechanical performance. Moreover, a meticulously crafted print trajectory ensures stability in the deposition process, averting inconsistencies in layer formation, ensuring uniform adhesion between successive layers, and facilitating the fabrication of components with self-supporting overhang geometries, such as embossing, debossing, and other three-dimensional features. This section delineates the essential design principles required to develop an optimized surface model, considering the geometric and material constraints of the gantry-based AMoC process.

2.3.1. Design guidelines for AMoC

I. **Surface Offset:** In AMoC, surface offset $'S_o'$ for outer surface of the part must be $'w/2'$, where w is the bead width. Accurate offsetting is essential for maintaining proper fit between the components, particularly in applications requiring precise connections, such as interlocking features. Any deviation can lead to misalignment, loose connections, or compromised stability of the printed structures.

Surface Offset; $\boldsymbol{S_o} = {}^{w}/_{2}$

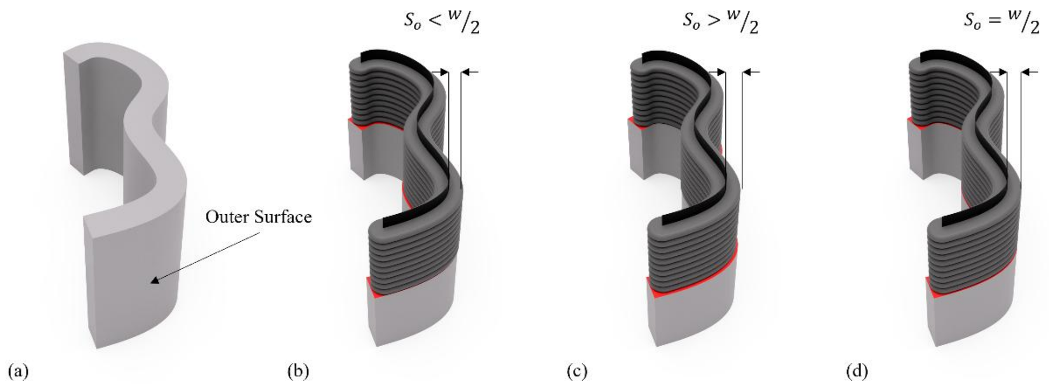

Figure 2.3 (a) Part to be printed, (b) Not ideal case 1: $S_o < {}^{w}/_{2}$, (c) Not ideal case 2: $S_o > {}^{w}/_{2}$, and (d) Ideal case: $S_o = {}^{w}/_{2}$

Figure 2.3 depicts the effect of surface offsetting on the dimensional accuracy of AMoC-printed structures while maintaining a constant bead width $'w'$. *Figure 2.3(a)* illustrates the outside surface of the actual part. In contrast, *Figure 2.3(b)* depicts the condition of surface offset, $S_o < {}^{w}/_{2}$ resulting in underfilling on the inner surface and overfilling on the outer surface. *Figure 2.3(c)* depicts the results of surface offset, $S_o > {}^{w}/_{2}$ leading to overfilling on the inner surface and underfilling on the outer surface. *Figure 2.3(d)* depicts the ideal scenario where $S_o = {}^{w}/_{2}$, ensuring uniform material deposition, dimensional accuracy, and a perfect fit for assembly. These graphics highlight the significance of precise surface offsetting in AMoC for attaining structurally robust, high-quality printed components.

II. **Functional surface design:** A functional surface in AMoC refers to a non-planar surface designed to enhance the aesthetics and structural integrity of the 3D printed part. It facilitates architectural elements such as complex facades and embossed or debossed details without supplementary formwork and support systems. These functional surfaces are self-supporting geometries that enhance layer adhesion while offering stability during the printing process. These functional surface designs must account for gravitational forces and load distribution to ensure stable layer stacking and avoid printing failure. The overhang print height of the functional surfaces must be determined within acceptable ranges for an angle chosen to prevent early-age structural collapse. In this regard, experiments with layer heights of 10 mm were performed to ascertain the material buildability using a 25 mm bead width. The results illustrated in *Figure 2.4(a)* indicate the operational range within which components can be printed successfully without failure. A safety factor of 30% was used by lowering the allowable print height for each overhang angle, hence maintaining structural integrity during the part manufacturing. The investigation includes printing multiple designs to evaluate buildability at several overhang angles. A vertical cylinder was successfully printed at 0 degrees, exhibiting stability under self-supporting conditions. But when the overhang angle is increased, the printed shape evolves into an inverted frustum of a cone, with each layer expanding outward. A similar experimental study was performed for the layer height of 8 mm with a bead width of 20 mm. It is clear from the results (*Figure 2.4(b)*) *that* reliable prints can be obtained at angles up to 32.5 degrees, using 10 mm layer height, whereas for 8 mm layer height, the threshold was 35 degrees. Due to gravity forces and material constraints, the structure typically fails when the layer deposition surpasses one-third of the bead width (w). This failure defined the limiting point beyond which overhang angles become impractical.

The lab-scale 3D printer utilized in the research has a maximum print height limitation of 1000 mm. Consequently, print heights beyond 1000 mm could not be comprehensively evaluated for angles approaching vertical.

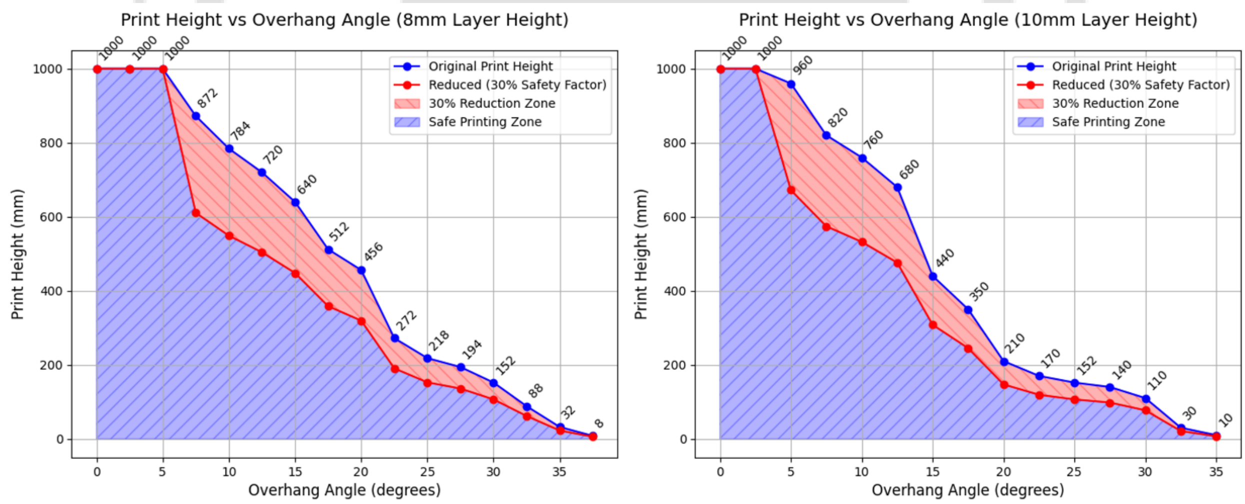

(a) (b)

Figure 2.4 Maximum printable height for different overhang angles using (a) 10 mm layer height with 25 mm bead width and (b) 8 mm layer height with 20 mm bead width

In addition, any unsupported cantilevers must be removed from the design, as they risk the constructability of the structure. Gradual slopes (chamfers) or stepped transitions improve structural integrity and accommodate intricate designs. Moreover, deposition beads must not overlap within a singular layer, as intersecting toolpaths induce stress in the XY plane, potentially compromising structural integrity and resulting in failure at higher heights. Complying with these rules facilitates the creation of non-planar exterior surfaces and functional attributes, such as embossed or debossed embellishments, while maintaining printability within the set limit.

III. **Sharp Junction elimination:** Eliminating sharp junctions present in a non-parallel direction to the slicing plane ensures a smooth and uniform AMoC process. At these sharp junctions, the print head changes direction abruptly, resulting in frequent stops and restarts, material irregularities, and nozzle blockage issues. Implementing a fillet radius of 2 mm at sharp junctions of the surface model is crucial for solving these issues. If the fillet radius is below 2 mm, the smaller number of points defining the curve is insignificant for the intended smoothing effect. Conversely, for a fillet radius of more than 2 mm, voids and deviations from the required dimension were noticed in the final print part, which is not desired in the AMoC process (Sahu & Panda, 2025).

2.3.2. Manufacturing guidelines for AMoC

I. **Part orientation and modularity:** The part orientation for a modular element or an independent single structure must be meticulously set to minimize the need for support structures, as AMoC process does not provide additional support during printing. The optimal orientation allows adequate support to each layer of the part from previous layers to uphold stability during the printing process. Furthermore, the orientation must be chosen to minimize nozzle lifts (toolpath discontinuities), improving printing continuity and reducing overall print time. Reduced nozzle lifts diminish defects and enhance structural integrity by ensuring uniform material deposition. Modular designs are strongly advised when design dimensions exceed the print volume or when there are limits related to transportation and assembly. Dividing items into smaller, interlocking components streamlines the printing process and improves overall constructability, facilitating assembly and transportation. In AMoC, the design process starts with this fixed orientation in mind. However, there are times when more than one possible orientation exists, as shown in *Figure 2.5*. *Figure 2.5(a)* illustrates the part's geometry intended for AMoC fabrication. *Figure 2.5(b)* and *Figure* 2.5*(c)* depict two alternative build orientations, with the z-direction representing the build direction. The orientation in *Figure 2.5(b)* leads to discontinuous toolpaths within layers, significantly increasing the print duration with possible defects in the nozzle lift-off points. The orientation shown in *Figure 2.5(c)* is considered an optimal part orientation as it effectively reduces the print time and defects without sacrificing print stability and part quality.

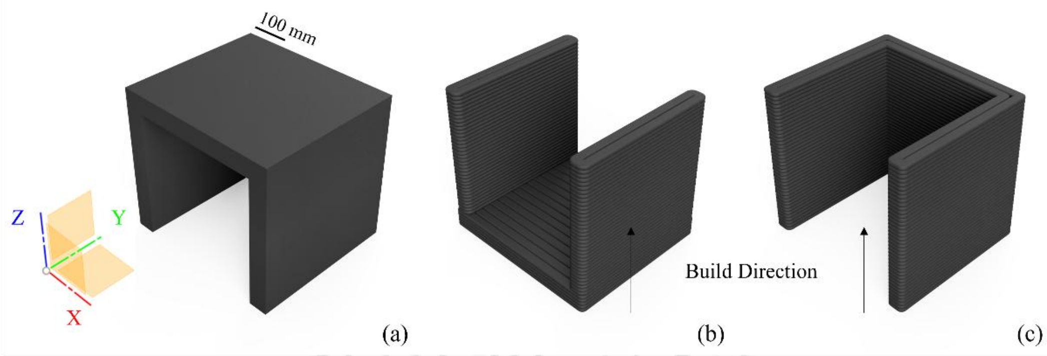

Figure 2.5 (a) 3D model of the Part (to be printed) (b) Build orientation 1 and (c) Build orientation 2

Meanwhile, *Figure 2.6* depicts the modularity concept implemented to address printability and build volume constraints in AMoC. *Figure 2.6(a)* illustrates a podium structure with a total vertical height of 1175 mm. This design includes an internal rack component that exceeds the printer's build volume in its original vertical position and contains overhangs that make it unprintable. Therefore, the podium is segmented into two parts *(Figure 2.6(b))*, where the lower module preserves its initial orientation and is printable within the specified build volume, as illustrated in *Figure 2.6(d)*. Moreover, the upper module is reoriented by a rotation of -87.5° about the Y-axis *(Figure 2.6(c))*, facilitating the part printability without needing support structures. This modular strategy ensures optimal utilization of build volume while preserving the design integrity. After printing the modules, high-strength epoxy resin or mortar grout can join the modules as mentioned elsewhere (Raphael et al., 2023).

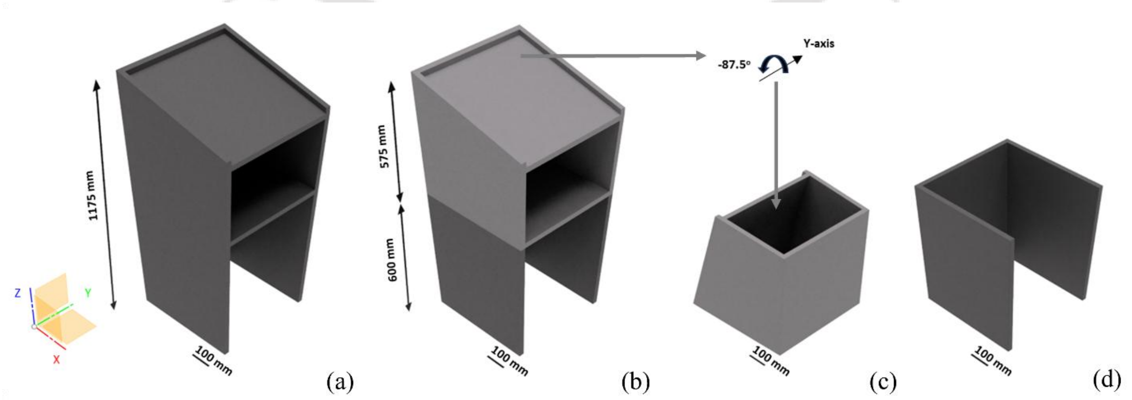

Figure 2.6 3D Models:(a) Podium, (b) Podium split into two modules (build volume & orientation constraints), (c) Top module of the podium rotated by -87.5 degrees along Y-axis for printable orientation, (d) Bottom module in original orientation

II. **Continuous toolpath:** The toolpath continuity in AMoC enhances interlayer adhesion and improves print quality of the part, while mitigating structural weaknesses. When complete continuity is not possible, a single, strategically positioned discontinuity should be introduced, thus making the toolpath as continuous as possible (ACAP). This allows the next layer to be deposited from the same endpoint but in the opposite direction, thereby minimizing disruptions to material flow, decreasing printing time, and avoiding problems such as nozzle blockage or material inconsistencies. In the absence of feasible discontinuity, minimizing the total number of discontinuities present is essential to ensure an ACAP toolpath, thereby reducing the number of nozzle lifts while maintaining optimal print quality and efficiency. *Figure 2.7(a)* illustrates the desired geometry of a lattice wall, whereas *Figure 2.7(b)* demonstrates a discontinuous toolpath that could result in many printing defects. Conversely, *Figure 2.7(c)* illustrates an optimized toolpath characterized by a single discontinuity. Similar to *Figure 2.7(a)*, *Figure 2.7(b)*, and *Figure 2.7(c)*; another example of toolpath selection is shown in *Figure 2.7(d)*, *Figure 2.7(e)*, and *Figure 2.7(f)*.

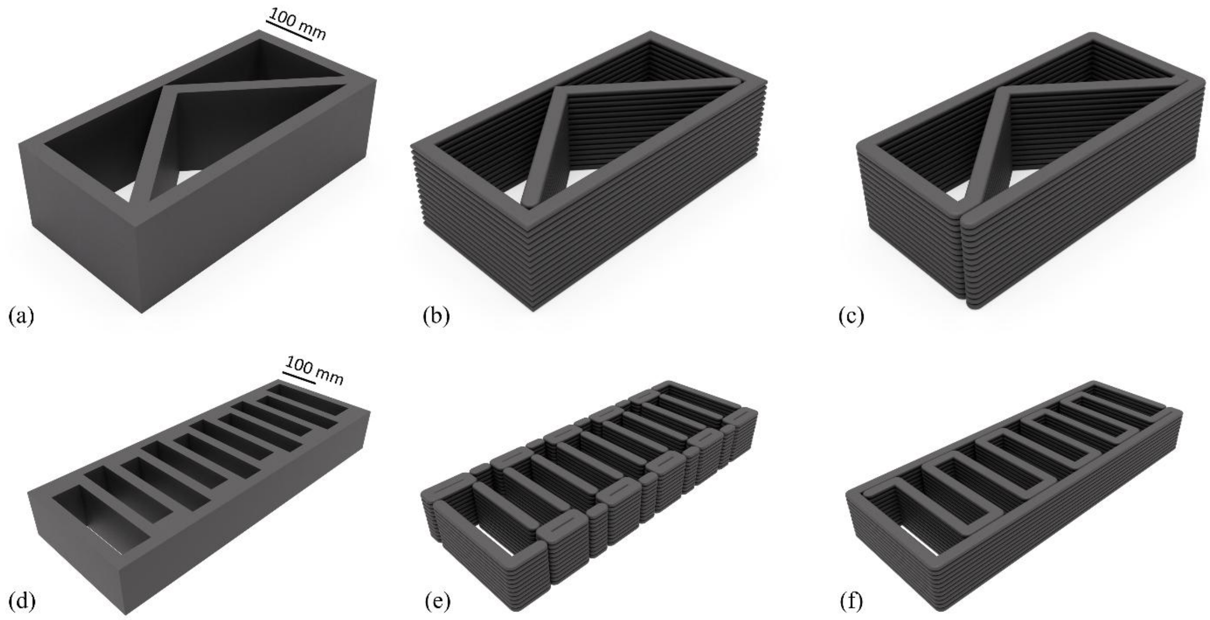

Figure 2.7 3D Models: (a) lattice wall-1, (b) Discontinuous toolpath for lattice wall-1, (c) ACAP toolpath for lattice wall-1, (d) lattice wall-2, (e) Discontinuous toolpath for lattice wall-2, and (f) ACAP toolpath for lattice wall-2

Table 2.2 compares the number of nozzle lifts, toolpath length, and print time (at a printing speed of 60 mm/s) for the above toolpath strategies typically used for making lattice walls. The data indicates that although the discontinuous toolpath is shorter than the ACAP toolpath, its total print time is higher due to more nozzle lifts and additional time delays for the layer changes.

Table 2.2 Parameter comparison for different toolpath strategies.

	Lattice wall - 1		Lattice wall – 2	
Toolpath	Discontinuous toolpath (*Figure 2.7(b)*)	ACAP toolpath (*Figure 2.7(c)*)	Discontinuous toolpath (*Figure 2.7(e)*)	ACAP toolpath (*Figure 2.7(f)*)
Number of nozzle lifts	2	**1**	29	**1**
Toolpath length (mm)	1954.22	1957.404	4343.932	4830.257
Print time (sec) at print speed 60 mm/sec	44.03	**32.57**	142.39	**80.50**

Table 2.3 summarizes the three key design guidelines and two manufacturing-based guidelines proposed in this study for extrusion-based AMoC. The proposed design and manufacturing guidelines-driven process planning is schematically presented in *Figure 2.8*. This workflow provides an efficient and flexible method for AMoC, incorporating non-planar and embossed characteristics while preserving structural integrity, geometric precision, and print quality.

Table 2.3 Design and manufacturing guidelines for an extrusion-based AMoC process

Guidelines		**Description**	**Output description**
Design			
I.	Surface offset	Outer surface must be offset by 'w/2' (w = bead width)	Ensure uniform material deposition, dimensional accuracy, and a perfect fit for assembly.
II.	Functional surface design	The maximum overhang of the functional surface should be within the printable height of the overhang.	Self-supporting structures, stable layer deposition, and avert failure during printing
III.	Sharp junction elimination	Implementing a fillet of 2 mm at the sharp junctions of the surface model	Eliminate jerks in the system, prevent nozzle blockage, and improve print quality
Manufacturing			
I.	Part orientation and modularity	Eliminate max build volume and printability constraints	Ensures printability within the build volume. Overhang sections are printed by using the modularity concept.
II.	Continuous toolpath	Design the ACAP toolpath	Ensure defect-free prints, decrease print time, eliminate nozzle blockage, and eliminate inconsistency in material deposition.

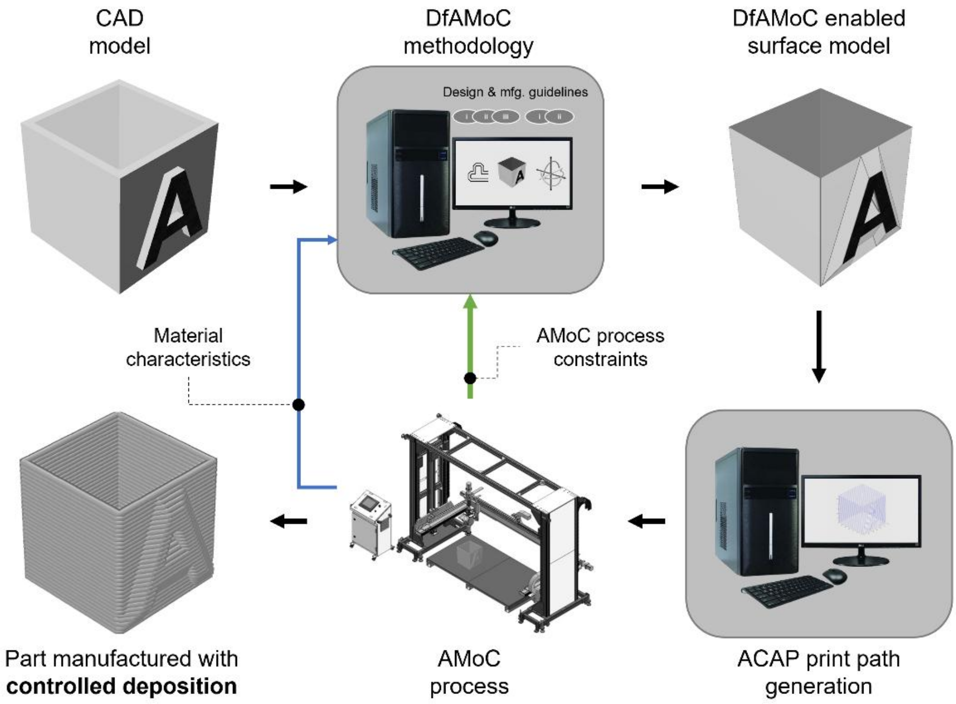

Figure 2.8 Additive manufacturing of concrete using DfAMoC and surface-based slicing method

2.4. AMoC with DfAM: Examples of planar and non-planar geometries

This section analyzes the implementation of design and manufacturing guidelines, specified in Section 2.3, with the help of three case studies. Firstly, a 2.5D geometry is defined by planar surfaces, whereas the subsequent case investigates fully 3D geometries featuring non-planar surfaces. The third case extends this examination to encompass complex 3D geometries, including detailed surface features like embossing and debossing. All examples illustrate applications of the suggested design and manufacturing guidelines to the distinct geometric features, ensuring enhanced manufacturability using 10 mm layer height and 25 mm bead width.

2.4.1. 2.5D or planar geometry

In the AM process, 2.5D objects are characterized by a uniform or unchanged cross-sectional profile extruded along a designated axis, typically the vertical or Z-axis. In contrast to fully three-dimensional shapes, 2.5D geometry lacks intricate variations or overhangs in the vertical dimension.

For 2.5D or planar geometries, the print head's center path must be precisely defined. This path can be carefully sketched in any CAD software and then extruded to form a 2.5D surface model.

Figure 2.9(a) shows a 2.5D model with 25 mm thickness and how it should be initially oriented following the manufacturing guideline I to determine the correct print direction. The geometry's outer surface was then offset inward by 12.5 mm using the design guideline I to accommodate a 25 mm bead width and 10 mm layer height, as shown in Figure 2.9(b). Following that, manufacturing guideline II was used to generate an ACAP toolpath that minimizes nozzle lifts, as seen in Figure 2.9(c). Before applying design guideline III, the ACAP toolpath was extruded to match the entire height of the 2.5D geometry, as shown in Figure 2.9(d). Then, design guideline III eliminates sharp junctions from the surface model, improving flow continuity, as shown in Figure 2.9(e). The design guideline II is not applicable here as the geometry persists only on planar or 2.5D surfaces. Finally, the generated surface model was exported as an .STL file for further processing in the AMoC workflow.

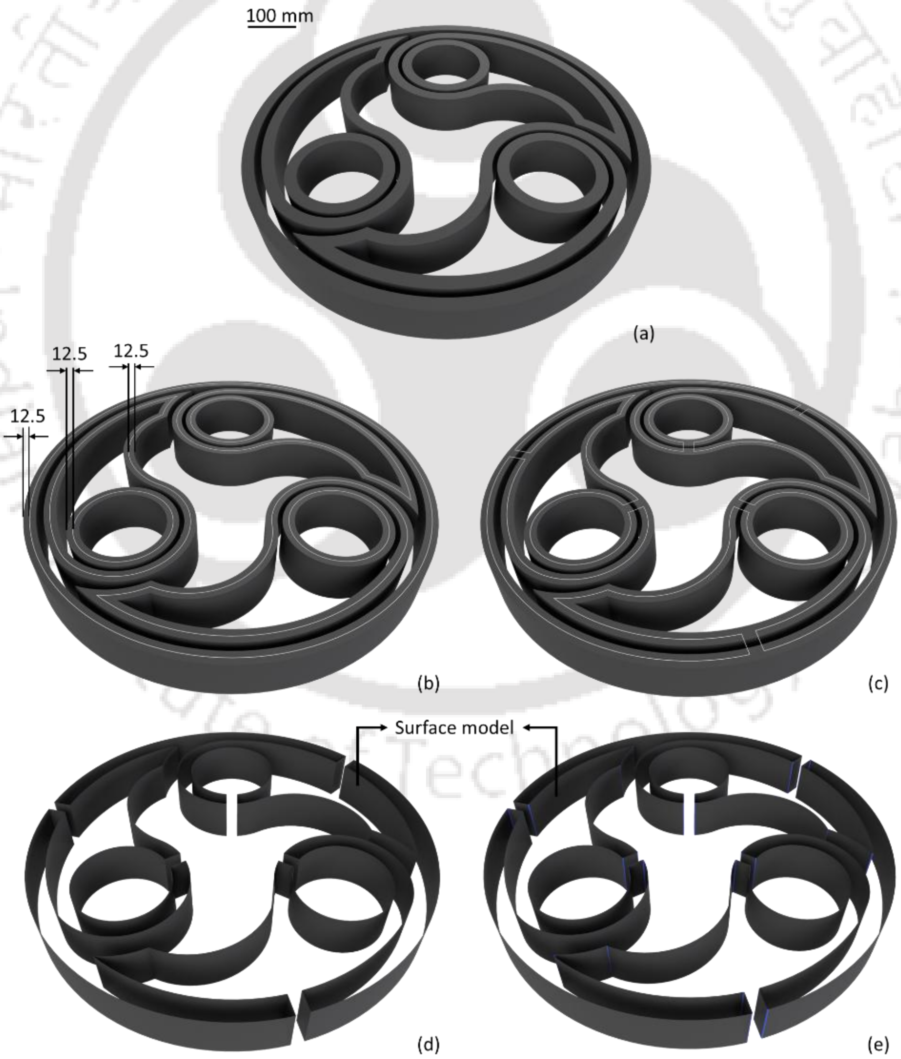

Figure 2.9 Stepwise development of 2.5D surface model for AMoC:(a) Orientation selection, (b) Surface offset for 25 mm bead width and 10 mm layer height, (c) ACAP toolpath generation, (d) Extrusion of the ACAP path to the full geometry height, and (e) Sharp junctions elimination

2.4.2. 3D or non-planar geometry

In the AM process, 3D parts are characterized by intricate, non-planar surfaces that exhibit continuous variation across all three dimensions - X, Y, and Z. These geometries frequently incorporate curves, overhangs, and freeform shapes, making them more challenging to manufacture. Manufacturing complex 3D geometries with AMoC necessitates precise surface design to ensure that each layer is adequately supported by the one beneath it, as no support structures are used in this process. *Figure 2.10(a)* depicts a representative solid model of a non-planar geometry with a wall thickness of 25 mm. This is then transformed into a surface model of the print head's central path by applying the design and manufacturing guidelines.

All the guidelines from Section 2.3 were implemented in a specific order, with a special focus on the design guideline II. The design process was initiated with design guideline II to ensure structural stability, which restricts non-planar surfaces' maximum inclination and print height within the acceptable limit (refer to *Figure 2.4(a)*). *Figure 2.10(b)* illustrates the angle of the non-planar surfaces, which is 21.8 degrees relative to the vertical (side view) and 100 mm in print height (well within the design limits for 10 mm layer height and 25 mm bead width).

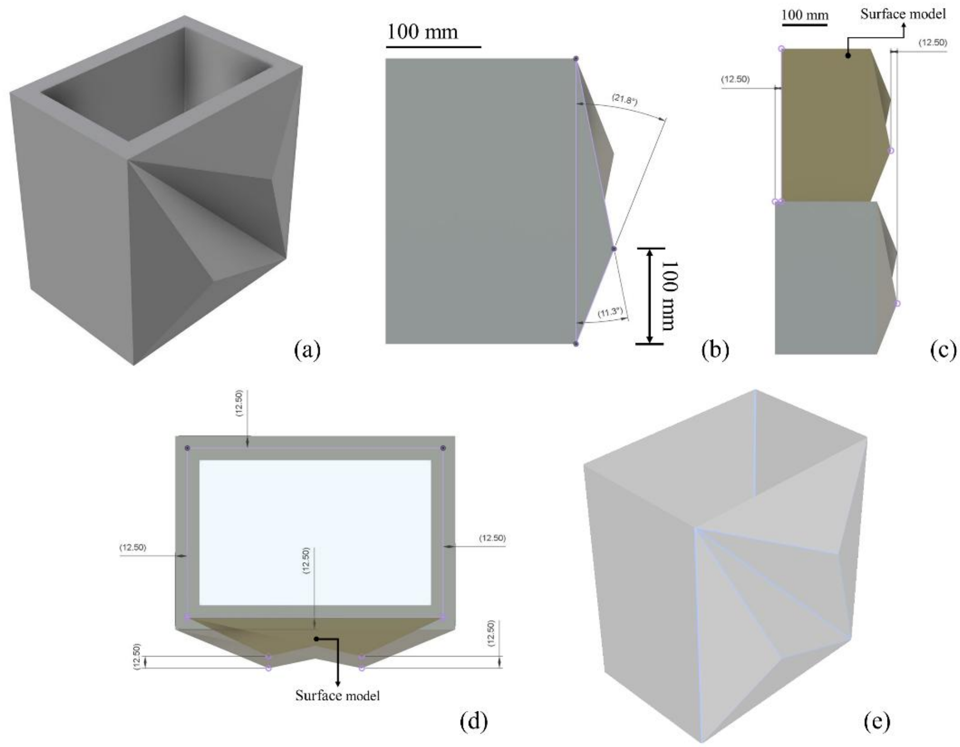

Figure 2.10 (a) CAD model of non-planar geometry, (b) Inclination of the non-planer surfaces from the vertical (side view), (c) and (d) Outer surface of the geometry offset inward by a distance equal to half of the bead (here, 12.5 mm is offset distance) [c: Side view (1:2) & d: Top view], and (e) Surface model of non-planar geometry

The subsequent guidelines were applied meticulously upon satisfying the inclination and printing height conditions for surface model generation. The model was further oriented according to the manufacturing guideline I to ascertain the suitable print orientation for printing, as shown in *Figure 2.10(a)*. Subsequently, the outside surface of the geometry was offset inward by 12.5 mm according to design guideline I to accommodate the bead width of 25 mm and layer height of 10 mm, as shown in *Figure 2.10(c)* and *Figure 2.10(d)*. It may be noted that the manufacturing guideline II was already implemented here due to the closed-loop contour of the geometry, which ensures an ACAP toolpath. Thereafter, design guideline III was executed to eliminate sharp junctions from the surface model (blue shows the applied fillet at every sharp junction of the surface model), as shown in *Figure 2.10(e)*. Finally, the generated surface model for non-planar geometry is exported as an .STL file for further processing in the AMoC workflow.

2.4.3. 3D or non-planar geometry with embossed and debossed features

3D or non-planar geometry with embossed and debossed features is a surface that varies in all three dimensions (X, Y, and Z) with embedded raised (embossed) or recessed (debossed) features into its form. These features add texture details (such as letters, logos, or patterns) on planar or non-planar surfaces. These features were found to also increase structural strength, material efficiency, and 3D printability (Sadakorn et al., 2024). When paired with internal supports, these features improve modular performance and accuracy (Yabanigül & Gulec Ozer, 2024). They also help to achieve sustainability goals by improving thermal behaviour and resource efficiency (Prasittisopin, 2024). Studies suggest these features suit small-scale construction and dry-assembly approaches (Sadakorn et al., 2022). When integrated into DfMA procedures, the 3D patterned surfaces allow for efficient part production with design flexibility (Tuvayanond et al., 2023). Printing such geometries in AMoC is difficult because the surfaces must be self-supporting while accurately replicating the delicate features of embossed or debossed elements. This requires prioritizing the surfaces of embossed or debossed features, focusing exclusively on those projected onto a horizontal plane. The defined regions specify the important surfaces for the fabrication of such parts.

Figure 2.11(a) illustrates the IITG embossed CAD model. *Figure 2.11(b)* and *Figure 2.11(c)* highlight the surfaces in red, showing the areas that will be projected on the horizontal plane. *Figure 2.11(d)* demonstrates the bottom surfaces of the IITG embossed feature projected onto a yellow horizontal plane, with the projected area indicated in black.

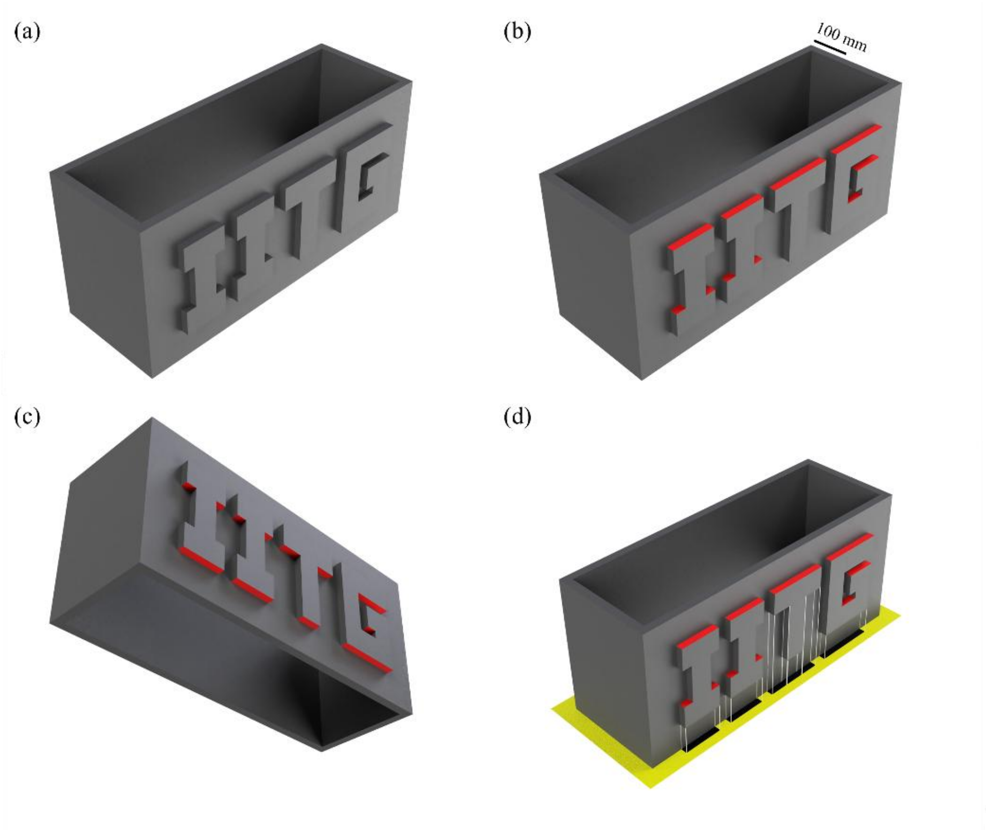

Figure 2.11 (a) IITG embossed CAD model, (b), and (c) All surfaces in red color will exhibit a projecting area when projected onto a horizontal plane, and (d) Bottommost surface of IITG has been projected onto a yellow colored horizontal plane, and the projected area is shown in black color.

For the generation of the surface model, the model was initially oriented according to the manufacturing guideline I, as shown in *Figure 2.11(a)*. Subsequently, the outside surface of the geometry was offset inward by 12.5 mm according to design guideline I to accommodate the bead width of 25 mm and layer height of 10 mm, as shown in *Figure 2.12(a)* and *Figure* 2.12*(b).* In contrast, offsetting the outer surface with a minimal horizontal thickness for embossed and debossed features is essential for a practical and feature-rich printing process. The font thickness must equal or exceed the specified bead width at all points to prevent material overlapping during deposition. *Figure 2.12(b)* also demonstrates that, with a bead width of 25 mm, the minimum horizontal thickness is established at 39.69 mm. *Figure 2.13* highlights the critical need to meet minimum thickness requirements, illustrating how insufficient width can lead to bead overlaps that result in missing debossed features. At higher heights, this overlap causes lateral strains in the XY plane, potentially resulting in collapse during manufacturing. *Figure 2.12(c)* illustrates the isometric view of the model (bottom) and surface model (top).

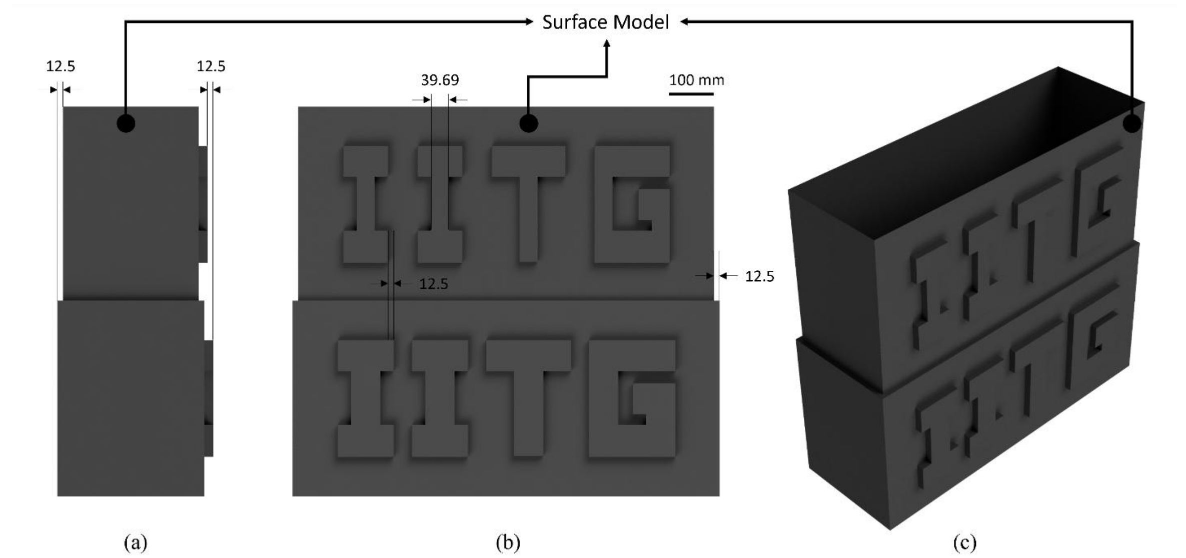

Figure 2.12 The outer surface of the geometry (bottom) is offset inward by a distance equal to half of the bead (here, 12.5 mm is the offset distance). (a) Side view, (b) Front view, and (c) Isometric view of the geometry (bottom) and surface model (top)

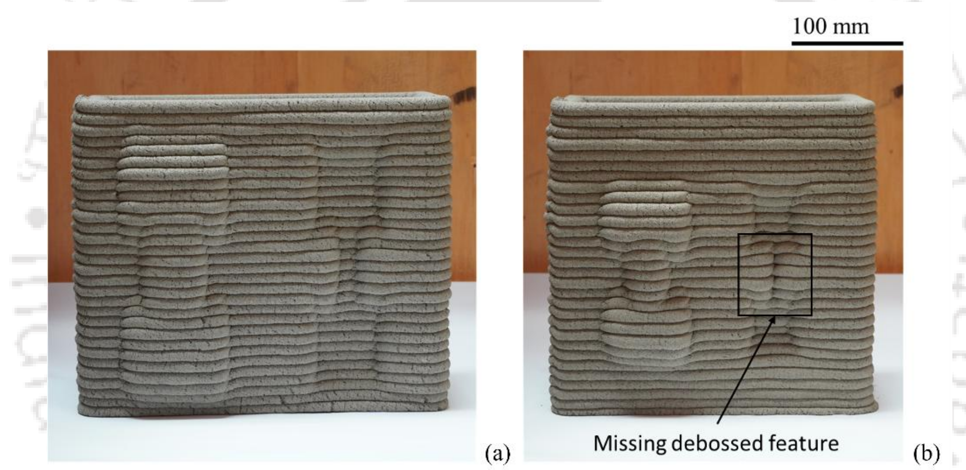

Figure 2.13 Non-planar geometries with embossed and debossed features (a) Minimum font thickness 39.69 mm (b) Minimum font thickness 18 mm

The design guideline II was implemented to ensure adequate layer support for embossed and debossed features throughout the printing process. This involves providing a chamfer on essential surface junctions that project onto a horizontal plane identified previously to create a control angle of inclination within acceptable limits (refer to *Figure 2.4(a)*). *Figure 2.15* demonstrates the implementation of chamfering (chamfered junctions shown by white color) on critical surface joints, attaining an inclination angle of 21.8 degrees, within the set range of 10 mm layer height and 25 mm bead width. In this case, the manufacturing guideline II was automatically implemented because of the closed-loop contour of the geometry, which ensures an ACAP toolpath. Following manufacturing guideline II, the design guideline III was implemented by providing fillets at the required sharp junctions of the surface model; *Figure 2.14(b)* shows the applied fillet on the surface model in blue. Finally, the generated surface model for non-planar geometry is exported as an .STL file for further processing in the AMoC workflow.

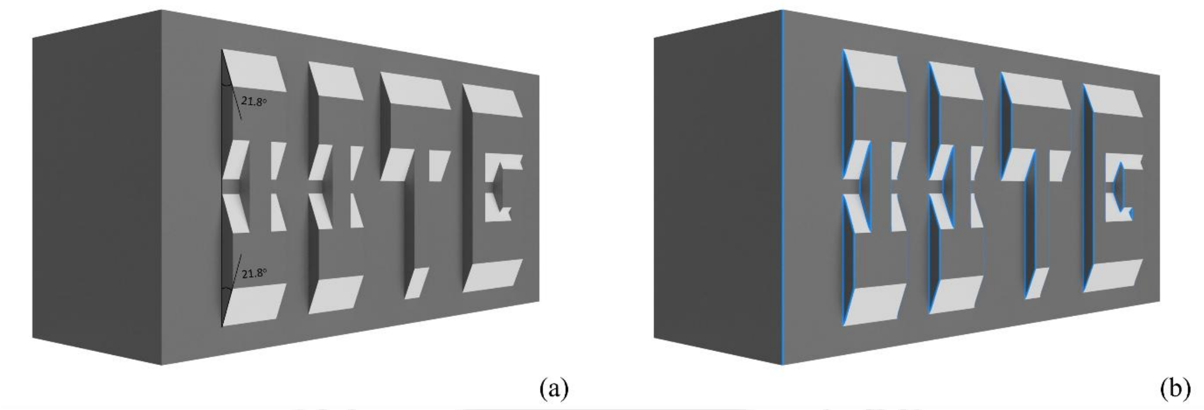

Figure 2.14 (a) Required surface joints have been chamfered such that the inclination angle from vertical is within the described limit (21.8 degrees), and (b) Surface model of non-planar geometry

The above methodology is summarized in *Table 2.4*, which outlines the sequence of design and manufacturing guidelines to create the surface model of a given geometry for AMoC.

Table 2.4 Guideline sequence for creating the surface model for AMoC

Geometry type	Guidelines sequence
2.5D or Planar	Manufacturing guideline I → Design guideline I → Manufacturing guideline II → Design guideline III
3D or Non-planar	Design guideline II → Manufacturing guideline I → Design guideline I → Manufacturing guideline II → Design guideline III
3D or Non-planar with features	Manufacturing guideline I → Design guideline I → Design guideline II → Manufacturing guideline II → Design guideline III

2.5. Experimental validation and discussions

Table 2.5 provides a summary of the geometries evaluated under DfAMoC guidelines, as well as critical phases of the AMoC workflow, encompassing solid modeling, DfAMoC-enabled surface modeling, slicing & G-code generation in MATLAB, simulation utilizing open-source tools (NC Viewer, 2025), and the realization of the printed components. The results confirmed the robustness and adaptability of the DfAMoC framework for obtaining structural integrity, reliability, and geometric precision in the 3D printed parts.

Table 2.5 Geometries and manufacturing process flow using DfAMoC guidelines

Geometry	Planar	Non-planar	Non-planar with embossing or debossing
Solid Model			
DfAMoC (surface model)		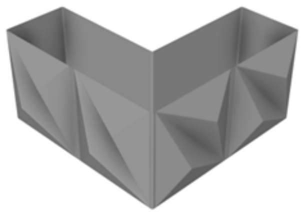	
Slicing and G-code generation in MATLAB	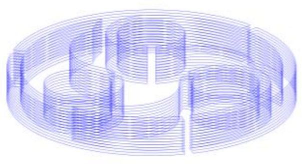	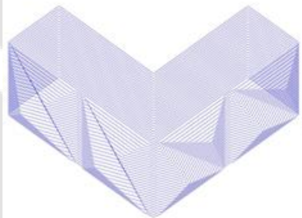	
G-code Simulation NC Viewer (2025)	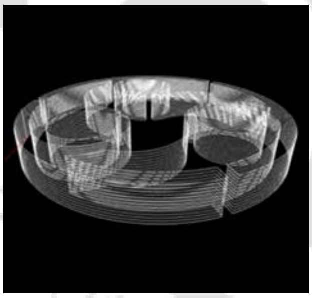	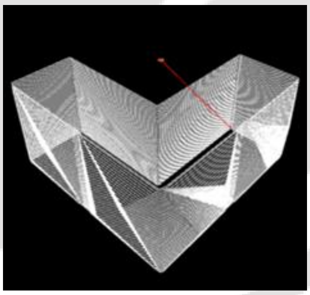	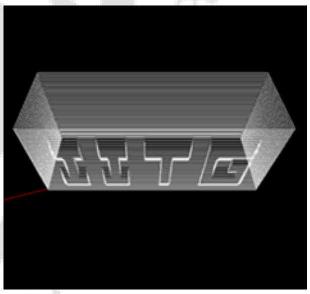
Realization (3D printed parts)			

Additional examples of the three geometry types—2.5D or planar geometry, 3D or non-planar geometry, and 3D or non-planar geometry with embossed or debossed features with different bead widths and layer heights are shown in *Figure 2.15* to demonstrate the versatility and robustness of the proposed methodology. The DfAMoC approach eliminates the need for additional scaffolding or support structures for the geometries, which are generally impractical in the AMoC process. When the geometric features of a part exceed the material's self-supporting capability, the part must be subdivided into distinct modules to ensure successful fabrication. *Figure 2.15(d)* demonstrates a case where the geometry has been split into three sections, each conforming to a maximum overhang angle of 20 degrees. Based on experimental results, the safe printable height corresponding to this inclination was determined to be 150 mm, assuming a layer height of 10 mm (i.e., 15 layers). This criterion guided the modular part printing, as the original geometry could not be printed entirely in a single attempt due to overhang characteristics and material constraints associated with the AMoC process. Therefore, each module was printed independently in its optimal orientation, then assembled post-printing to realize the complex form without the need for support structures. *Figure 2.15(g)* shows how a Yin-Yang was successfully embossed and fabricated onto a non-planar surface, illustrating the adaptability of the proposed method. This study indicates that embossed and debossed features can be successfully printed on planar and non-planar geometries using the proposed DfAMoC method.

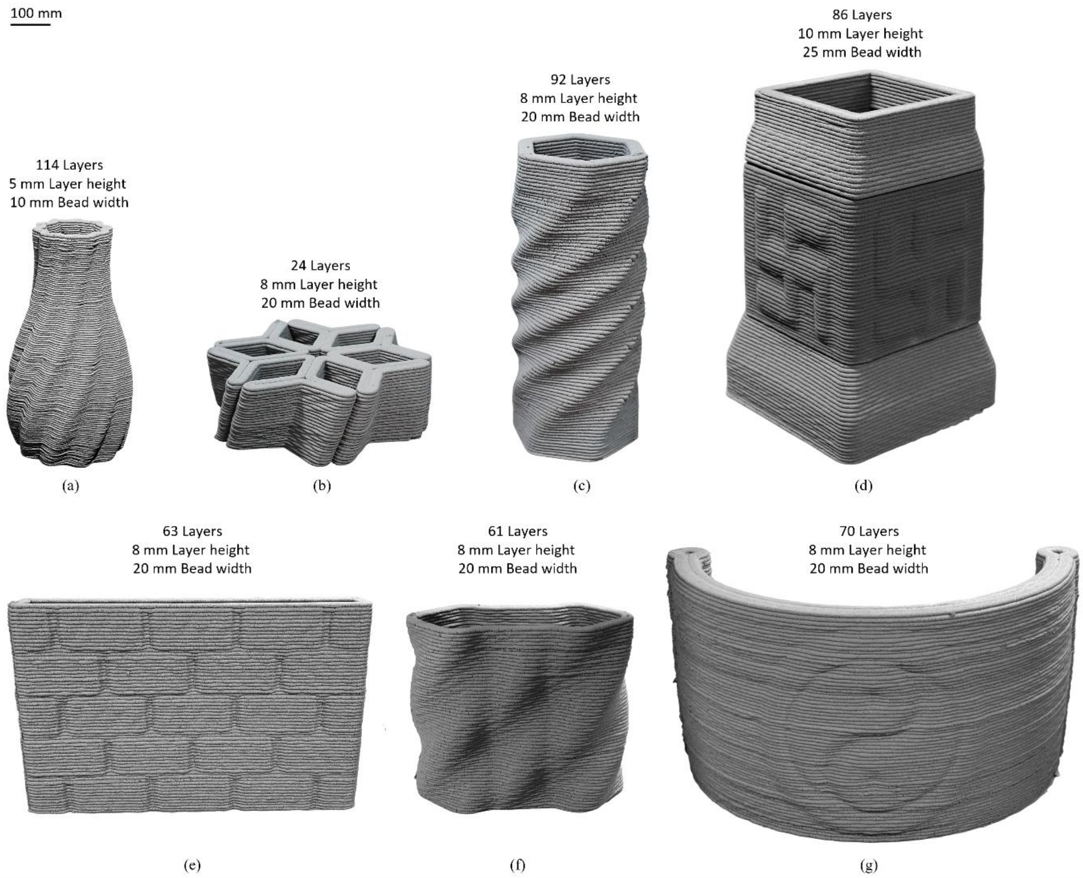

Figure 2.15 Examples of DFAMoC guided 3D printed concrete structures: (a) Flower vase: non-planar geometry, (b) Planter: non-planar geometry, (c) Vertical hollow column: non-planar geometry, (d) Traditional basil planter: a combination of planar, non-planar, and non-planar with feature geometries, (e) Brick patterned wall element, (f) A non-planar column formwork, and (g) Yin-Yang embossing on a non-planar surface.

The above examples demonstrate that the extrusion-based AMoC process has been successfully utilized in printing various geometries when guided by the DfAMoC design and manufacturing guidelines. The DfAMoC provides superior part quality (dimensional accuracy ±6 mm), toolpath continuity, and manufacturability without support structures. These findings enable more informed decisions in optimizing the part design in the AMoC process flow.

Following successful manufacturing, the dimensional accuracy of the additively manufactured concrete structures was investigated, and all the calculations were performed using the boundary box method, as shown in Figure A1.3 (Appendix). *Table 2.6* summarizes dimensional accuracy results for all the geometries, and all deviations are within the acceptable tolerance levels reported in several studies (Buswell *et al.*, 2022; Xu *et al.*, 2020).

Table 2.6 Dimensional accuracy of additively manufactured concrete structures

Geometry	**Bounding box**								
	Expected dimensions (mm) (CAD model)			**Actual dimensions (mm) (Printed part)**			**Deviation (mm)**		
	X_c	Y_c	Z_c	X_p	Y_p	Z_p	ΔX	ΔY	ΔZ
Flower vase	300	300	*570*	302.4	303.8	*569.7*	+ 2.4	+ 3.8	*- 0.3*
Planter for six plants	618	618	*192*	620.8	622.4	*192*	+ 2.8	+ 4.4	*0.0*
Vertical hollow column	310	310	*736*	314.8	314.2	*735.8*	+ 4.8	+ 4.2	*- 0.2*
Traditional basil planter	410	410	*860*	414.2	413.8	*859.6*	+ 4.2	+ 3.8	*- 0.4*
Brick-patterned wall element	*800*	*110*	*504*	*802.5*	*111.8*	*504.0*	*+ 2.5*	*+ 1.8*	*0.0*
Non-planar column formwork	560	250	*488*	562.8	255.8	*487.8*	+ 2.8	+ 5.8	*- 0.2*
Yin-Yang embossing	900	480	*560*	905.2	484.2	*559.5*	+ 5.2	+ 4.2	*- 0.5*

Splitting strength tests were performed at 28 days on three specimens to assess the mechanical performance of the printed structures. The extracted specimens from concrete structures were tested in a UTM machine, where samples were positioned between two cylindrical steel heads and compressed at a constant rate of 100 N/s until failure, as mentioned in earlier studies (Zareiyan & Khoshnevis, 2017; Srinivas *et al.*, 2025). *Figure 2.16* shows the interlayer strength of printed specimens, and experimental results confirm strong and consistent layer bonding of all printed specimens, suggesting robustness of the proposed methodology. Nevertheless, it may be noted that the interpretations of this study are contingent upon the material composition and part design. Changes to the printing parameters, such as layer height, bead width, print speed, or adjustments in material composition, would need a reassessment of the experimental parameters. This entails recalibrating the inclination angle range, reassessing the requisite printable height of the non-planar layers, and performing supplementary tests to confirm the modified design under the new conditions.

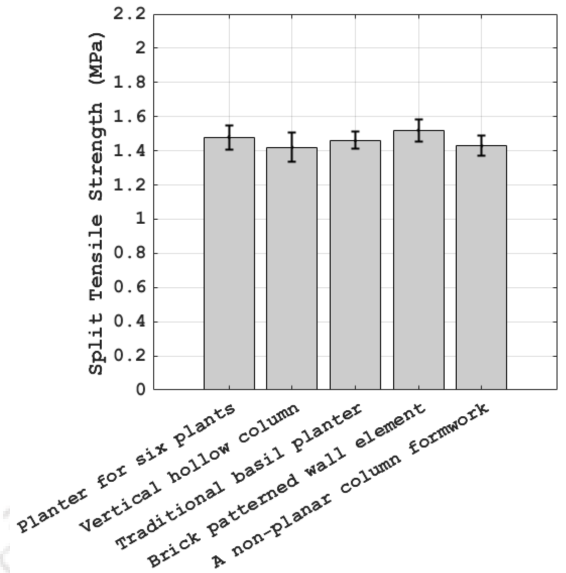

Figure 2.16 Interlayer bond strength of the specimens extracted from additively manufactured concrete structures obtained via the splitting test

2.6. Summary

The proposed framework - DfAMoC was successfully applied to design three geometry types: planar, non-planar, and non-planar with embossed and debossed features, considering a three-axis gantry-based AM system. This method adheres to experimentally determined limitations of overhang angles relative to print height, facilitating the creation of intricate functional surfaces without additional support structure. The deposited material paths minimize nozzle lifts and non-extrusion movements, reducing idle time and improving interlayer bonding. Moreover, the printed parts' interlayer bond strength and dimensional accuracy are determined to ensure a fully optimized part. Experimental results confirmed dimensional deviations of the parts within ±6 mm of their CAD models. Splitting tensile strength ranging from 1.42 MPa to 1.52 MPa for different printed structures further indicates a strong and consistent interlayer bonding.

By embedding experimentally derived printability limits and continuous toolpath strategies into the design stage, the DfAMoC framework enables support-free fabrication of complex non-planar concrete geometries with controlled dimensional accuracy (±6 mm) and reliable interlayer strength (≈1.5 MPa). This demonstrates a practical pathway for translating AMoC from laboratory-scale demonstrations toward architectural and large-scale construction applications.

Chapter 3: Investigation into a TSP-based Toolpath Strategy for Area Filling

This chapter investigates the implementation of a TSP-based toolpath strategy for solid structure area filling. The approach is designed to enhance isotropy, minimize non-productive travel, and ensure continuous deposition paths. Comparative analysis with conventional infill strategies demonstrates the benefits and limitations of the TSP approach in the context of AMoC.

A portion of this chapter has been published:

Sahu, A., & Panda, B. (2025). A TSP-based continuous path planning for additive manufacturing of concrete. *Progress in Additive Manufacturing*, 10(4), 2205-2226. *https://doi.org/10.1007/s40964-024-00746-2*

3.1. Abstract

The advent of additive manufacturing of concrete technology has emphasized the critical role of toolpath strategies in construction efficiency and part quality. However, most of the current toolpath solutions are inefficient and lack the adaptability to meet the scale and material challenges of concrete extrusion. In response, this chapter draws inspiration from TSP and proposes continuous toolpath strategy for (solid) space-filling applications. Compared with control groups that focuses on non-continues toolpath, the proposed method provides better print quality, less sharp turns, and reduced anisotropic strength. The effectiveness of this method is demonstrated through generation, printing, and (experimental and numerical) evaluation of different planer design examples. Moreover, by leveraging on optimization techniques such as contour offset and boundary trim, the TSP-based toolpath effectively mitigates underfilling while ensuring structural integrity of the printed structures. The TSP-based toolpath is combined with a sharp turn removal technique to ensure continuous and smooth concrete deposition. An example of additively manufactured topology-optimized design is presented by combining with TSP-based toolpath at the end of this chapter, illustrating the applicability and scalability of the proposed method for efficient, cost-effective construction scale additive manufacturing.

3.2. Toolpath planning methodology

The travel-path optimization problem of discontinuous paths belongs to the category of generalized TSP. The TSP is a widely recognized combinatorial optimization problem in computer science and mathematics. It has been applied in diverse fields, including manufacturing (Khodabakhshi et al., 2022), job shop sequencing (Silva et al., 2002), computer wiring (Lenstra & Kan, 1975), pick-up and delivery (Mosheiov, 1994), and search algorithms (Osterman & Rego, 2003) and (Ulder et al., 1991) due to its versatile applicability and problem-solving nature.

In AMoC, TSP can be an effective toolpath strategy to generate continuous area-filling curves. The suggested technique ensures seamless continuity, maintains step-over distance constant, reduces turns, and emphasizes its attention on computational efficiency. The solutions to the TSP problem can be classified into two main categories: exact algorithms and heuristic techniques. This paper investigates the Lin-Kernighan (LK) method, a type of heuristic algorithm known for its simplicity but lacks the guarantee of producing ideal tours. In contrast to fixed-value λ-opt algorithms, which optimize tours by exchanging edges, the LK algorithm employs a dynamic approach by iteratively adjusting the value of λ. This adjustment assesses whether reconfiguring the tour might lead to a shorter distance. The LK algorithm is a toolpath planning technique for the TSP. A feature called the 'variable λ-opt' algorithm enhances its adaptability and effectiveness. Keld Helsgaun originally designed the LK algorithm and has been successfully implemented as LKH (Helsgaun, 2000). This LKH (Lin-Kernighan-Helsgaun) algorithm extends the LK heuristic by a series of search steps and sensitivity analysis to enhance the search for an ideal solution (Lin et al., 2015). In this study, we utilized the LKH solver, a component of the comprehensive open-source solver 'Concorde,' developed by the University of Waterloo in Canada (University of Waterloo, n.d.).

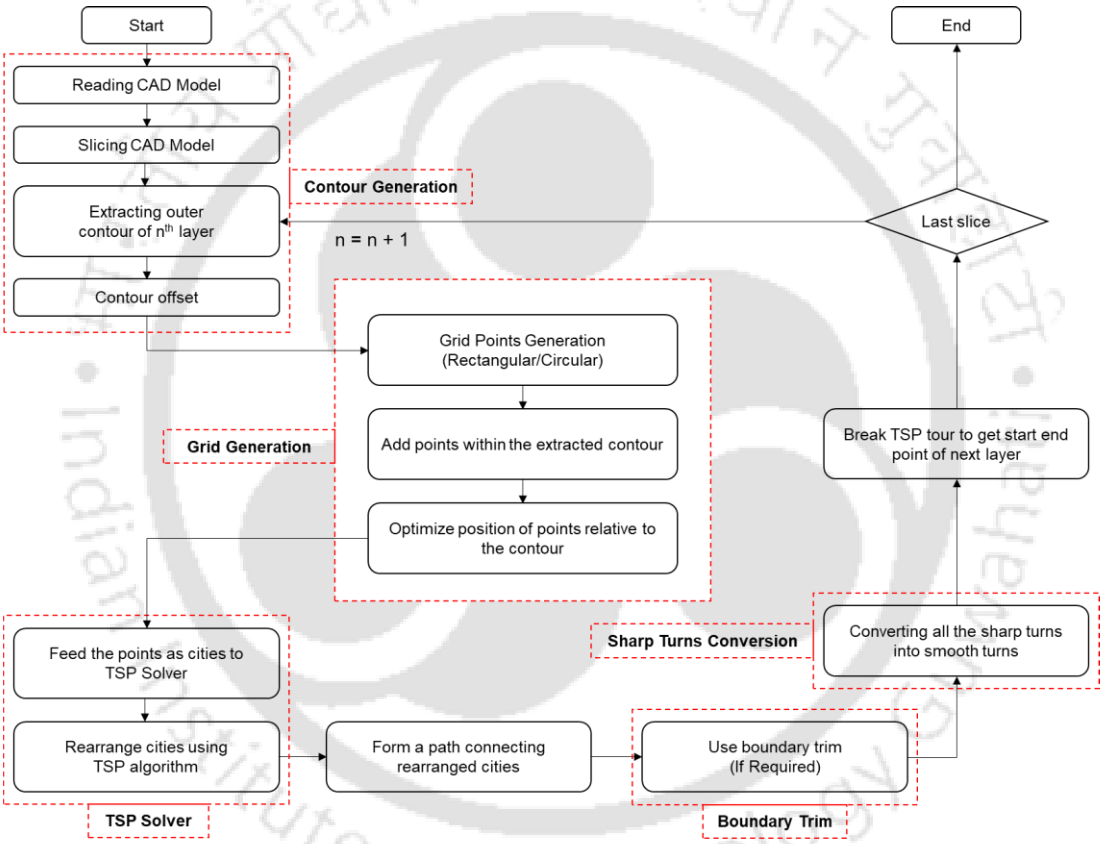

Figure 3.1 Design-to-Print framework for extrusion-based AMoC toolpath generation using TSP solver

This study executes the TSP path-planning strategy using a two-stage approach. A contour is created to create grids, and the internal area is approximately filled using a discrete and precisely defined array of points. In the second stage, a sequential route that satisfies the specified optimization goals within the region populated with grid points is determined. The proposed two-stage method comprises five sequential steps. The process begins with (a) contour generation, followed by (b) grid generation, (c) TSP solver, (d) boundary trim, and concludes with (e) sharp turns conversion. *Figure 3.1* is a diagrammatic representation of the algorithm utilized in the study. The proposed method is implemented on a computing system featuring robust specifications to ensure efficient execution and accurate results. The system has an 11th Gen Intel(R) Core (TM) i7-11700K processor with a base frequency of 3.60GHz. It also has a 32 GB RAM capacity, providing sufficient memory resources for complex computational tasks. The system was integrated with an NVIDIA T600 graphics card with a 4GB GDDR6 VRAM and a 128-bit memory interface to enhance its graphical processing capabilities. This robust hardware configuration not only ensures the swift execution of algorithms but also makes the method adaptable to computationally intensive tasks. As a result, it contributes to the accuracy and dependability of research outcomes.

A streamlined toolpath generation process used in this work is shown in *Figure 3.2*. The process begins by dividing the STL-format CAD model into several layers (*Figure 3.2(a)*). Ensuring dimensional accuracy, the subsequent step involves contour offsetting (*Figure 3.2(b)*). Following this, grid points are generated, and a geometric contour corresponding to a given layer is superimposed on this grid (*Figure 3.2(c)*). Subsequently, grid points inside or near the border are retained, while those outsides are eliminated (*Figure 3.2(d)*). These chosen grid points then serve as cities for the TSP solver, which constructs a toolpath based on specified criteria (*Figure 3.2(e)*). In the final step, the toolpath was trimmed to align with the original contour, and every sharp turn of the toolpath was converted to a smooth turn for continuous and smooth movement of the printhead throughout the printing process (*Figure 3.2(f)*).

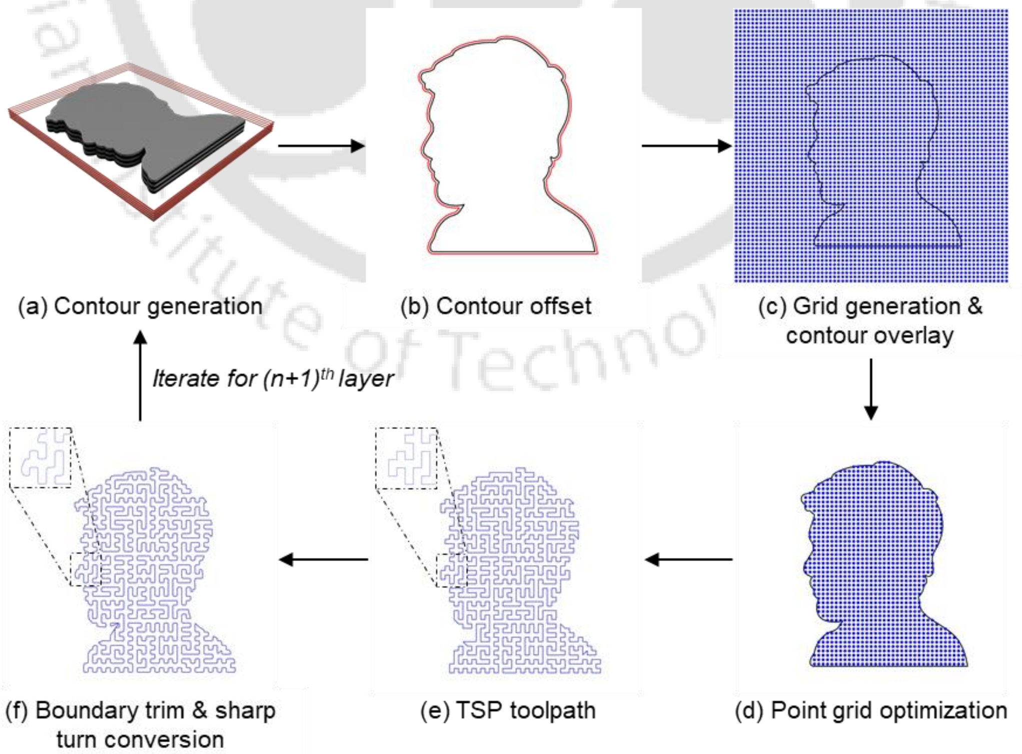

Figure 3.2 Process flow for TSP toolpath in extrusion AM of concrete

3.2.1. Contour generation

In AMoC, offsetting the exterior contours in the inward direction and inner contours in the outward direction can help to enhance the manufactured object's dimensional accuracy. This step considers the material deposition process and possible deviations during the 3D printing by shifting the contour inward or outward by 'half the value of bead-width (W), i.e., 0.5*W' (*Figure 3.3*).

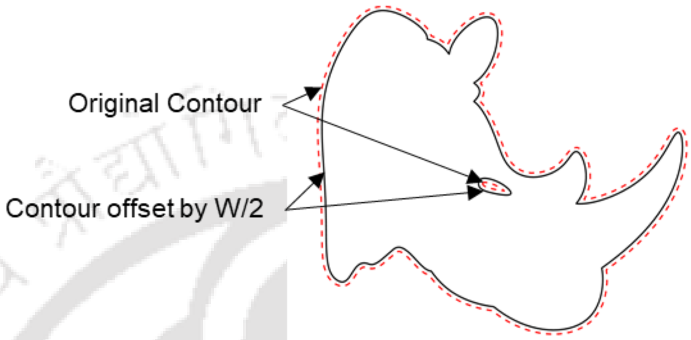

Figure 3.3 Original contour is in red, and the offset contour is in black color

3.2.2. Grid generation

The grid point arrangement significantly affects the toolpath's overall characteristics. This study has investigated rectangular and circular grid point arrangements. *Figure 3.4(a)* shows the initial scenario, in which grid points are arranged in a rectangular pattern (length and width both are equal to 's'), while *Figure 3.4(b)* shows the circular arrangement.

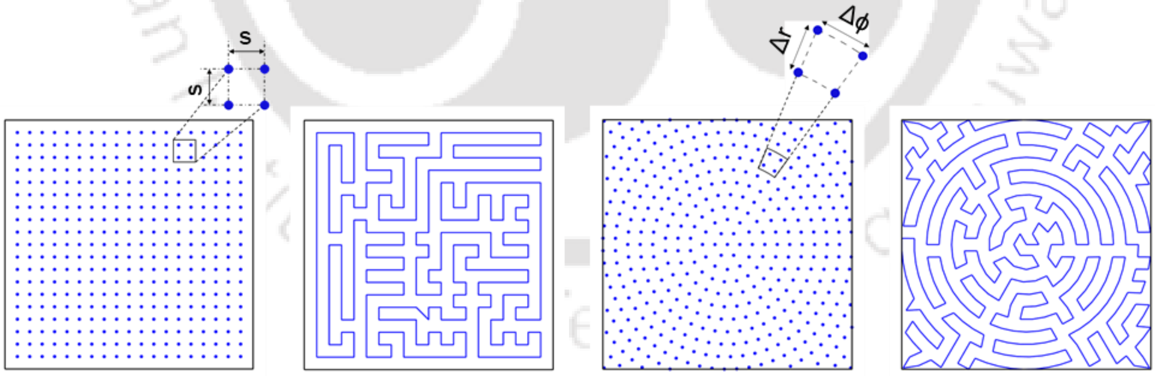

(a) (b)

Figure 3.4 For square geometry (a) Rectangular grid points, (b) Circular grid points

Figure 3.4 shows that TSP-based path planning results in many turns. Such turns are avoided during construction as they cause unnecessary decelerations during material deposition. The potential for these rapid decelerations to unintentionally change crucial process parameters linked to material deposition makes the scenario more worrying, especially in the absence of closed-loop feedback control systems. The structural integrity and quality of the finished printed part may suffer as a result of such unintentional fluctuations in the printing process, which is not desired in AMoC. On the other hand, there are instances in which intentionally including a specific number of turns might be helpful. These turns have a significant role in improving the printed part's homogeneity. The toolpath should predominantly favor a single direction to minimize the number of turns. A TSP framework can achieve a toolpath adjustment by simply changing the distance between the grid points or cities. For instance, changing the width between two adjacent points on a rectangular grid while maintaining a constant length will tilt the toolpath to give preference to movement in the "width" direction. *Figure 3.5* and *Figure 3.6* elegantly illustrate this phenomenon. A crucial parameter in this context is the 'step-over value s,' which expresses the distance between subsequent grid points as a multiple of that value. *Figure 3.6* shows how the number of turns in a contour changes based on the placement of grid points. The direction-preference strategy to reduce the separation width between adjacent grid points results in a toolpath with fewer turns.

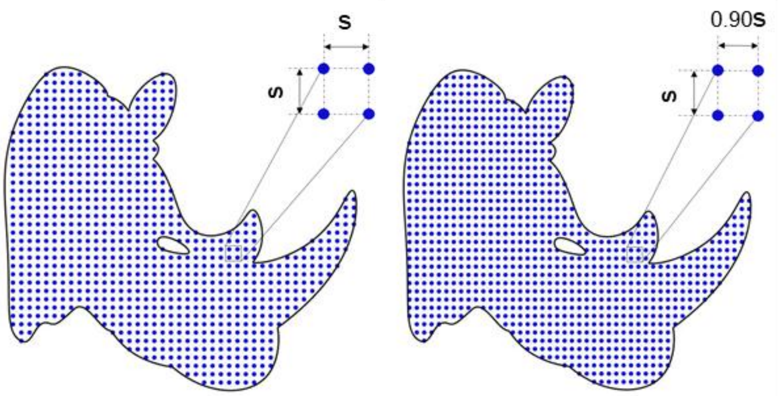

(a) (b)

Figure 3.5 Grid points in (a) Square and (b) Rectangular format with cells 0.90 times the length

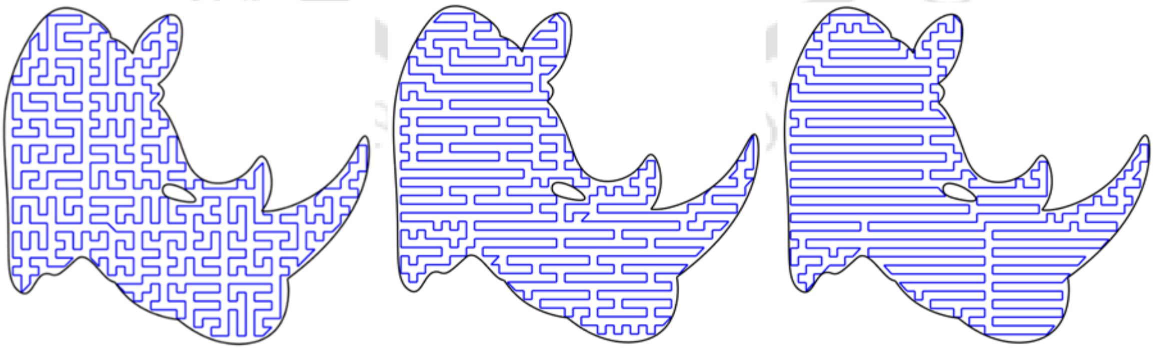

(a) (b) (c)

Figure 3.6 Decreased cell width (W) caused a reduction in turns: (a) W=s, (b) W=0.95s, (c) W=0.90s due to direction favoring.

Similar to a rectangular grid case, a circular grid's cell size can result in toolpath preference in one direction over another. In a circular grid, the size of each cell is determined by the radial and azimuthal distances. The symbol 'a' represents the count of points along the azimuth direction corresponding to a specified radius. On the other hand, the spacing between the succeeding radii is represented by the symbol Δr.

$$Radial\ distance\ \Delta r\ \approx\ s\beta \tag{3.1}$$

$$Azimuthal\ distance\ \Delta\phi\ \approx\ s\alpha \tag{3.2}$$

For a given *'r,' the number of points along ϕ,*

$$a\ =\ \left\lceil\frac{2\pi r}{s\alpha}\right\rceil \tag{3.3}$$

Where, *s* stands for step-over and *r* stands for radius, β and α control the spacing between grid points along the radial and azimuthal directions, respectively, as depicted in *Figure 3.7*.

Eq. (3.3) defines the denominator as the arc length between two adjacent grid points separated by a step-over distance (s). As the radius 'r' increases, it is essential to increase the number of points along the azimuthal direction 'ϕ' while keeping a consistent step-over distance. This adjustment guarantees that the distance between any two points within the ϕ direction remains constant for a given r value. The ceiling function is employed to approximate the point count to the nearest integer value for precision.

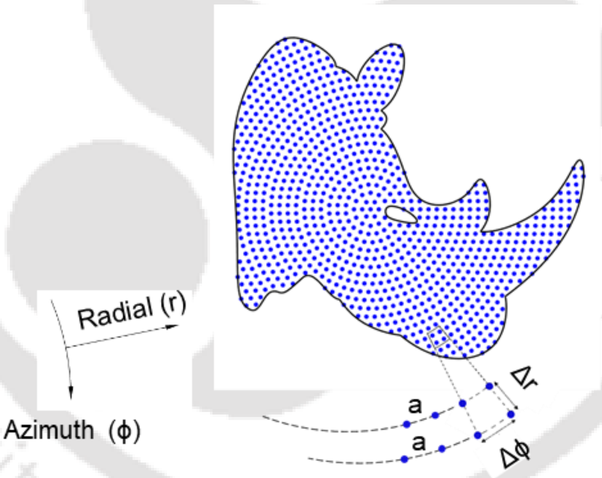

Figure 3.7 For generating a geometric contour, the orientation of circular grid points.

Eq. (3.1) indicates that decreasing the value of β reduces the distance between neighboring grid points along the radial direction. Consequently, the TSP-based toolpath is inclined to traverse more frequently in the radial direction. Conversely, lowering the value of α, as depicted in *Eq. (3.2)*, augments the count of points along the azimuthal direction. This increase results in smaller separations between adjacent points, facilitating finer resolution in the azimuthal direction. As a result, azimuthal is prioritized over the radial direction in the circular grid toolpath, as shown in *Figure 3.8.*

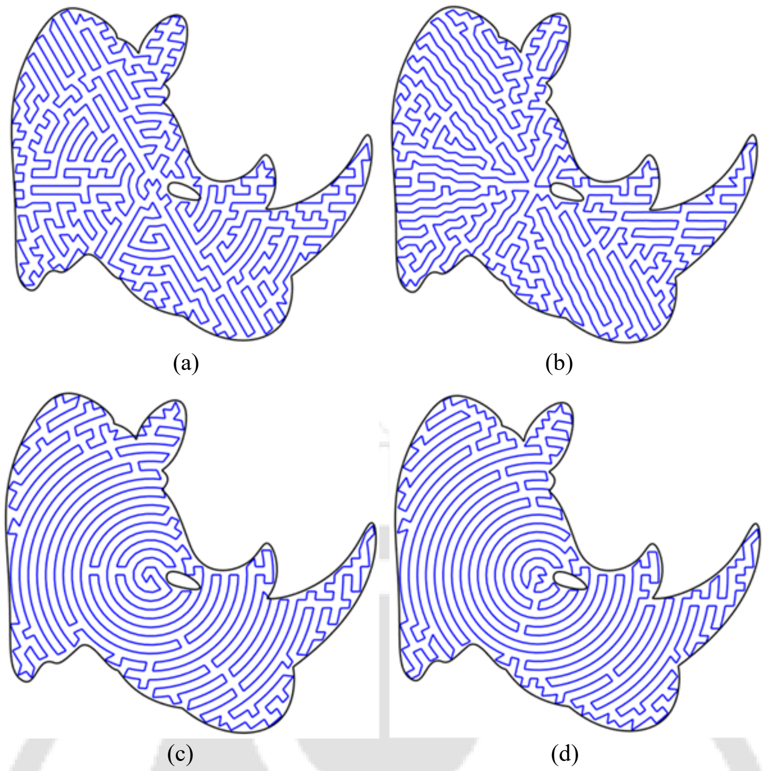

Figure 3.8 As β decreases, the radial direction is preferred, while as α decreases, the azimuthal direction is preferred; (a) α = 1.00; β = 0.95, (b) α = 1.00; β = 0.90, (c) α = 0.95; β = 1.00, and (d) α = 0.90; β = 1.00.

3.2.3. Grid fitting

The efficiency of the TSP-based area-filling toolpath in maximizing area utilization is significantly impacted by the spatial configuration of geometric contours surrounding grid points. *Figure 3.9* depicts the arrangement of circular geometric contours encircling square grid points, where the size of each cell matches the step-over distance. The diagram illustrates the minimum distance *(b_1...b_5)* from a border location (highlighted by a red circle) to the nearest neighboring grid points *(1...5)* within the border. The amount by which a deposited track extends beyond the border is represented by the term spillage 'd'.

$$d = (s - b_1)^2 + (s - b_2)^2 + (s - b_3)^2 + (s - b_4)^2 + (s - b_5)^2 \quad (3.4)$$

It should be noted that selecting particular grid points (located within the border and immediately adjacent to it) impacts variables b and d. The minimal perpendicular distance between each inner point and the border is determined. These points become essential in determining parameter *'d'* if this distance exceeds the defined step-over value. The Shapely package (Shapely, n.d.) was used in the Python computational environment to determine these distances. This unique subset of grid points, collectively known as *P*, is produced from the more extensive collection of grid points used in the TSP algorithm's execution.

The example given in *Figure 3.9* shows circular geometry aligned with a rectangular grid arrangement. A more general formulation of *Eq. (3.4)* can be used in cases of complex contours and non-uniform distribution of grid points as follows,

$$d = \sum_{all\ P}(s - b_{1\ldots P})^2 \qquad (3.5)$$

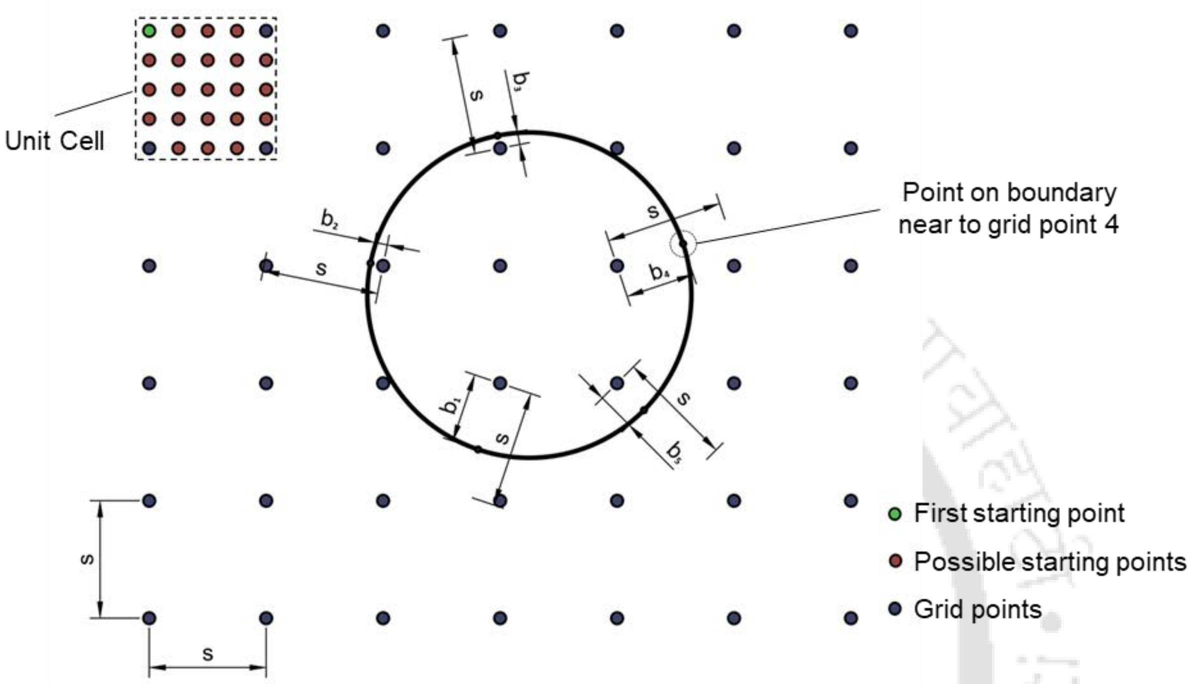

Figure 3.9 The arrangement of grid points relative to the boundary of an object.

The grid point array should be strategically positioned about the geometric contour to reduce the value of *d* (referred to as spillage in *Eq. (3.5)*). As shown in *Figure 3.10*, optimizing 'd' has twin effects on improving the geometric alignment of the deposited track and enabling more regular and uniform material deposition. Achieving an optimal configuration of grid points around the geometric contour is feasible by treating the grid point array and geometric contour as distinct layers. This involves determining the optimal position of the grid points by designating the array's starting point, with the layer containing the geometric boundary positioned atop the layer containing the grid points. Therefore, the optimization objective may be "searching for a starting point inside the unit cell that minimizes the leakage parameter *d*".

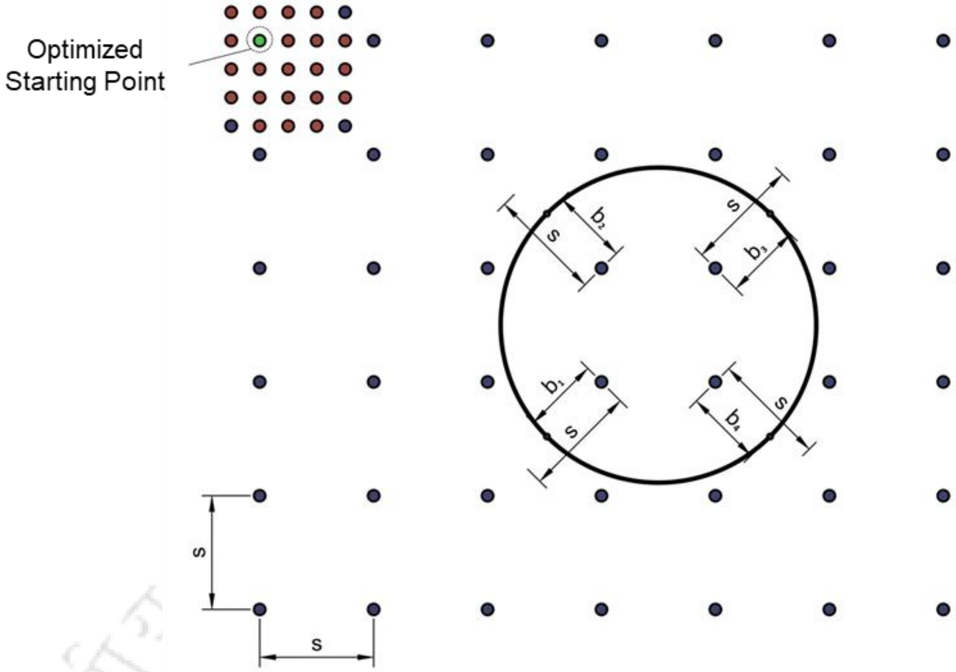

Figure 3.10 Optimizing the grid positioning about the object's boundary.

Following this optimization process, the grid configuration can be effectively adjusted, thus producing a toolpath that favors symmetry and uniform material deposition.

3.2.4. Boundary trim and sharp turn conversion

Figure 3.11 shows the trim algorithm (Kapil et al., 2016) for a particular shape, and its implementation is as follows. The process involves overlaying the geometric contour onto the grid points. Any points more than 0.5 steps away from the outer contour are then removed. This step ensures the availability of numerous grid points outside the outer contour for subsequent operations. Following this, the TSP algorithm generates the toolpath, which extends beyond the contours while adhering to predefined criteria. Subsequently, the toolpath points crossing the boundary upon exiting the geometric contour are identified, facilitating connections with other grid points. It is pertinent to note that both the toolpath's boundary data file and the grid points dataset encompass these junctions. Finally, within the toolpath, grid points outside the boundary are replaced with boundary points between the two junction points. This meticulous process results in the generation of the toolpath with boundary trim. The TSP-based toolpath encourages excellent part print quality when combined with the boundary trim technique.

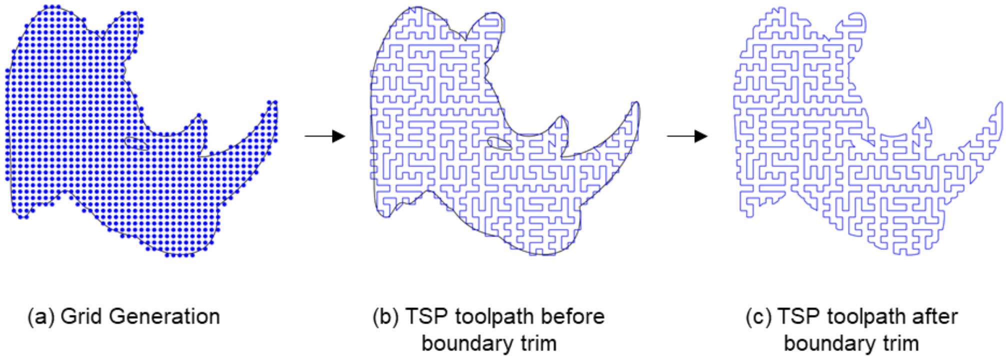

Figure 3.11 Boundary trimming affects the toolpath for a given geometric contour.

Sharp turns significantly impact the printed part quality, and such abrupt changes in the extrusion path will cause distortions in the extruded layers. Additionally, sudden changes in direction during the printing process sometimes generate vibrations that compromise the stability and accuracy of the printed part. A method is used in this study to eliminate sharp corners, and it is deployed via Rhino 7.0/ Grasshopper's visual programming language. After receiving the TSP toolpath as input as coordinates from an Excel file, the user can specify the 'fillet radius' at the sharp corner. This algorithm returns coordinates with the necessary amount of fillet at the sharp corner as its output. *Figure 3.12(a)* shows the toolpath with sharp turns, while *Figure 3.12(b)* and *Figure 3.12(c)* show the toolpath with 2 mm and 4 mm fillets (for rectangular grid).

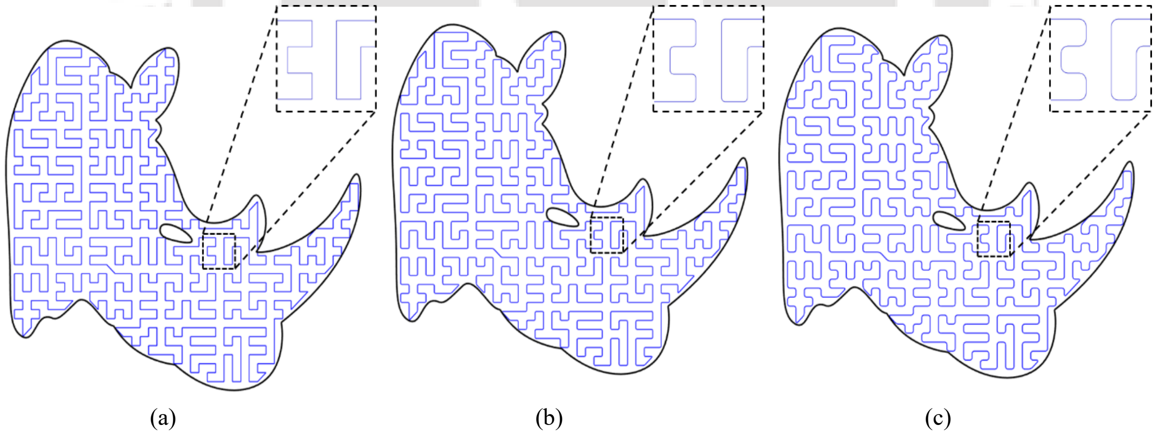

Figure 3.12 (a) TSP toolpath with sharp turns, (b) TSP toolpath with 2 mm fillet at sharp turns, and (c) TSP toolpath with 4 mm fillet at sharp turns

3.2.5. Start and end point selection

In order to ensure quality and manufacturing process effectiveness, it is beneficial to fabricate parts using a continuous deposition of material without any interruptions or discontinuities in the process (Jin et al., 2014). Different printing pathways are available for the same component while printing, depending on the printing start point and the area-filling technique used by each layer. A TSP-based toolpath offers the same start and end point, as shown in *Figure 3.13*. The material deposition forms a complete loop by beginning at the point *'O'* and ending at the same point after filling the region inside the specified contour. For each layer, this pattern of material deposition may be repeated, guaranteeing a constant starting and stopping point for the production process. These start & end points can also be customized by the user.

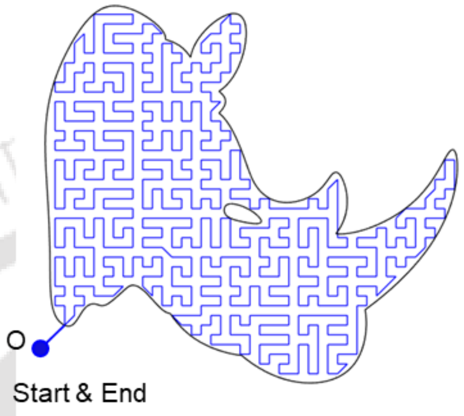

Figure 3.13 Material deposition starts and ends at a common point (O)

3.2.6. Compressive strength test and evaluation of anisotropy

Figure 3.14 illustrates the fabrication of concrete blocks measuring 160x160x160 mm^3 (length × width × height) using four distinct continuous toolpaths: contour parallel continuous, Fermat spiral, circular grid TSP, and rectangular grid TSP. Subsequently, directional markings were applied to the surface of each specimen. Following a curing period of 28 days, the specimens underwent compression testing utilizing a hydraulic-controlled compression testing machine (CTM) with a capacity of 2000 kN. Loading was applied at a rate of 1000 N/s until failure occurred. The printed blocks underwent testing in the X, Y, and Z directions for each of the four toolpaths to assess the anisotropic behavior of 3D printed structures.

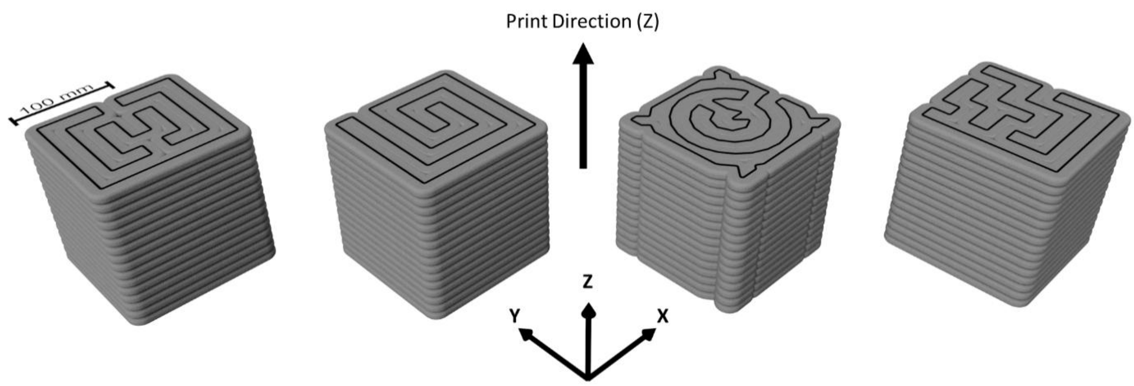

Figure 3.14 Illustrates 3D printed blocks using a continuous toolpath, from left to right, using contour parallel continuous, Fermat spiral, circular grid TSP, and rectangular grid TSP.

The determination of the anisotropic coefficient (I_{3D}) for the printed specimens was based on the empirical parameter established by Ye et al., (2021) (refer to *Eq. (3.6)*). Furthermore, the anisotropic coefficients in various directions (I_X, I_Y, and I_Z) can be calculated using *Eq. (3.7)* (Jin et al., 2014).

$$I_{3D} = (I_X + I_Y + I_Z)/3 \tag{3.6}$$

$$I_{Dir} = \sqrt{(f_X - f_{Dir})^2 + (f_Y - f_{Dir})^2 + (f_Z - f_{Dir})^2}/f_{Dir} \tag{3.7}$$

where '*Dir*' represents the loading directions and f_{Dir} represents the compressive strength corresponding to that direction.

3.3. Numerical studies

This section introduces multiple case studies to evaluate the resilience of the proposed methodology. A comparative analysis with existing algorithms (paintbrush, zigzag, contour parallel, and spiral) is also included to explore the merits and limitations of this approach. The algorithm is implemented using Python, Rhino, and Grasshopper platforms. We have created and meticulously tested two independent TSP toolpath methods in this study. The first strategy entails the creation of a rectangular grid-based toolpath, while the second strategy focuses on developing a circular grid-based toolpath. A comprehensive analysis of the numerical results is presented for the five distinct geometries (*Figure 3.15*), considering four key evaluation factors: continuity, printing time, time interval, and sharp turn.

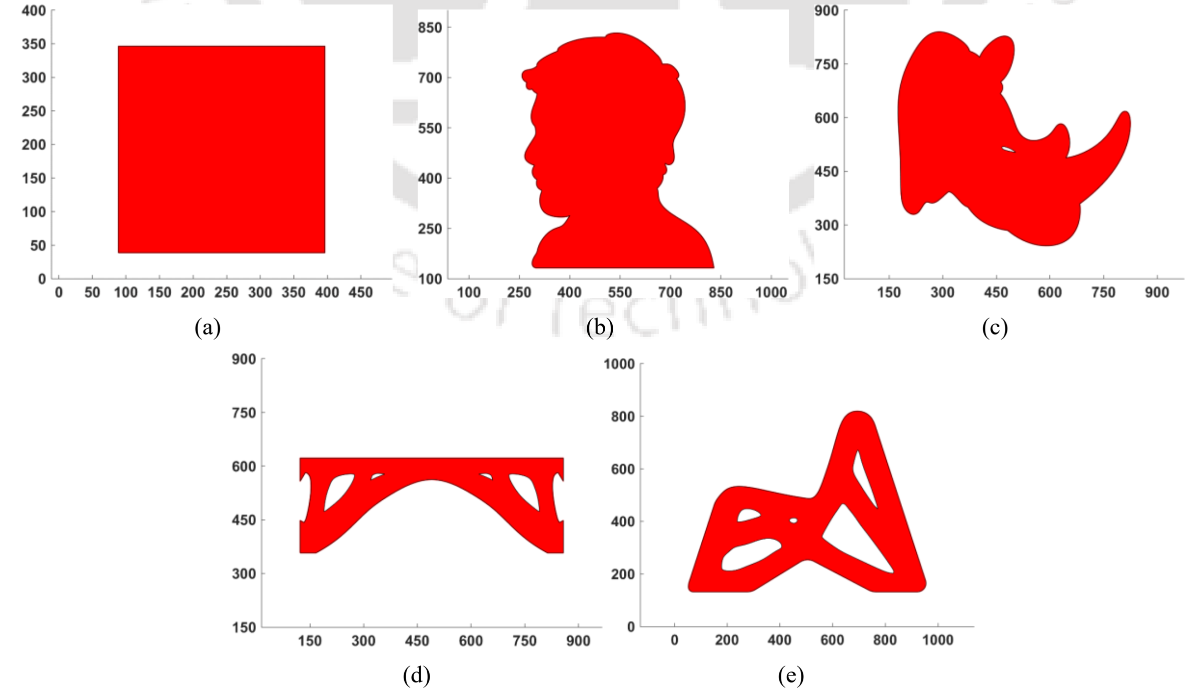

Figure 3.15 For evaluation of the performance of the TSP-based toolpath, five geometries were tested, including (a) Square, (b) Human face, (c) Rhino face, (d) Arch bridge, and (e) Chair.

3.3.1. Print quality

An approach mentioned in (Bi et al., 2022) is used to quantify print quality in terms of underfill and overlapping. Underfilled areas are generated by offsetting the toolpath by 0.5 times the bead width (0.5×w).

Total overlapping is determined as follows:

$$L \times w - A_T \tag{3.8}$$

Where L, w, and A_T are the total toolpath length, bead width, and the Target area that has to be deposited.

Table 3.1 shows underfilling and overlapping for the five geometries, and these results have been generated for the bead width equal to 22.5 mm.

Table 3.1 Underfilling and bead overlapping

	Toolpath			
	Rectangular grid without boundary trim	**Rectangular grid with boundary trim**	**Circular grid without boundary trim**	**Circular grid with boundary trim**
		Square		
Underfilling (%)	0.1824	0.0124	0.1189	0.0327
Overlapping (%)	0.0506	0.0948	0.0621	0.1045
		Human face		
Underfilling (%)	0.1104	0.0210	0.0869	0.0158
Overlapping (%)	0.0686	0.0754	0.0673	0.1135
		Rhino face		
Underfilling (%)	0.1338	0.0288	0.1169	0.0249
Overlapping (%)	0.0576	0.0826	0.0677	0.1146
		Arch bridge		
Underfilling (%)	0.3389	0.0762	0.2767	0.0511
Overlapping (%)	0.0058	0.0855	0.0659	0.1227
		Chair		
Underfilling (%)	0.1979	0.0412	0.1848	0.0321
Overlapping (%)	0.0352	0.0623	0.0404	0.0976

Table 3.1 indicates a significant reduction in underfilling percentages for various geometries with the adoption of boundary trim operations. Concurrently, there is a noticeable rise in the occurrence of beads overlapping, which can enhance the strength and stability of the final structure during the filling of the area. While underfilling is necessary for establishing complete

solidity in the printed structure, limiting it is very important, and implementing the boundary trim procedures on rectangular grids leads to a significant decrease in underfilling, ranging from 77.58% to 93.41%. In circular grids, the reduction in underfilling ranges from 72.50% to 82.62%. This decrement indicates a significant improvement in reducing empty spaces close to the edges, although it comes at the expense of more beads overlapping. *Figure 3.16* illustrates five testing geometry toolpaths (a) Square, (b) Human face, (c) Rhino face, (d) Arch bridge, and (e) Chair using the TSP toolpath for rectangular grid (left) and circular grid (right) with boundary trim.

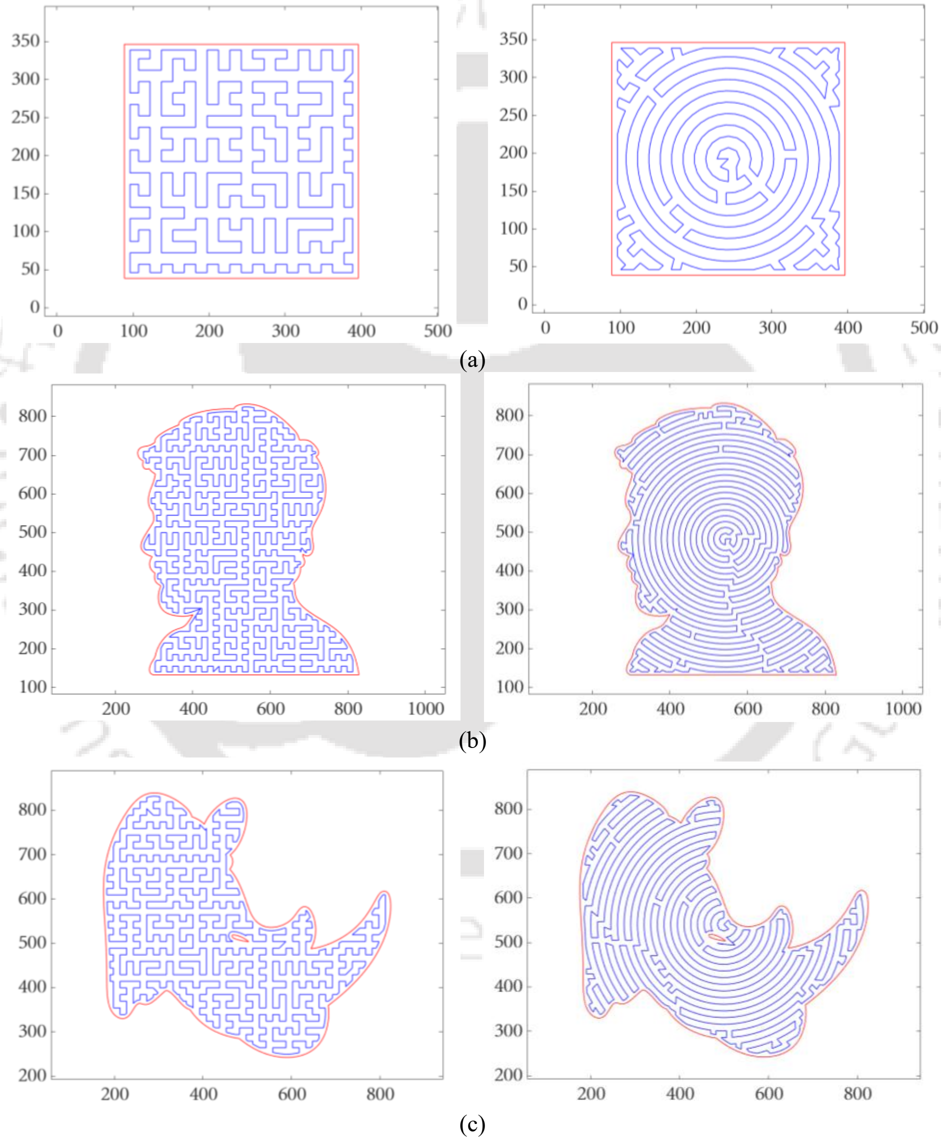

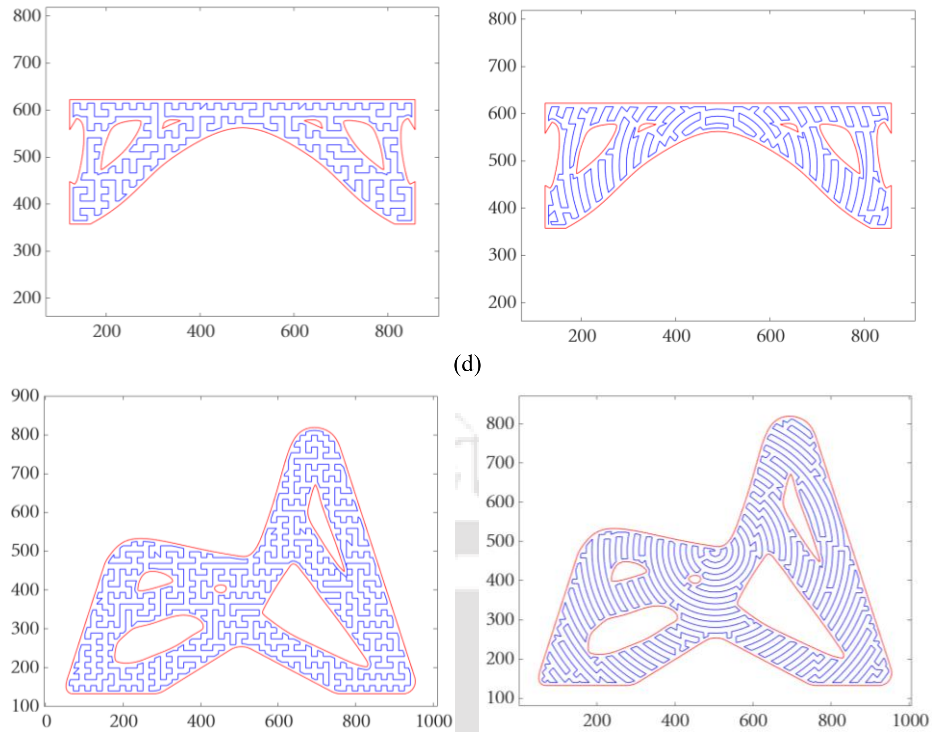

(d)

(e)

Figure 3.16 Testing geometries toolpath (a) Square, (b) Human face, (c) Rhino face, (d) Arch bridge, and (e) Chair using the TSP toolpath for circular grid (left), and rectangular grid (right) with boundary trim

In AMoC, the fabrication of large-scale geometry is the basic need. This analytical work focuses on the repercussions of scaling up by factors ranging from 100% to 600% at intervals of 100% while maintaining a consistent bead width. The analytic data for square geometry using rectangular and circular grid TSP toolpaths has been calculated for print quality.

Table 3.2 Effect of scaling on print quality while using TSP toolpath for square geometry

Square	**Toolpath**			
	Rectangular grid TSP toolpath with boundary trim		**Circular grid TSP toolpath with boundary trim**	
Scale factor	**Underfilling (%)**	**Overlapping (%)**	**Underfilling (%)**	**Overlapping (%)**
100%	0.0124	0.0948	0.0327	0.1045
200%	0.0119	0.0933	0.0319	0.0996
300%	0.0127	0.0962	0.0341	0.1018
400%	0.0115	0.0935	0.0320	0.1012
500%	0.0120	0.0971	0.0314	0.1030
600%	0.0122	0.0909	0.0342	0.1025

The findings indicate that upscaling does not significantly affect print quality, with only minor fluctuations observed in underfilling and overlapping percentages. In conclusion, the study highlights the feasibility of using the TSP toolpath for upscaling in large-scale AMoC processes. *Table 3.2* shows the effect of upscaling on print quality for square geometry using rectangular and circular grid TSP toolpaths, keeping a constant bead width of 22.5 mm.

3.3.2. Effect of step-over

In AMoC, the stepover distance directly affects path length and, consequently, the printing time. Material deposition per pass reduces when the stepover decreases, leading to additional passes and a smaller width in each pass. On the other hand, increasing the stepover results in wider breadth in each pass, thus allowing more material deposition per pass. This results in printing a part with fewer passes and printing time. Finding an ideal balance between material deposition efficiency and reducing the number of passes is challenging to achieve optimal stepover for printing time and material utilization. *Figure 3.17(a)* and *Figure 3.17(b)* show the effect of stepover on printing time for rectangular and circular grids, respectively, for all five geometries. The percentage change in printing time is influenced by adjusting the stepover values for rectangular grids, such that increasing the stepover from 15 mm to 20 mm leads to a decrease in printing time ranging from 25.88% to 24.39%. Similarly, when the stepover changes to 25 mm and 30 mm, the printing time decreases approximately 40.35% to 37.80% and 50.99% to 41.46%, respectively. Similarly, modifying the stepover values for circular grids leads to a reduction in printing time ranging from 25.47% to 24.04%, 39.75% to 36.56%, and 49.73% to 49.07% for stepover adjustments from 15 mm to 20 mm, 25 mm, and 30 mm, respectively.

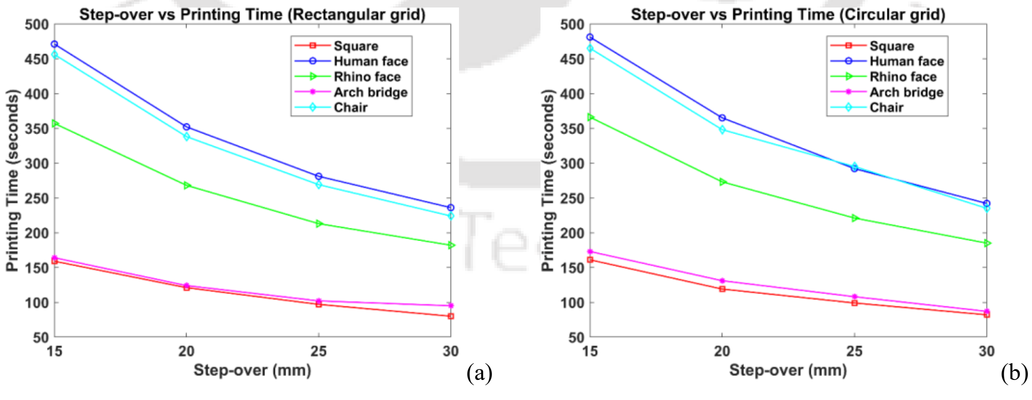

Figure 3.17 Step-over vs Printing Time, (a) Rectangular grid (b) Circular grid

3.3.3. Effect of the reduction factor

Figure 3.18 illustrates how toolpath length varies with a reduction factor for a 20 mm step-over distance. Four instances are provided for each geometry, for example, rectangular grid favoring horizontal direction (R.G.H.D.) in red color, rectangular grid favoring vertical direction

(R.G.V.D.) in blue color, circular grid favoring radial direction (C.G.R.D.) in green color, and circular grid azimuthal direction (C.G.A.D.) in magenta color. Irrespective of grid type, the toolpath length increases with the reduction factor. This phenomenon can be elucidated by considering an instance utilizing a simple rectangular grid with uniform dimensions, as depicted in *Figure 3.19(a)*. In this case, the toolpath remains consistent with a continual step-over. Specific areas inside this grid, indicated by red circles in *Figure 3.19(b)* (a decrease in the distance between two vertical lines), represent the less favored direction. A reduction factor (s = 0.90) reduces the grid width, emphasizing the horizontal direction. This reduction is illustrated in *Figure 3.18*; this causes an increase in the toolpath's length of approximately 0.30% to 26.47% for R.G.H.D., 1.18% to 15.35% for R.G.V.D., 2.08% to 7.98% for C.G.R.D., and 0.33% to 3.83% for C.G.A.D. It is thus clear that when the reduction factor decreases, it leads to an increase in toolpath length and, consequently, printing time.

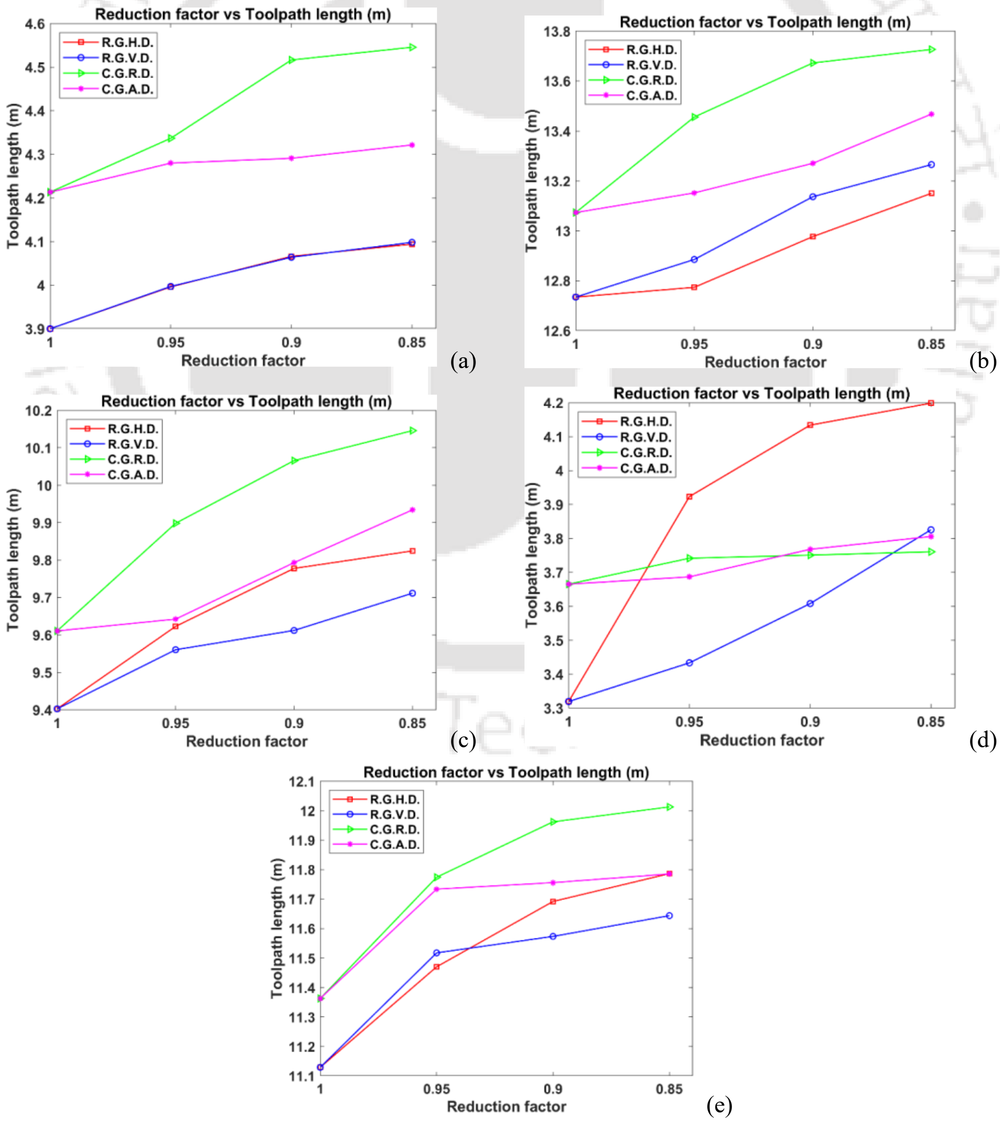

Figure 3.18 Variation in toolpath length for (a) Square, (b) Human face, (c) Rhino face, (d) Arch bridge, and (e) Chair with different grid reduction factors.

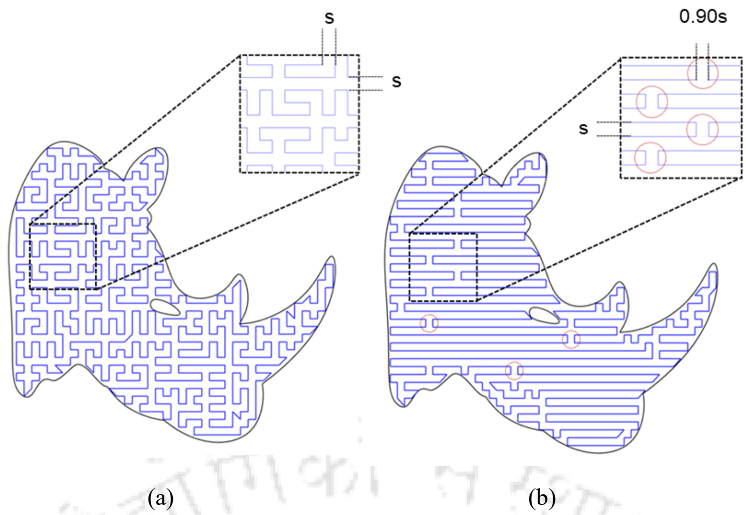

Figure 3.19(a) Toolpath maintains a constant stepover, and (b) Gap between two vertical lines of the toolpath is reduced due to grid irregularities.

3.3.4. Continuity

In addition to generating a continuous toolpath, the TSP solver maintains a consistent speed and rate of material deposition in AMoC during the area-filling operation. Table A2.2 (see Appendix Section A2.2) shows the number of lifts (discontinuities) present in different toolpath strategies for 15 mm Step-over. In contrast, in the case of the TSP toolpath, only one single discontinuity (nozzle lift) is present, i.e., during layer changes.

3.3.5. Printing time and time interval

The TSP toolpath offers an excellent choice for delivering both speed and performance in AMoC by minimizing printing time without sacrificing the part quality. *Table 3.3* shows the printing time comparison of the TSP toolpath with different toolpath strategies for a printing speed of 40 mm/sec and 15 mm stepover (calculating for a 15 mm nozzle). The TSP toolpath exhibits greater efficiency and time optimization than the other toolpaths examined in the investigation. According to the data in *Table 3.3*, it can be inferred that the printing time for the available toolpath strategies is more significant when compared to the 'TSP toolpath' with the lowest printing time. The increase in printing time was found for the paintbrush strategy, ranging from 13.57% to 84.15%, -1.16% to 38.12% for the raster strategy (negative values are due to simple geometry and fewer turns), 14.05% to 60.37% for contour parallel strategy, and 65.50% to 264.67% for spiral toolpath strategy concerning square (simplest) and chair (complex shape) respectively.

Table 3.3 Comparison of printing time for different toolpath strategies

Factor	**Printing time (Sec)**					
	TSP toolpath		**Other available AM strategies**			
Toolpath	**s = s (Rectangular grid with boundary trim)**	**α = β (Circular grid with boundary trim)**	**Paintbrush**	**Zigzag**	**Contour Parallel**	**Spiral**
Square	155.148	155.05	176.25	**153.35**	182.802	256.77
Human face	474.552	**444.342**	544.602	477.102	506.398	773.85
Rhino face	**324.39**	329.88	514.05	407.052	444.648	632.118
Arch bridge	184.458	**173.412**	301.02	239.748	257.748	632.352
Chair	**393.408**	401.802	725.118	535.122	630.27	1196.472

The mechanical performance of 3D-printed concrete is affected by the start & end points of the toolpath, which must be carefully decided before the print begins. The interfacial bond strength of the 3D-printed concrete declines as the printing time interval rises, according to test data produced by Le et al., (2012). Feng et al., (2015) and Nerella & Mechtcherine, (2019). Due to the same start and end point in the TSP path planning, uniform interfacial bond performance can be envisaged in AMoC by maintaining the same printing time interval.

3.4. Experimental validation

The gantry printer and 3D mortar mix were selected for this study are presented in section 2.2.

3.4.1. Print quality

The samples are 3D printed using the gantry-based concrete 3D printer. The experimental results shown in *Figure 3.20* unambiguously validate the toolpath's ability to fill the square area. Eight specimens for Square (three adhering to rectangular grid and five w.r.t circular grid) are fabricated for initial investigation of the TSP toolpath, excluding boundary trimming. The samples are printed using a 15 mm step-over TSP toolpath. *Figure 3.20(a)*, *Figure 3.20(b)*, and *Figure 3.20(c)* show the part printed using the TSP toolpath with a rectangular grid, while *Figure 3.20(d), Figure 3.20(e), Figure 3.20(f), Figure 3.20(g), and Figure 3.20(h), show* the part printed using TSP toolpath with circular grid. The data in *Table 3.4* shows the underfilling and overlapping for the bead width of 22.5 mm.

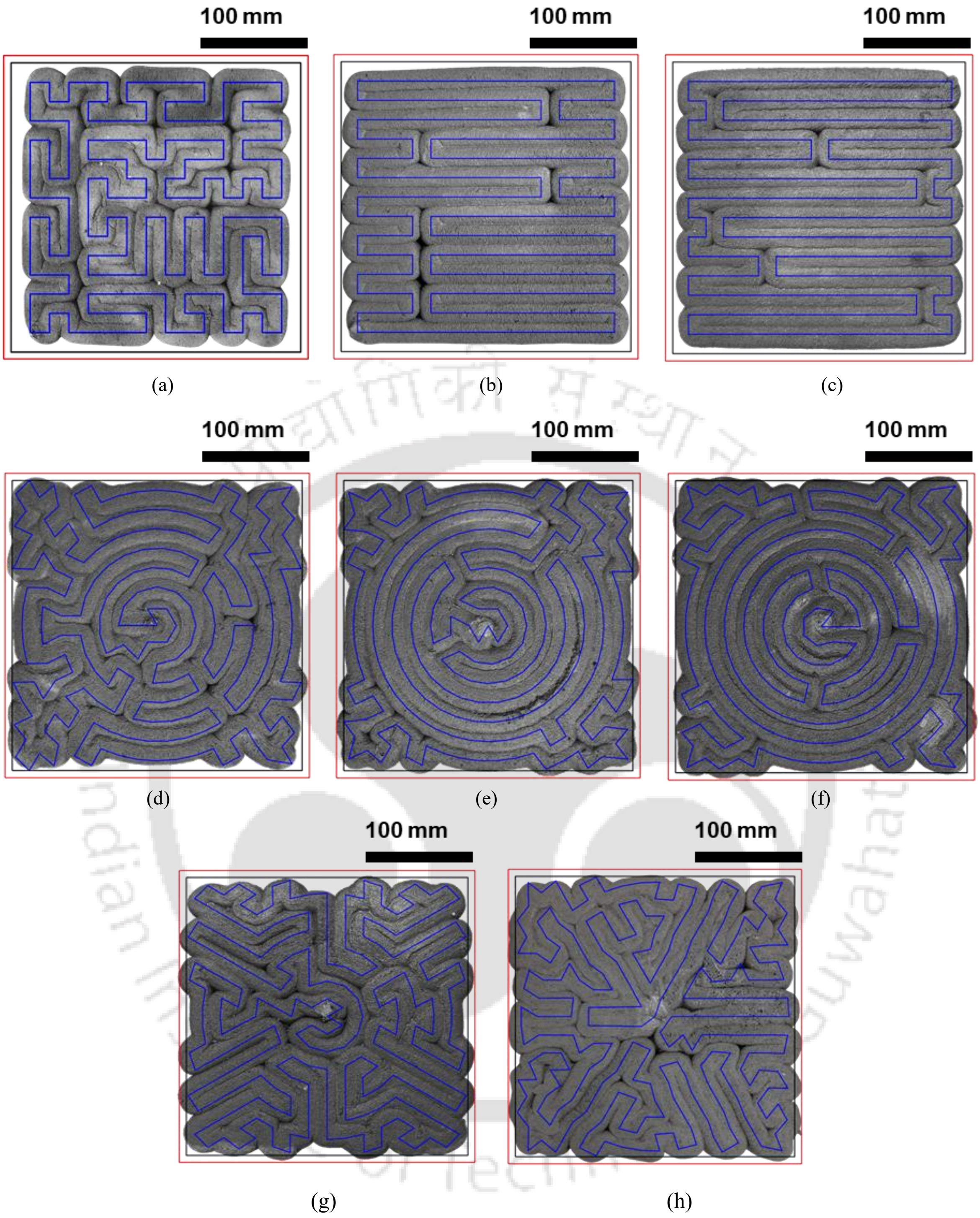

Figure 3.20 Parts printed using TSP toolpath with the following configuration; (a) s = s, (b) s = 0.95s, (c) s = 0.90s, (d) α = β, (e) α = 0.95β, (f) α = 0.90β, (g) 0.95α = β, and (h) 0.90α = β

Table 3.4 Underfilling and overlapping for Square

Toolpath	*s = s*	*s = 0.95s*	*s = 0.90s*	*α = β*	*α = 0.95β*	*α = 0.90β*	*0.95α = β*	*0.90α = β*
Underfilling (%)	0.2089	*0.1850*	*0.1783*	*0.1073*	*0.0728*	*0.0848*	*0.1260*	*0.1136*
Overlapping (%)	0.0506	0.0723	0.0786	0.0673	0.0745	0.0815	0.0738	0.0860

Two "Rhino face" samples are 3D printed with a TSP toolpath with border trimming for a thorough analysis. The toolpaths used to fabricate the Rhino face are a non-unique direction rectangular grid (s = s) and a non-unique direction circular grid (α = β). *Figure 3.21(a) and Figure 3.21(b)* show printed geometry with rectangular and circular grid TSP toolpaths using a 15 mm nozzle and 22.5 mm bead width for proper overlapping of the consecutive beads. Visual observation indicates that the TSP-generated path may not effectively retain the boundaries of smaller areas, as evidenced by the unclear representation of the eye in the rhino's face geometry after 3D printing.

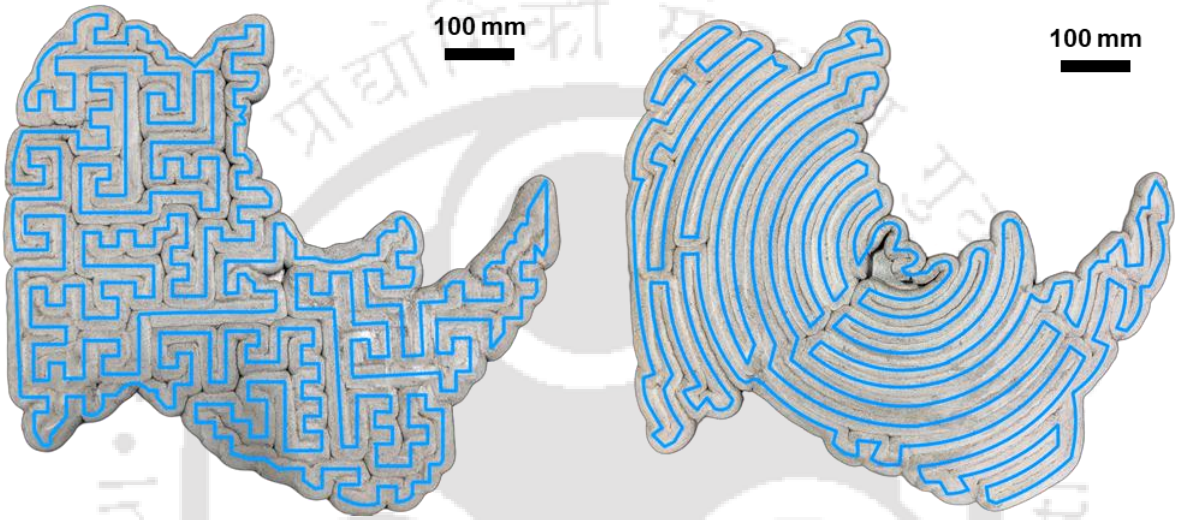

(a) (b)

Figure 3.21 Rhino face printed using 15 mm nozzle (22.5 mm bead width) (a) Rectangular grid, and (b) Circular grid

3.4.2. TSP toolpath for topology-optimized design

An optimal design ensures waste minimization while maintaining satisfactory structural integrity. In this study, the Arch bridge and Chair are the two optimal geometries, and only the Arch bridge, having dimensions 750 × 280 × 250,, is 3D printed with 100% infill setting using the selected concrete mix. *Figure 3.22(a) and Figure 3.22(b) show an Arch bridge constructed using a* continuous TSP toolpath with both rectangular and circular grid orientation. These examples confirm that the proposed TSP-based continuous toolpath can facilitate the fabrication of spatially complex topology-optimized structures.

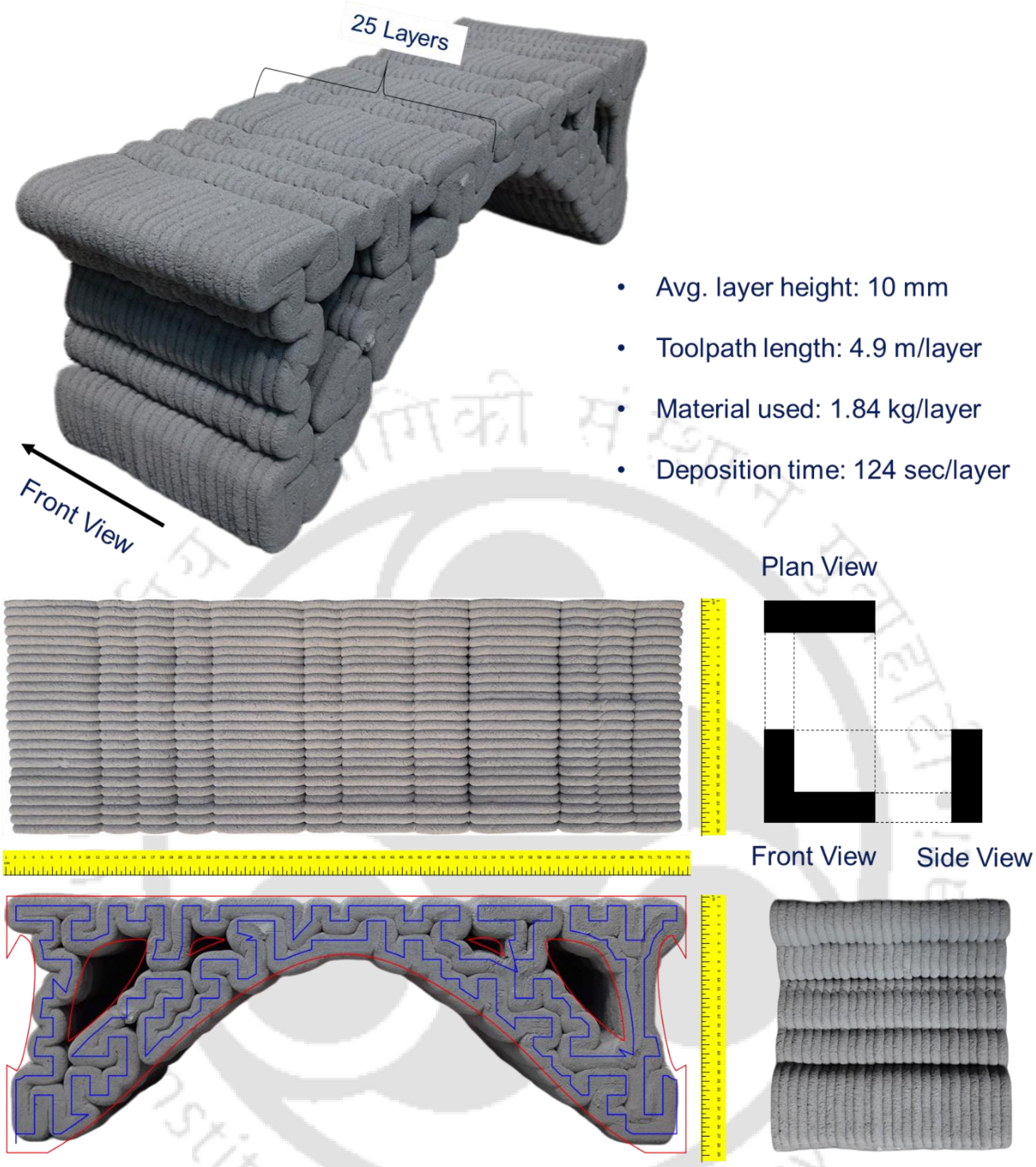
25 Layers
Front View
Avg. layer height: 10 mm
Toolpath length: 4.9 m/layer
Material used: 1.84 kg/layer
Deposition time: 124 sec/layer
Plan View
Front View
Side View

(a)

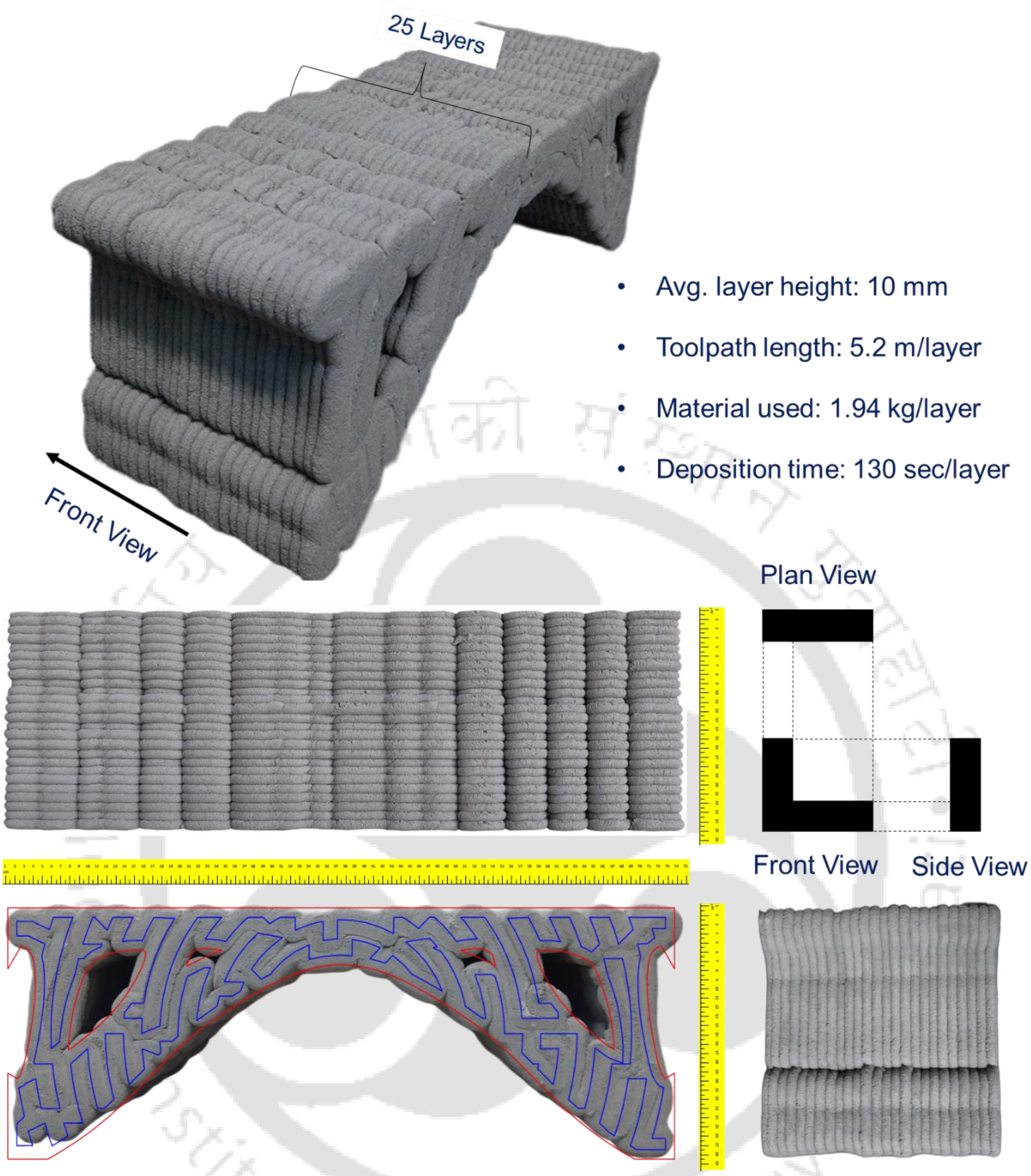

(b)

Figure 3.22 3D printed Arch bridge produced using (a) Rectangular grid TSP toolpath with boundary trim, and (b) Circular grid TSP toolpath with boundary trim

3.4.3. Sharp turns

The impact of sharp turns within the TSP toolpath has been effectively demonstrated by examining printed parts. In *Figure 3.23*, the area-filling characteristics of Square are showcased utilizing a rectangular grid-type TSP toolpath. *Figure 3.23(a)* displays a square printed with the TSP toolpath featuring sharp corners. In contrast, *Figure 3.23(b)* exhibits the same geometry with a 2 mm fillet at every sharp corner, and *Figure 3.23(c)* illustrates the printing of a square with a 3 mm fillet. Upon visual inspection, it is clear that, under no fillet condition, the printed geometry reflects the printer's momentary start and stop at each sharp corner, resulting in nozzle clogging and an uneven bead width along the toolpath. This phenomenon persists even with a 1 mm fillet. Conversely, employing a 2 mm fillet at each sharp turn yields the most effective area-filling with minimal underfilling area. As the fillet radius increases, the underfilling area progressively expands, as shown in *Figure 3.23(c)*, an example with a 3 mm fillet radius. Notably, a further increase in the fillet value consistently results in an augmentation of the underfilling area. All experiments kept the print speed at 60 mm/sec with a constant material flow rate.

(a) (b) (c)

Figure 3.23 Square shape printed using TSP toolpath with (a) Sharp turns, (b) 2 mm fillet, and (c) 3 mm fillet at every sharp turn.

3.4.4. Directional compressive strength

The compressive strength of 3D printed products depends on layer orientation for a given process-material combination. *Figure 3.24(c)* shows that concrete cubes are designed and printed by four continuous toolpaths, including TSP, to compare their effect on ultimate load-bearing capacities. The details of the material and printing process are provided in section 2.2. All the test results are the medians of three replication experiments. Section 3.2.6 summarizes the compression testing procedure and evaluation of anisotropic dependency concerning three loading directions. *Figure 3.24(a)* shows that the Z direction compressive strength of all four toolpaths (Contour parallel continuous, Fermat spiral, and TSPs) is almost equal because of the nearly equal length of the continuous path deposited on every layer. As depicted in *Figure 3.24(c)*, the voids between the filaments create weak vertical planes and the potential formation of cracks under the X and Y loading directions. Such weak planes will result in weaker compressive behavior in X and Y directions, thus creating an anisotropic behavior of 3D printed concrete *(Figure 3.24(b))*. Both the circular and rectangular TSP toolpaths have resulted in approximately 41.67% & 34.87%, and 35.35 & 27.73% reduction in anisotropic dependency concerning the contour parallel continuous, and Fermat spiral paths, respectively. Anisotropic mechanical properties (Murcia et al., 2020) are often reported in additively manufactured parts. The size and exact effect of voids originating from toolpaths and other influential parameters could be pursued as a separate research topic in the future.

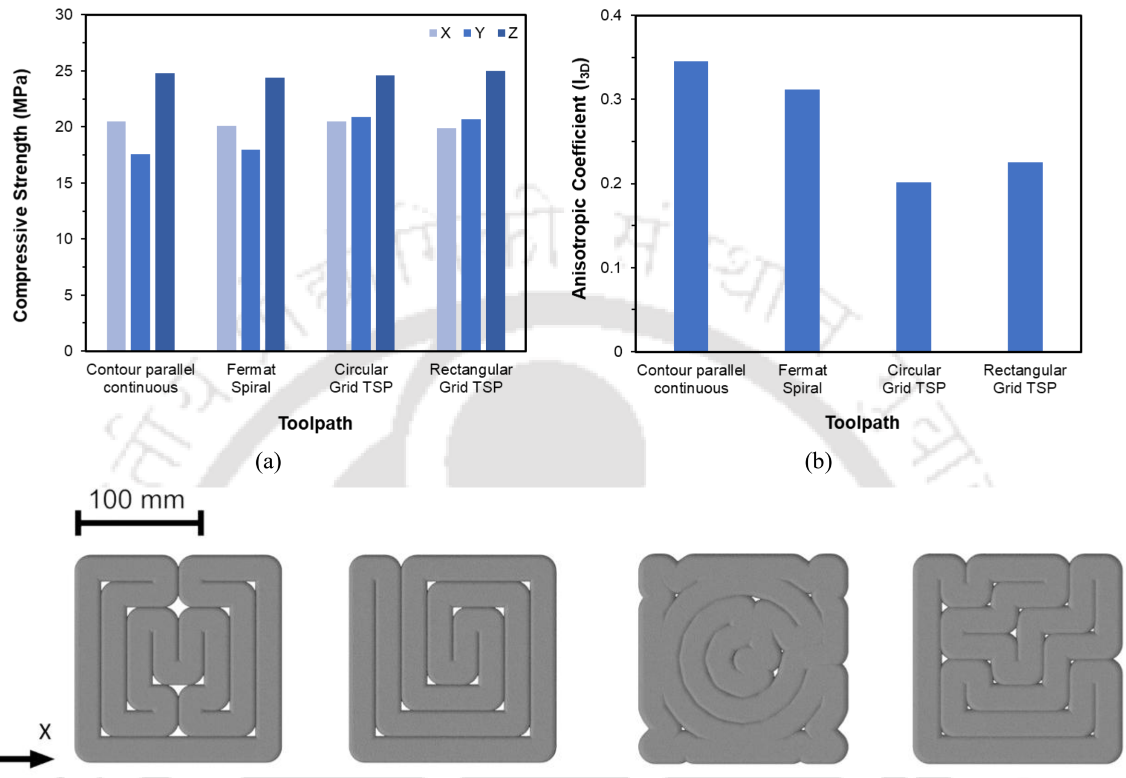

Figure 3.24 The effect of continuous toolpaths on (a) 28-day compressive strength, (b) Anisotropic coefficient, and (c) Voids at the inter-filament vertical planes

3.5. Summary

The proposed TSP-based continuous toolpath generation workflow provides better print quality (underfilling <0.05 and overlapping <0.11), fewer sharp turns, and reduced anisotropic strength, thereby enabling AMoC technology to embrace both productivity and quality in handling different planar geometries. The results demonstrate that the TSP-based toolpath minimizes the print head travel distance and substantially reduces the total printing time. Moreover, integration of a continuous toolpath strategy and (solid) topologically optimized design shows great potential for minimizing the concrete usage, which can lead to cost reduction and enhanced design flexibility. The experimental and numerical results obtained from various geometries confirmed the scalability and robustness of the workflow that can generate continuous toolpaths for target shapes.

The proposed TSP-based workflow enables continuous, space-filling concrete deposition with reduced travel distance, lower printing time, and improved structural continuity, demonstrating a scalable and material-efficient path-planning solution for AMoC. Despite computational growth with problem size, the method remains practical for large-scale concrete printing and provides a strong foundation for future extensions toward robotic non-planar deposition and reinforced concrete printing.

Chapter 4: Development of a Growth Curve-based Toolpath Strategy for Area Filling

This chapter proposes a growth curve-based continuous toolpath generation method for area filling. The strategy provides a computationally efficient and scalable solution while overcoming the limitations of the TSP-based method, such as exponential computation time and complexity in large-scale applications. The framework is validated across a range of geometries, highlighting robustness and adaptability.

A portion of this chapter has been published:

Sahu, A., & Panda, B. (2026). Growth curve-based continuous toolpath for improving the performance of the additively manufactured concrete. *Progress in Additive Manufacturing* *https://doi.org/10.1007/s40964-025-01515-5*

4.1. Abstract

In this chapter, a Growth curve-based toolpath planning was developed to generate area-filling and continuous toolpath for extrusion-based AMoC. Unlike conventional methods that rely on FDM-based material deposition, the growth curve-based toolpath utilizes a generative system to create a continuous toolpath that optimally fills the given space, considering AMoC process constraints. The process begins with an input curve subjected to a linear growth function and a user-defined growth factor. The effects of growth factors and other design parameters, including tuning step-over and scale factors, on various performance measures — such as printing time, toolpath continuity, computation time, anisotropic mechanical properties, and print quality — were investigated. Based on experimental and numerical trials, it was confirmed that the proposed method enables efficient and variable area filling with minimal nozzle lifts and sharp turns for the AMoC process. Furthermore, it outperforms the extant zigzag, contour-parallel, and continuous TSP-based toolpath methods, while demonstrating a practical pathway toward optimized part printing for infrastructure and architectural applications.

4.2. Methodology

The problem statement for the Growth curve-based area filling is as follows:

Let's consider a target area (A_T) in a two-dimensional space defined by its boundary. The issue pertains to the expansion of an input curve defined by the user during the initial phase inside the target area. A user-defined growth function ($R(t)$) determines the expansion of this input curve by the growth factor (G). Here, the term $'t'$ denotes the required iterations. The growth factor sets the pace at which the curve grows over iterations.

The objective of the GCAF problem is to design a growth strategy that fulfills the following criteria:

- **Constant Distance Maintenance:** As the input curve grows with iteration or time based on the provided growth function, the growing curve continually maintains a minimum fixed distance (s) from itself. This ensures that the completely grown curve uniformly occupies the target area (A_T) without any areas of overlap.
- **Non-Crossing Constraint:** The growing curve follows a single, continuous path without a single crossover to itself, akin to a Hamiltonian circuit.

- **Area Coverage:** Following the given limitations, the growing curve should effectively grow inside the target area only.

The final full-grown curve, which must adhere to the growth function, distance limitation, and non-crossing constraint, can be defined as a Hamiltonian Circuit. Another significant characteristic of a Hamiltonian Circuit (or path) is its closed-loop structure, meaning it has a shared vertex for both the starting and ending points. *Figure 4.1* illustrates the complete algorithm. This algorithm demands four user inputs, shown in the light grey box: (i) importing the CAD file, (ii) specifying the step-over $'s'$, (iii) defining the Input Curve, and (iv) defining the growth function with a growth factor. The algorithm breaks down into three key steps, represented by (a) orange, (b) turquoise, and (c) green.

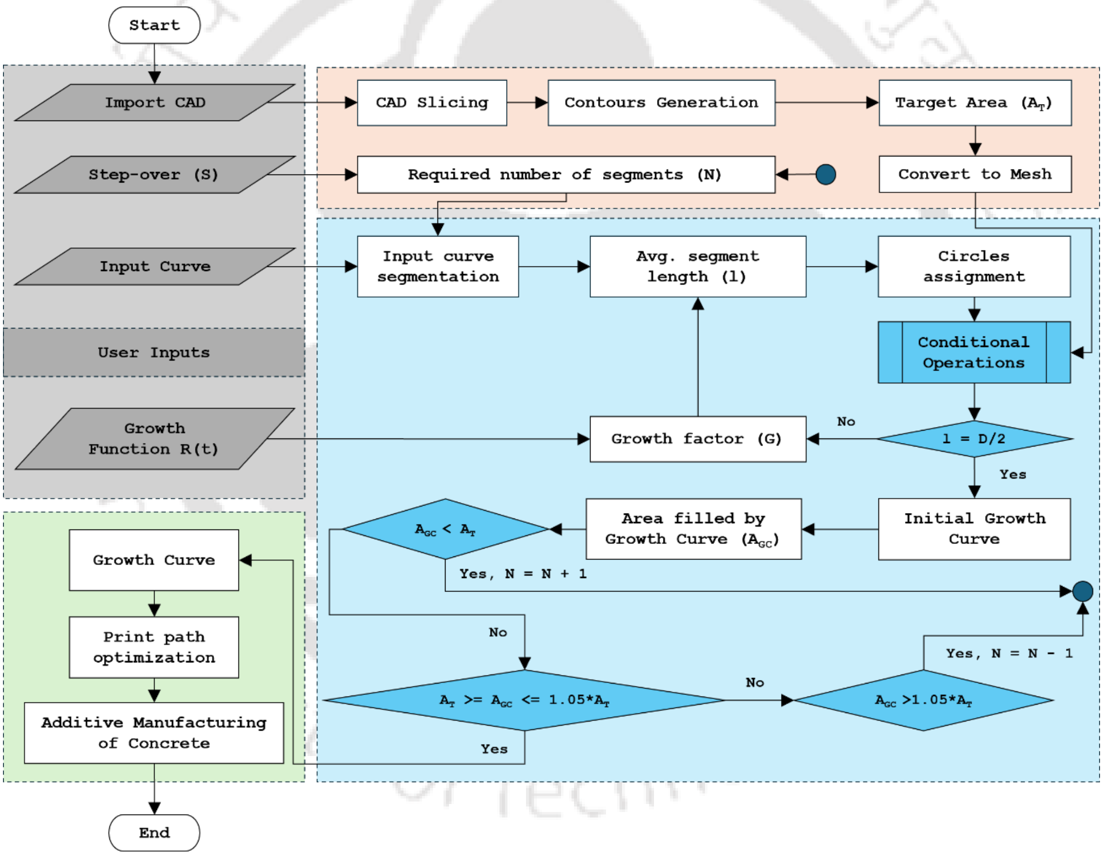

Figure 4.1 Growth curve-based area-filling algorithm for toolpath generation.

Referring to *Figure 4.1*, the algorithm is structured into three key steps:

Step (a) involves two operations: contour generation and area definition. It utilizes two user inputs: importing the CAD file and specifying the step-over (s).

Step (b) utilizes the other two user inputs, which define the input curve describing the growth function $(R(t))$ with a growth factor (G) and the conditional operations (shown in a darker shade of turquoise). The fully grown growth curve is obtained by the end of the second step.

Step (c) comprises toolpath optimization, G-code generation, and product fabrication.

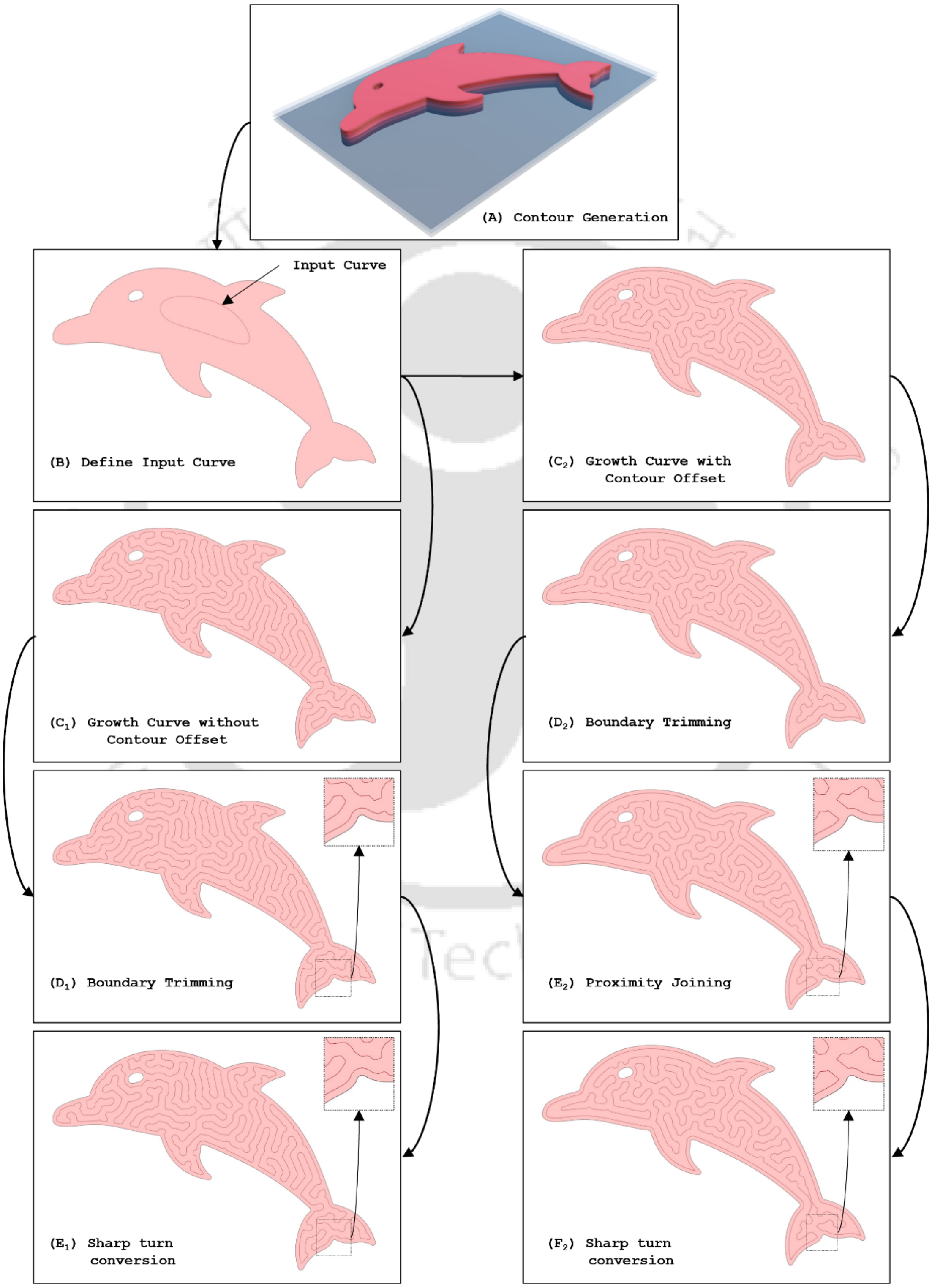

Figure 4.2 The process sequence for growth curve-based toolpath generation

A graphical layout of the algorithm is illustrated in *Figure 4.2*. The process begins with *Figure 4.2* contour generation of the required geometry, which is then followed by *Figure 4.2* defining the input curve that expands within the target area according to a growth function. Following this, the process can proceed in one of two ways: the first, without contour offset *Figure 4.2*, and the second, with contour offset *Figure 4.2*. The geometry's shape and other relevant factors determine whether or not to incorporate a contour offset. A contour offset produces a smoother outer surface in the printed part but may cause excessive material deposition (overfilling) in narrow areas. On the other hand, excluding the outside contour avoids overfilling. It is more suitable for thin structures but may not produce a smoother outer surface in the printed part. Process *Figure 4.2* demonstrates the fully grown growth curve within the target area, *Figure 4.2* shows the operation of trimming the boundary between the contours of the target area and the fully grown growth curve, *Figure 4.2* entails joining the boundary-trimmed growth curve with the outer contour based on proximity, and *Figure 4.2* handles converting sharp turns in the path into smoother transitions. The algorithm for this study was created using Grasshopper, Rhinoceros 7.0's visual programming environment. The machine used for development and analysis featured an Intel i7 processor, 32 GB of RAM, and a 6 GB graphics card.

4.2.1. Contour generation and area definition

The initial stage of the growth curve-based area-filling (GCAF) algorithm entails the generation of contours derived from the 3D model to be printed. This starts with **importing the CAD file,** which encompasses the geometric data, and dividing it into layers to extract the 2D cross-sectional boundaries of the geometry within each layer. Once the boundaries have been identified, the method determines the actual area (A) of the geometry within each layer. The **step-over** ($\boldsymbol{s}$) is then defined as a critical parameter, signifying the width of material deposition. The algorithm uses the given step-over to compute the target area, and the AMoC process will fill the material by following the toolpath created by the growth curve. To accomplish this, the algorithm calculates the necessary number of segments (N) *(Eq. (4.1))*, each with a length equal to $'s/2'$, required to fill the target area. Subsequently, the target area is transformed into a mesh, which will be helpful in the remaining steps of the procedure. The algorithm optimizes the printing process for accuracy and efficiency by adjusting the number of segments (N) to match the actual area (A) closely.

$$N = \frac{\left(A_T/_s\right)}{\left(^s/_2\right)} \tag{4.1}$$

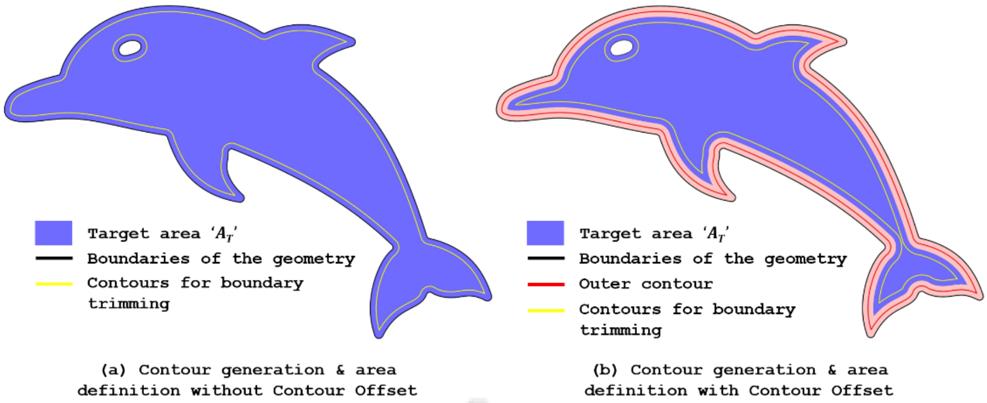

Figure 4.3 Contour generation & area definition (a) Without contour offset, and (b) With contour offset

Figure 4.3 illustrates the process for generating contours and defining the area for two different scenarios: one without contour offset (*Figure 4.3(a)*) and another with the contour offset (*Figure 4.3(b)*). The geometry's actual area (A), is calculated based on its boundaries (shown in black). In the first scenario, the target area is the same as the actual area. In the second case, the target area is determined by offsetting the outer boundary of the geometry inward by a factor of $'1.00 \times s'$ (The target area is highlighted in light blue). The second scenario occurs when a printed item demands an outside contour. Generating the contours for boundary trimming operations requires offsetting the target area's boundaries by a factor of $'0.5 \times s'$ with the direction of the offset towards the target area in both scenarios (shown in yellow).

4.2.2. Defining an input curve

In the second stage, the task is to **define an input curve**, either specified by the user or an offset curve derived from the geometry (maybe a contour generated for boundary trim). The input curve must encompass the target area mesh and can have any shape, but it must not have any self-intersections. Furthermore, the curve must be closed. After being defined, the input curve will be divided into 'N' segments, each of equal length $'l'$. At each intersection point of these segments, a circle has been assigned, with a radius equal to the length of the segment $'l'$. Every segment of the input curve grows by a growth function. The length of each segment is determined according to the total length of the input curve. If the input curve is longer, each segment will also be longer, meaning fewer iterations will be needed for the input curve to grow entirely, and vice versa, as long as specific conditions are satisfied.

Figure 4.4 illustrates two different methods for defining the input curve (shown in dark red). In *Figure 4.4(a)*, the user explicitly defines a closed-loop input curve. In *Figure 4.4(b)*, the closed-loop input curve is an offset curve derived from geometry. The input curves are subsequently partitioned into $'N'$ Segments according to the target area.

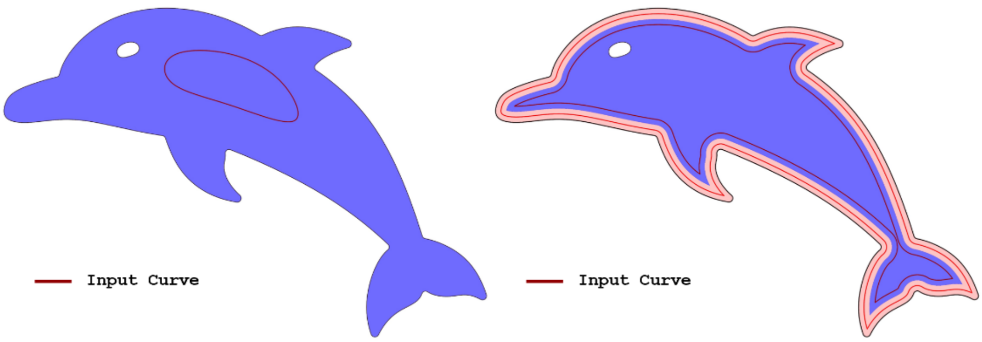

(a) User-defined Input Curve inside the target area

(b) Offset curve derived from the geometry used as an Input Curve

Figure 4.4 Defining the Input Curve (a) User-defined, and (b) Offset curve derived from the geometry

Figure 4.5 illustrates the assignment of a circle with a radius equal to $'l'$ at every intersection point between two adjacent segments. *Figure 4.5(a)* shows that a smaller input curve corresponds to shorter segment lengths, whereas *Figure 4.5(b)* demonstrates the opposite. The length of these segments will increase with each iteration until it reaches half the value of step-over, which eventually equals the radius of each circle in each iteration. Each segment and circle undergoes specific conditional operations to ensure that the input curve grows into a continuous, non-intersecting path spaced apart by a minimum distance $'s'$.

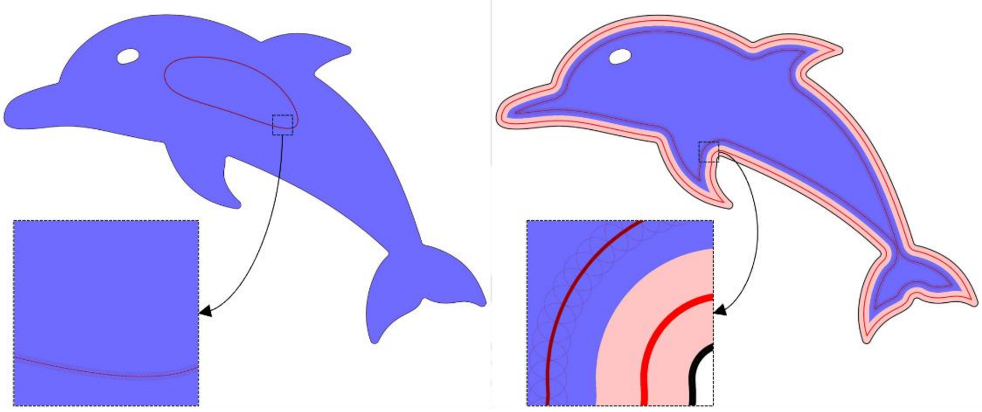

(a) A circle with radius 'l' is assigned at every intersection point between two adjacent segments

(b) Circle with radius 'l' is assigned at every intersection point between two adjacent segments

Figure 4.5 Assignment of the circle at every intersection between two adjacent segments of (a) User-defined input curve, and (b) An offset input curve

4.2.3. Defining a growth function R(t)

In the third step, the user-defined Growth function $'R(t)'$ is assigned to the input curve. The growth function has a growth factor 'G', which continuously increases the value of the initial segment length $'l'$, with each iteration. This process continues until the length of the segment reaches a final value equal to $'s/2'$. The growth factor 'G', defines the rate at which the segment length increases in size, leading it from its original length 'l' to the desired length '$s/2$' through a series of iterations 't'. This ensures a controlled and continuous segment growth defined by the particular growth function. This growth of the segments ensures that all the segments collectively occupy the target area, with precision. The growth can be modeled by several mathematical functions, such as linear, quadratic, or others. The specific function chosen will impact on the number of iterations and computation time required to fill the entire region. The number of iterations 't' can be found with the help of a growth factor, initial length, and the target length '$s/2$', of each segment. *Eq. (4.2)* shows a linear growth function.

- **Linear Growth Function:** The length of a segment rises uniformly with each iteration.

$$R(t) = l + G \times t \tag{4.2}$$

The number of required iterations (t) based on a growth factor (G):

$$t = \frac{\frac{s}{2} - l}{G} \tag{4.3}$$

4.2.4. Conditional operations

The fourth step involves conditional operations for the segments of the input curve, regulating the growth curve in the given area. The input curve undergoes four conditional operations in an ordered sequence after it is divided into $'N'$ segments of the same length $'l'$.

The first conditional operation, ***Equal Length***, ensures the length of each segment remains the same throughout the number of iterations 't'. *Figure 4.6* shows the effect of the linear growth function on the length of each segment of the input curve. If the average segment length is not equal for all the segments, then the algorithm will redo this operation as shown in *Figure 4.8*. The input curve has a cumulative length of 1639.41 mm. By using $Eq. 4.1$, the number of segments' N' was determined to be 618. Hence, if the input curve is divided into 618 segments, each segment will have an average starting length $'l'$ of 2.653 mm, at $'t = 0'$. For a growth factor of 0.5, after each iteration, the length of each segment grows by 0.5 mm and the required number of iterations $'t'$, comes out to 8.69 (nearly 9) using $Eq. 4.3$. Following the 1st iteration, the segment length grows by 0.5 mm, leading to a revised length of 3.153 mm. The length of the segment increases gradually by 0.5 mm in each iteration until it reaches the maximum length of 7 mm in the 9th iteration (in this specific scenario). *Figure 4.6(a) – Figure 4.6(f)* shows the gradual increase in segments' lengths during iterations with odd numbers, starting from 0, 1, 3, 5, 7, and 9.

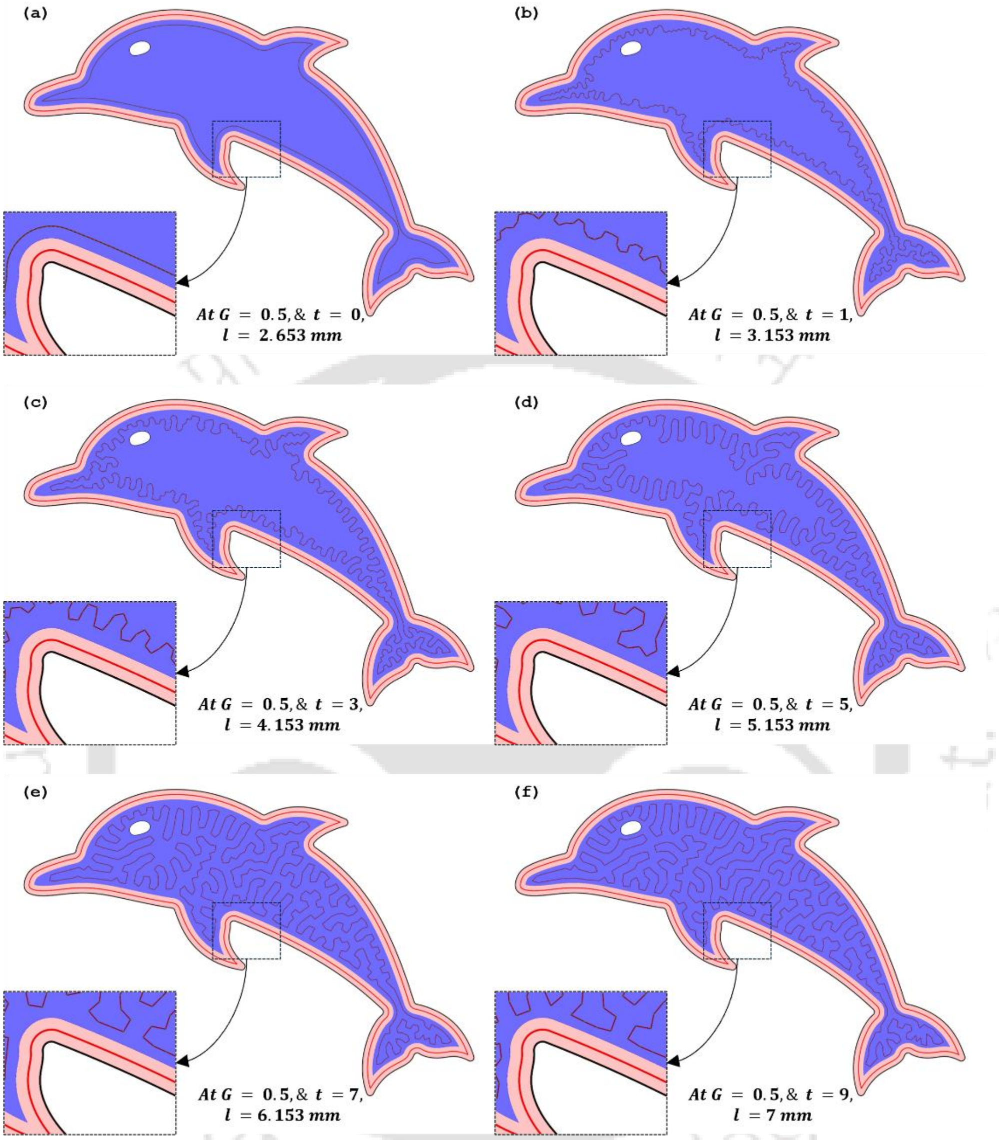

Figure 4.6 Growth of each segment while subjected to equal length operation and linear growth function with a growth factor of 0.5, where 't' varies in an order (a)0→(b)1→(c)3→(d)5→(e)7→(f)9

The second conditional operation, ***Circle Collide***, ensures the circles assigned at every intersection point between two adjacent segments do not intersect and overlap with one another. This operation ensures a minimum distance between adjacent paths, precisely twice the length of the segment $'2 \times l'$ at any iteration. This spacing ensures the path does not intersect itself, creating a Hamiltonian circuit. The path also traverses through all the centers of the circles within the target area without any significant overlapping. *Circle Collide* is a physics-based solver used in circle packing algorithms and spatial distribution tasks, ensuring that elements spread out evenly on a plane or surface without intersecting one another. Implemented through the Kangaroo plugin in Grasshopper, this solver applies repulsive forces between overlapping or closely spaced circles, driving them apart until collisions are resolved. The operation runs iteratively for each iteration (t) as the circle radii increase, and convergence is achieved when the repulsive forces balance out and the system reaches an equilibrium state as shown in *Figure 4.8*.

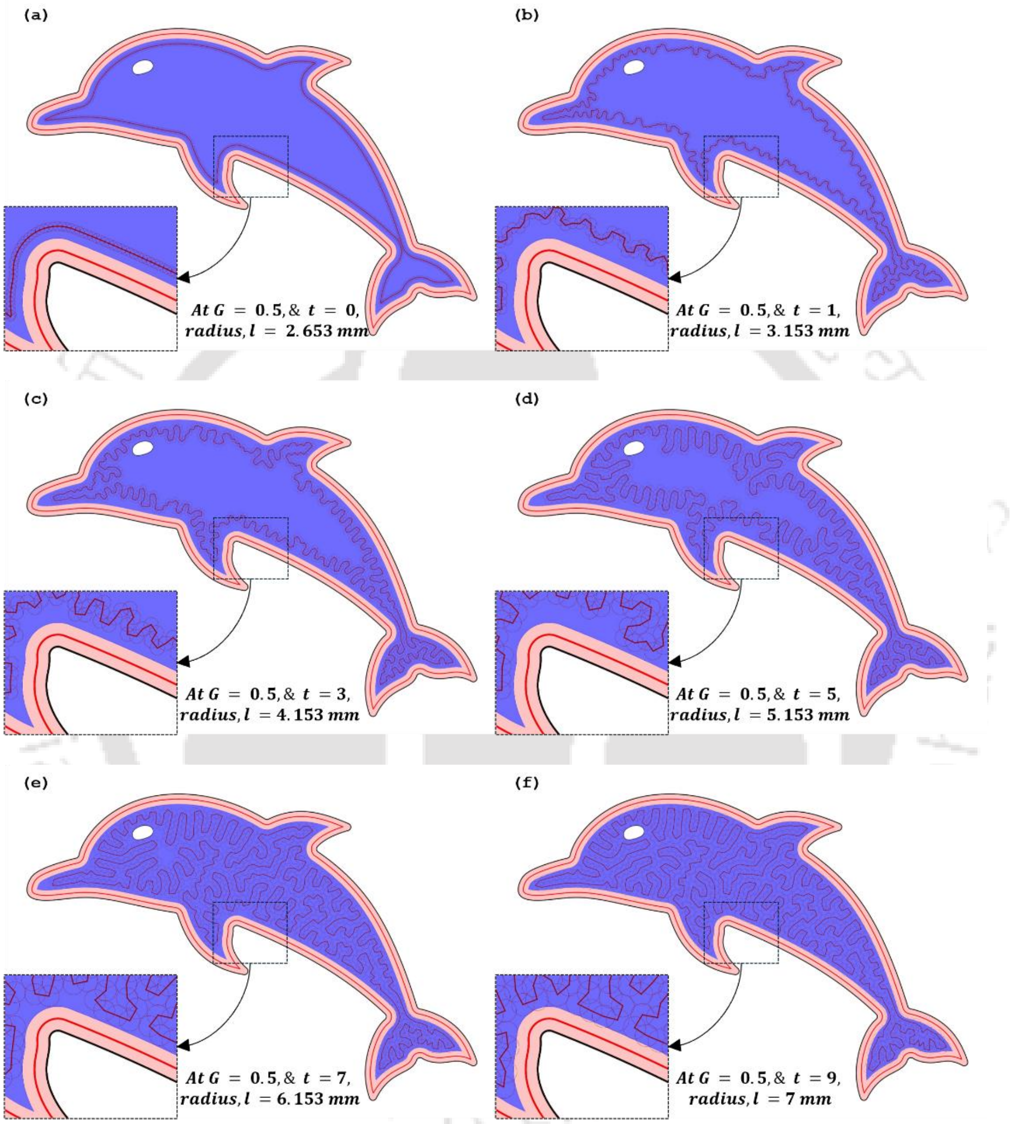

Figure 4.7 Growth of each circle while subjected to the circle collide operation and linear growth function with a growth factor of 0.5, where 't' varies in an order (a)0→(b)1→(c)3→(d)5→(e)7→(f)9

Figure 4.7 illustrates the circle collide operation, the segment length $'l'$ assigned as the radius of each circle in this operation. The radius of each circle expands linearly with each iteration. This method ensures that the circles will expand without overlapping while also preserving the minimal distance between adjacent paths as they grow. *Figure 4.7(a) – Figure 4.7(f)* shows the gradual increase in the radius of the circles while subjected to circle collision operations during iterations with odd numbers, starting from 0, 1, 3, 5, 7, and 9.

The third conditional operation, ***On Mesh***, is applied to the circles' centers to ensure that all the circles stay within and on the target area (A_T) during each iteration. This operation keeps all circles constrained within the Mesh extracted in the first step (Section 4.2.1) of the algorithm, ensuring that the growing curve accurately fills the target area without exceeding its boundaries. *Figure 4.7(f)* shows that all the circles associated with the growth curve have their centers within the target area. If, at any iteration, the centers of the circles move outside the target area, the growth-curve propagation is terminated, and the user must redefine the input curve to restart the entire process, as illustrated in *Figure 4.8*.

The fourth conditional operation, termed ***Optimum Area Coverage***, is applied to the fully grown growth curve and is implemented as a loop within the toolpath-generation algorithm, as illustrated in *Figure 4.1*. During growth, as the length of each segment increases, the algorithm evaluates the total area covered by the growth curve, $'A_{GC}'$, which is calculated by multiplying the combined length of all segments by the stepover s, and compares it with the target area $'A_T'$. However, the append or delete operation is executed only after the completion of one full growth cycle of the input curve. If the area covered by the growth curve ‘A_{GC}' is smaller than $'A_T'$, an additional segment is appended to the input curve at the initial definition stage (before growth begins), resulting in $N + 1$ segments, and the growth process is repeated. Conversely, if the area covered by the growth curve $'A_{GC}'$ exceeds $'1.05 \times A_T'$, one segment is removed from the input curve, yielding $N - 1$ segments, and the curve is regenerated. This verification and correction cycle continues until the covered area falls within the acceptable range of $'A_T'$ to ‘$1.05 \times A_T'$, where the 5% tolerance accounts for bead overlaps due to the circular nozzle geometry. Once this optimum area-coverage condition is satisfied, the resulting growth curve proceeds to the toolpath-optimization stage.

Figure 4.8 presents the algorithmic flowchart of the conditional operations used in the growth curve–based toolpath generation. After importing the CAD model and defining the target area (AT), step-over (S), growth factor (G), and a closed user-defined input curve, the toolpath is generated through an automated iterative process. A verification–correction step ensures that the input curve is continuous and free of self-intersections. Continuity is confirmed by verifying that the input curve forms a closed loop, while self-intersections are detected through geometric checks between non-adjacent segments as shown in *Figure 4.8*.

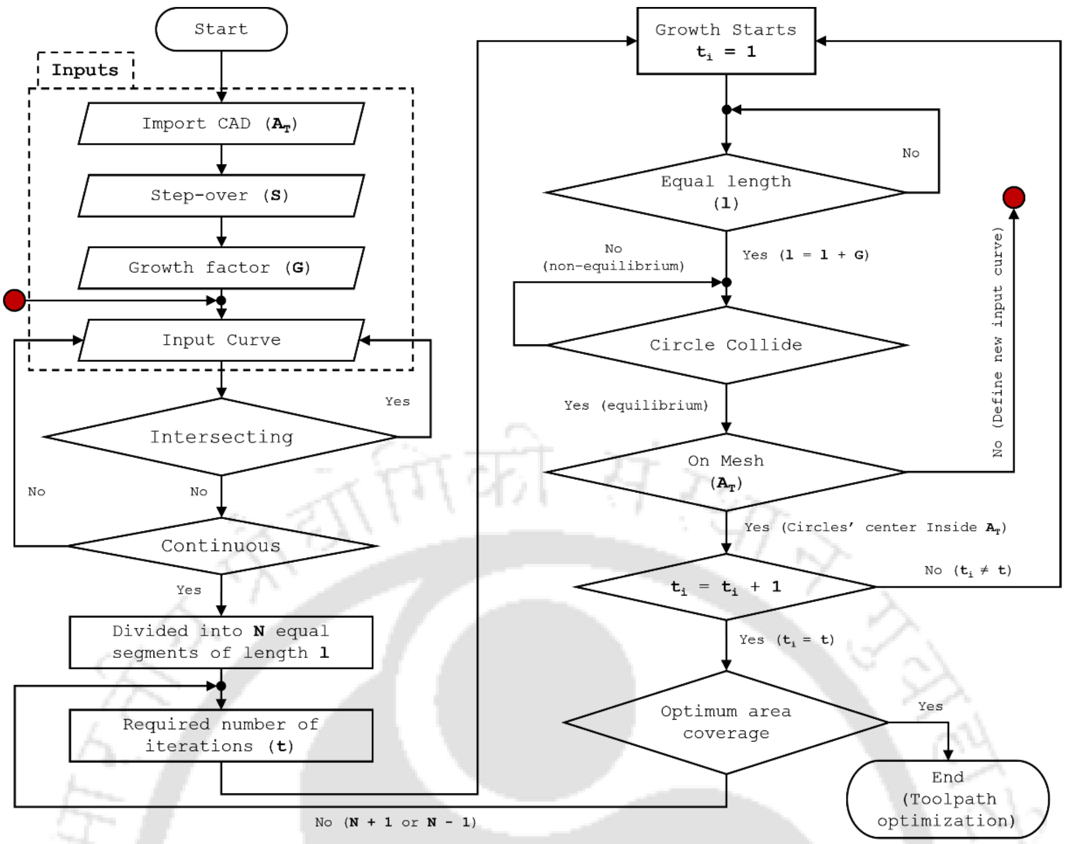

Figure 4.8 Algorithmic flowchart for conditional operations involved in growth curve-based toolpath generation

4.2.5. Toolpath optimization

The fifth step, toolpath optimization, involves three critical operations: boundary trimming, proximity joining, and sharp turns conversion.

The first operation, **Boundary Trim**, is performed on the completely grown growth curve and the target area's outer and inner offset contours. It ensures that the deposited material does not overlap with adjacent beads. Moreover, this step ensures optimal dimensional accuracy in the printed parts where the outer contour is not needed by trimming the completely grown growth curve to coincide with the boundaries of the geometry. *Figure 4.9* illustrates the boundary trim operation. *Figure 4.9(a)* shows the two required curves for the operation, represented by red and yellow colors, intersecting at multiple locations. This process removes the portions of the growth curve that go beyond the offset contours of the target area and replaces those removed sections with corresponding parts of the offset contours. *Figure 4.9(b)* illustrates the growth curve after the completion of the boundary trim operation.

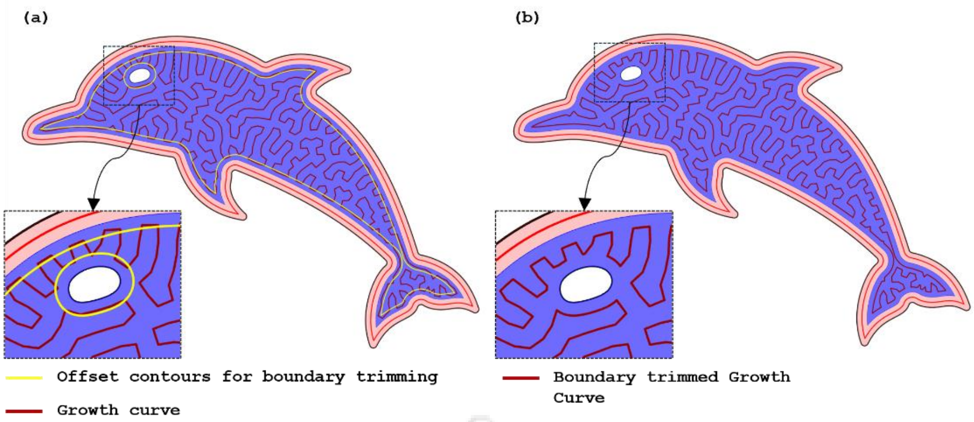

Figure 4.9 Boundary trim operation (a) Before boundary trim and (b) After boundary trim

The second operation, **Proximity Joining**, is executed exclusively when an outer contour is required in the printed geometry and the contour offset operation has been previously applied to the target area. This process involves connecting the full-grown input curve with the offset contour to create a continuous toolpath determined by the step-over. This operation ensures a smooth and uninterrupted connection between the growth curve and the offset contours, enabling a uniform and continuous material deposition. If the printed geometry does not require the outer contour, this operation is skipped, and the algorithm advances directly to the third operation.

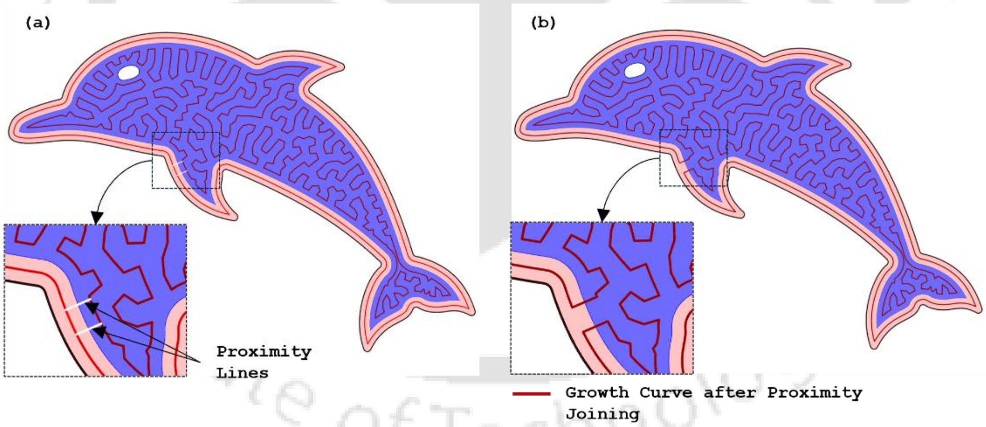

Figure 4.10 Proximity joining operation (a) Finding the proximity lines, (b) After joining the complete growth curve-based toolpath

Figure 4.10 illustrates the proximity joining operation, which includes two basic steps. The first step is to identify the minimal distance between the boundary-trimmed growth curve, and the outer contour offset curve. In the second stage, unnecessary portions of the boundary-trimmed growth curve and the outer contour offset curve get eliminated, leaving a complete and continuous toolpath.

The third operation, **Sharp Turns Conversion**, deals with the sharp turns present in the completely grown growth curve-based toolpath. This toolpath is made up of N segments that are linked together. Each segment with the segment next to it has an angle between 90 and 180 degrees, forming sharp turns. The final toolpath may have sharp turns of less than 90 degrees due to the boundary trim operation. These turns can make the printing speed change quickly, slowing the printer or even making it stop and start suddenly. To resolve this, the sharp turns conversion operation employs a user-specified fillet radius to convert all the sharp turns into a smoother fillet. This fillet is subdivided into 0.2 mm segments, so the angle between segments will be 174.3 degrees. The print head won't slow down or pause at any corner for this angle during printing. Finishing this last step ensures the printing process runs smoothly without interruptions. This will improve the printing quality (consistent material deposition) and reduce mechanical strain on the machinery. The sharp turn conversion is shown in *Figure 4.11*. The final toolpath with sharp turns is displayed in *Figure 4.11(a)*. The toolpath is shown in *Figure 4.11(b)* after applying a fillet radius of 2 mm at every sharp turn.

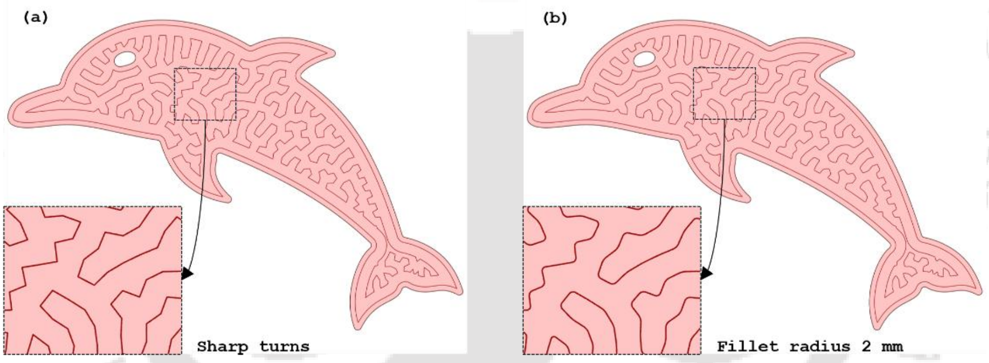

Figure 4.11 Sharp turns conversion (a) Toolpath with sharp turns, (b) Toolpath with 2 mm fillet radius

An experiment was conducted to determine the minimum angle at which the printer can keep the same speed without slowing down, utilizing G-code generated for a polyline. The polyline comprised 20 mm long segments, with the angle between subsequent segments decreasing by 2 degrees at a time, from 180 degrees to 90 degrees. *Figure 4.12(a)* depicts the drawing of the polyline. In contrast, *Figure 4.12(b)* shows the print speed plotted against the turning angle, which indicates that the printer maintains its speed without deceleration at angles of 150 degrees or greater. Therefore, to avoid slowdowns, all turns in the toolpath should have angles exceeding 150 degrees. Any angle below this threshold is considered a sharp turn and may reduce printing speed.

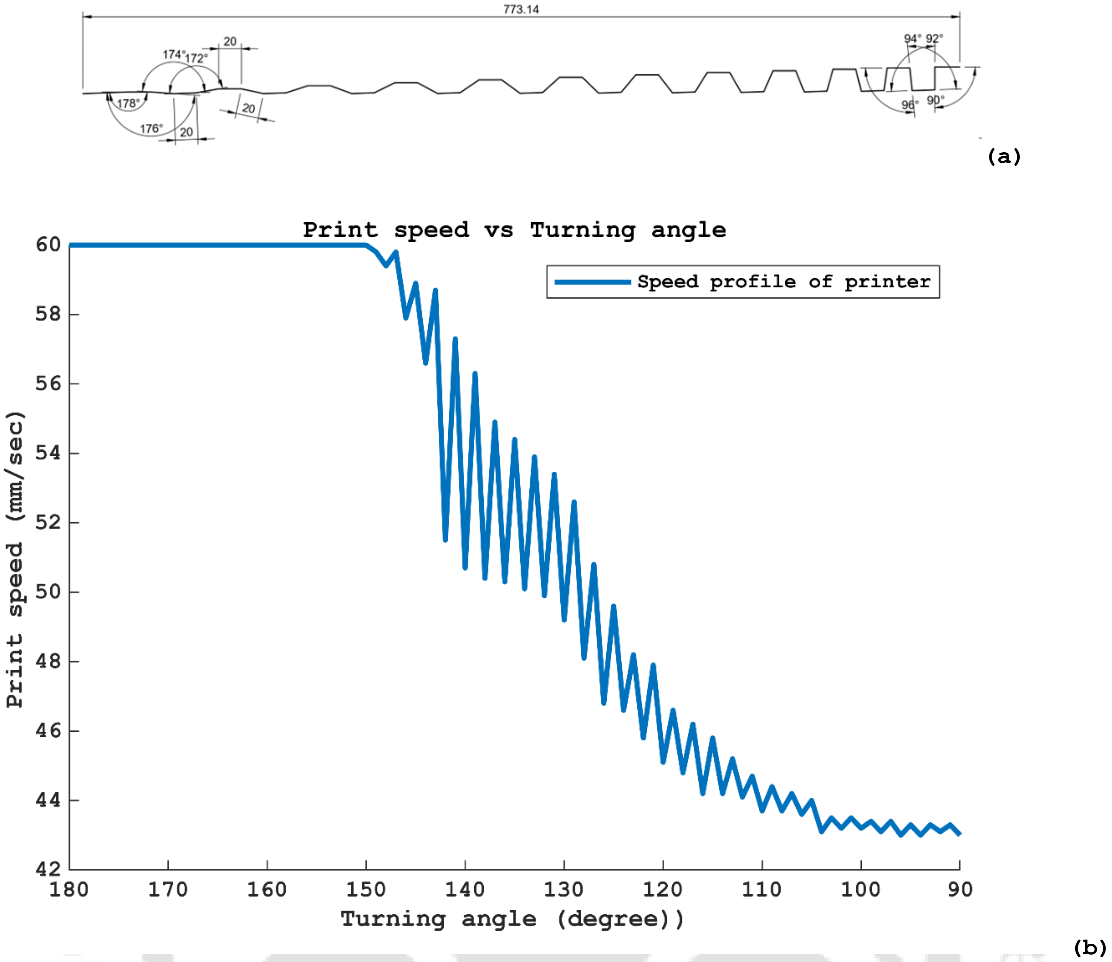

Figure 4.12 (a) Polyline, and (b) Printing speed plotted against the turning angle

To ensure quality and manufacturing process effectiveness, it is advantageous to fabricate parts using continuous material deposition, avoiding any interruptions or discontinuities (Xiao et al., 2021). The choice of toolpaths for a component can vary based on the starting point and the area-filling technique used for each layer. A growth curve-based toolpath, as depicted in *Figure 4.13*, provides a consistent start and end point. The material deposition follows a complete loop, beginning at point 'O' and returning to the same point after filling the region within the specified contour. This pattern can be repeated for each layer, ensuring a consistent start and stop point throughout the production process. Additionally, the user can customize these common start and endpoints to meet specific requirements.

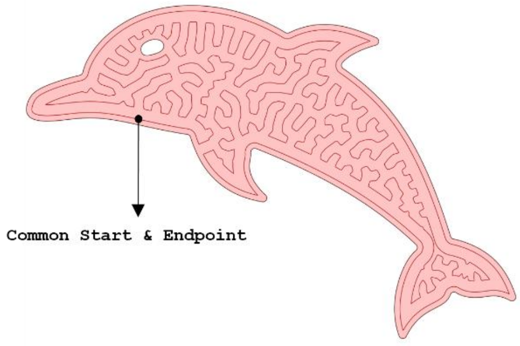

Figure 4.13 Material deposition starts and ends at a common point.

The sixth step of the algorithm involves generating G-code and fabricating parts using AM of concrete technology. G-code creation is an essential part of the AM process. Rhinoceros 7.0's visual coding environment is used to write the script for making G-code. This script takes the data from the growth curve and turns it into G-code directions that direct the 3D printer precisely on how to move and deposit the material. Key input factors, like extracted coordinates, layer height, number of layers, and material density, are used to figure out accurate coordinates, the distances between coordinates, extrusion rates, and an estimate of the amount of printing material required. This G-code generation script links the digital path design and AM processes well. It ensures the path's fine details and complexity are correctly translated into printed objects.

4.3. Parametric studies

This section presents multiple case studies to assess the resilience of the proposed methodology. The algorithm was created using Grasshopper, Rhinoceros 7.0's visual programming environment. A detailed parametric analysis is conducted for six geometries (*Figure 4.14*). Before the analysis begins, two parameters must be fixed for every study. A linear growth function has been selected for this study; the input curve defined for each geometry is the boundary offset curve of the same geometry, not a user-defined input curve. Section 4.3.1 investigates the effect of step-over, Section 4.3.2 investigates the effect of scaling factor, and Section 4.3.3 investigates the effect of growth factors on four dependent parameters: (1) Printing time, (2) Toolpath continuity (nozzle lift and sharp turns), (3) Computation time, and (4) Print quality (underfilling and overlapping).

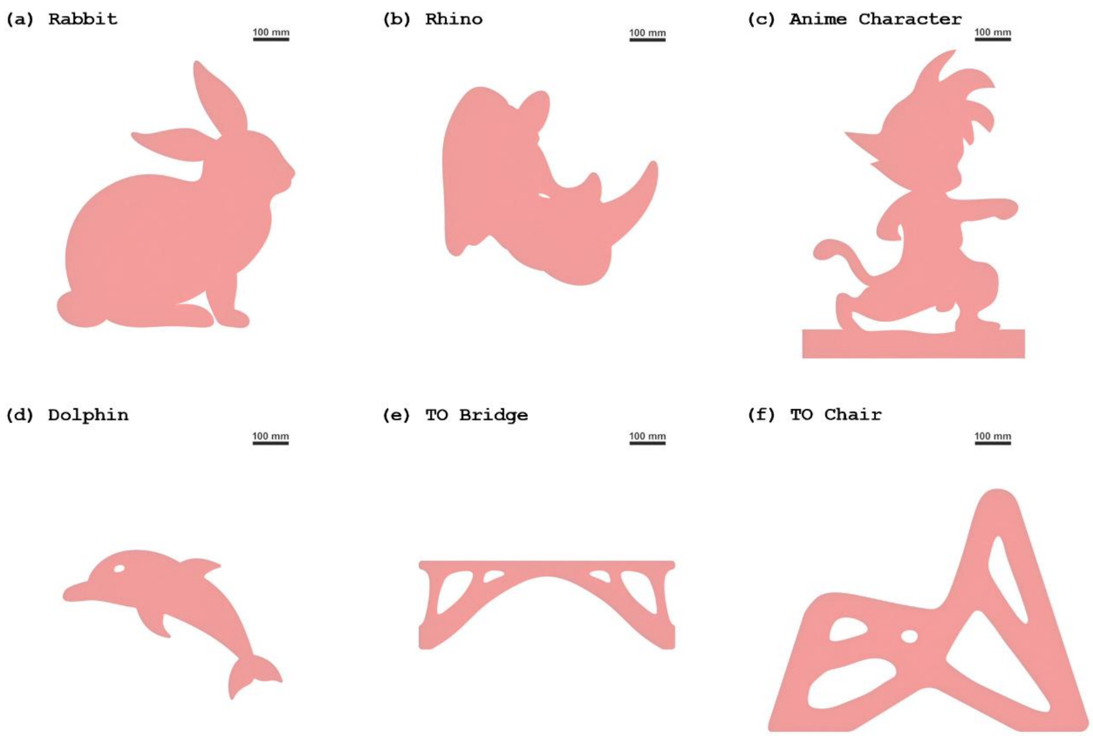

Figure 4.14 Geometries were used to demonstrate the growth curve-based area filling of the continuous toolpath.

Printing time refers to the entire time material is extruded through the print head to create the concrete structure, transforming it from a digital model to a physical object. The printing time calculation is done by fixing the printer's printing speed. **Toolpath continuity** is associated with the number of nozzle lifts and sharp turns in the toolpath. A Sharp turn is the point where the printer decelerates and accelerates again, for an instant, during the printing operation. The optimum value of the sharp turning angle has been calculated in Section 4.2.5. **Computation time** is when the algorithm generates the printer-ready toolpath after providing the necessary inputs without human intervention or the required post-processing (Inputs to G-code). **Print quality** is contingent upon the amount of underfilling and overlapping in the printed object. Underfilling and overlapping should be minimized to achieve optimal print quality while maximizing area coverage.

An approach mentioned in (Bi et al., 2022) is used to quantify print quality in terms of underfill and overlapping. *Figure 4.15* illustrates typical underfilled (blue) and overlapped (yellow) areas in AMoC. Underfilled areas are generated by offsetting the toolpath by 0.5 times the bead width (0.5 * w).

Total overlapping is determined as follows:

$$L * w - A_T \qquad (4.4)$$

Where L, w, and A_T are the total toolpath length, bead width, and the Target area that has been deposited.

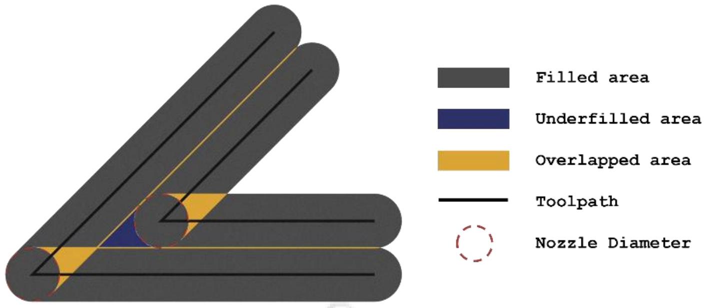

Figure 4.15 Underfilling and overlapping areas in AMoC

4.3.1. Effect of step-over

In this section, by keeping the value of the growth factor (G) equal to 0.5, the effect of the step-over on five dependent parameters has been analyzed. **Step-over 's'** is the lateral space between consecutive paths, significantly influencing printing process efficiency and quality of the printed structure. A growth curve-based toolpath for Dolphin geometry has been generated for different step-over values, as shown in *Figure 4.16.*

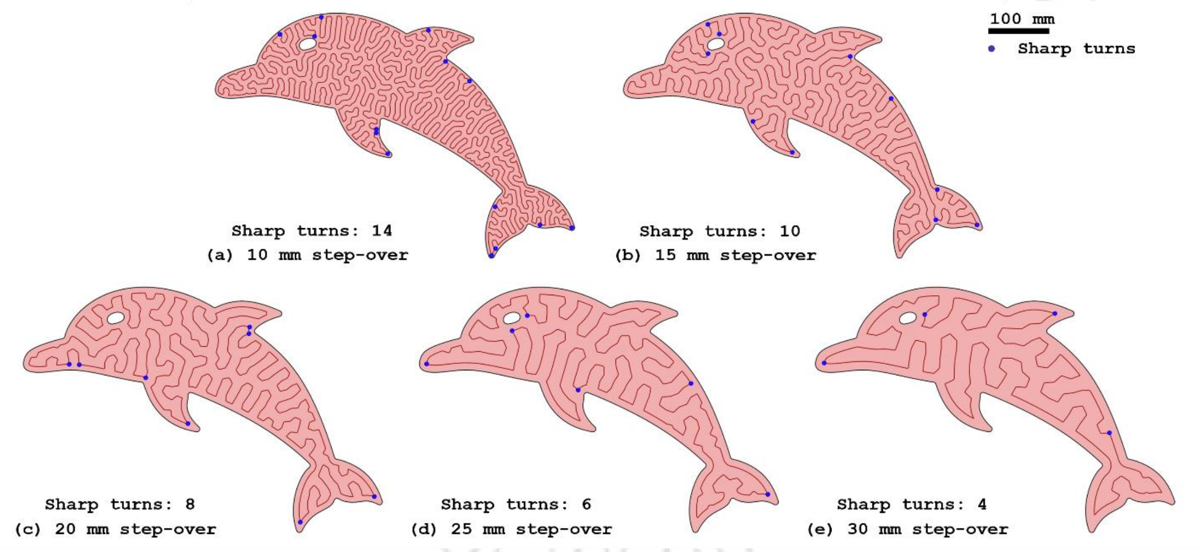

Figure 4.16 Growth curve-based toolpath for Dolphin geometry with different step-overs

As the stepover value increases, the entire length of the toolpath decreases, leading to a significant drop in overall printing time and vice versa. This observation is illustrated in *Figure 4.17,* and results were plotted in *Figure 4.17(a)* for all six geometries for different step-over starting from 10 mm up to 30 mm with an interval of 5 mm with a constant printing speed of 60 mm/s, against the printing time. When the step-over increases from 10 mm to 15 mm, the printing time decreases consistently, ranging from approximately 33.43% to 32.97% across all geometries. A further increase from 15 mm to 20 mm results in a drop of about 25.15% to

24.44%. The reduction continues when the stepover increases to 25 mm, with printing times falling by 20.05% to 19.18%. Lastly, increasing the step-over to 30 mm decreases printing time between 17.52% and 16.16%, reflecting a trend of diminishing returns as the step-over becomes wider. This demonstrates a distinct trend: initial step-over yield increments (10 mm → 15 mm, and 15 mm → 20 mm) significantly decrease printing time, whereas subsequent increases provide diminishing returns. This trend underscores that the initial step-over change significantly influences printing time.

The number of sharp turns (angle < 150°) present in the toolpath changes with a change in step-over values; the lower the step-over, the higher the number of sharp turns available only at boundary-trimmed toolpath, as shown in *Figure 4.16* for Dolphin geometry, and for six geometries, the results were plotted in *Figure 4.17(b)*. When further analysis took place, it was found that none of these sharp turns had an angle < 140°, which reduces the printer speed by nearly 10% of its running speed. Also, these sharp turns are not one after another, so they didn't affect the printing process much.

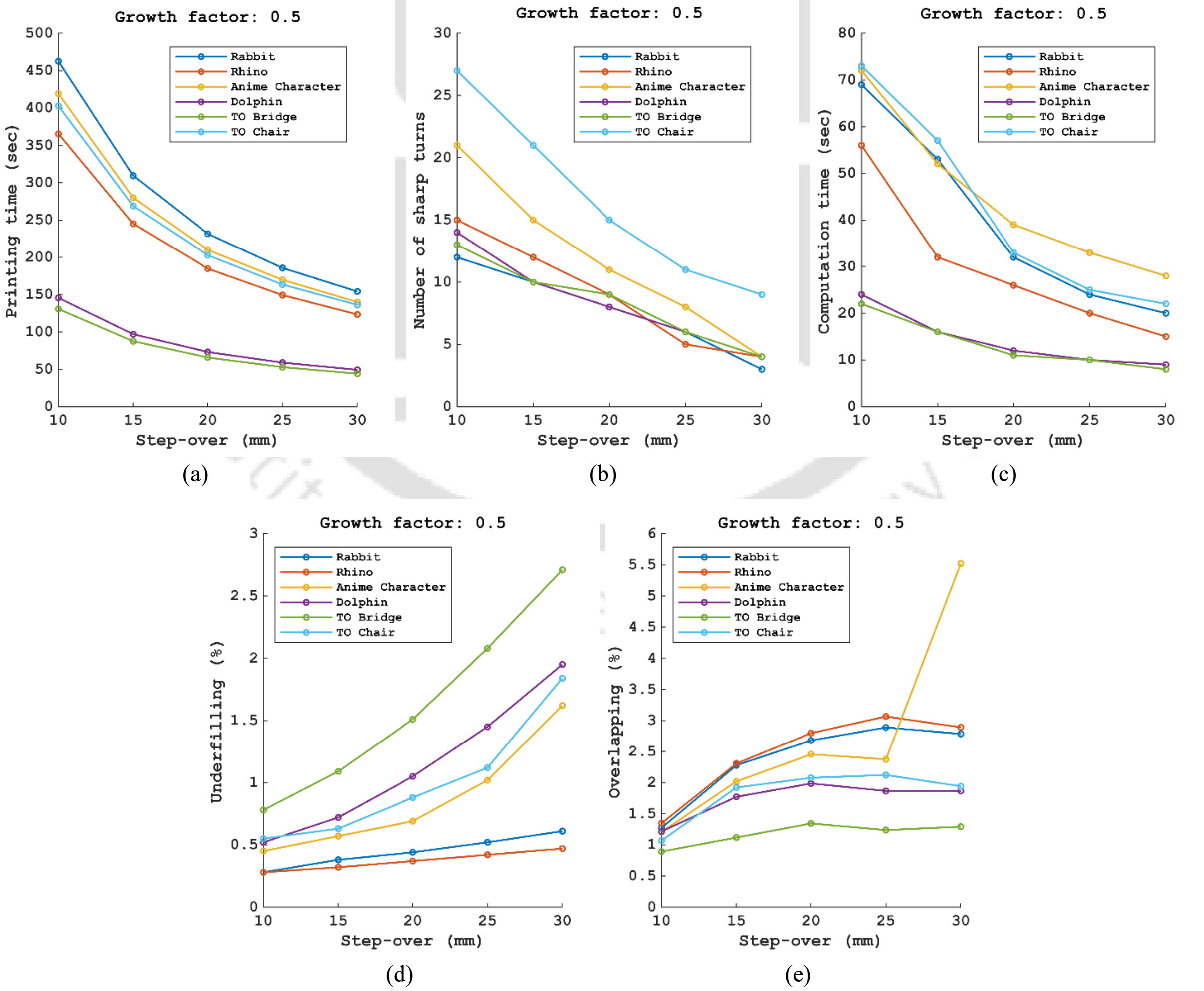

Figure 4.17 Effect of step-over: (a) Printing time, (b) Number of sharp turns, (c) Computation time, (d) Underfilling, and (e) Overlapping

The step-over value primarily affects computation time. Increasing the step-over value reduces the toolpath length, reducing the total number of segments (N) required to generate the toolpath and, consequently, the computation time. This relationship is illustrated in *Figure 4.17(c)* for all six geometries, which demonstrates the inverse correlation between step-over and computation time. As the step-over increases from 10 mm to 15 mm, the computation time decreases by around 18.75% to 39.62%. Further increasing it to 20 mm diminishes computing time, ranging between 15.15% and 42.11%. As the step-over increases from 20 mm to 25 mm, the reduction becomes more modest, generally ranging from 9.09% to 27.78%. Augmenting it to 30 mm yields the least enhancement, with a mere 10.00% to 20.00% reduction. This demonstrates a distinct trend: initial step-over yield increments (10 mm → 15 mm, and 15 mm → 20 mm) significantly decrease computation time, whereas subsequent increases provide diminishing returns. This trend underscores that initial step-over modifications significantly influence computation performance.

Increasing the step-over will affect the print quality of the printed part. *Figure 4.17(d)* demonstrates the effect of step-over on the underfilled area. When there is an increment in the step-over value, the underfilling area in the geometry will increase mainly in the area with acute corners and areas less than the size of the step-over. Analysis shows that the underfilling area in the printed geometry is as low as 0.0028% and as high as 0.0271% for six different geometries. As the step-over increases from 10 mm to 15 mm, underfilling significantly increases, generally from 14% to 40%. Further increasing it to 20 mm maintains this pattern, with underfilling increasing at a moderate rate, typically between 15% and 38%. Similarly, from 20 mm to 25 mm, underfilling remains between the 13% to 38% range. The most substantial increase in underfilling transpires when the step-over attains 30 mm, with increments soaring up to 64% in certain instances. This indicates a distinct pattern: minor step-over increments result in slight underfilling alterations, but greater step-over values, particularly over 20 mm, produce a significantly sharper increase. This underscores the necessity for meticulous calibration of step-over parameters to preserve print quality (underfilling and overlapping).

Figure 4.17(e) demonstrates the effect of step-over on the overlapped area. Analysis shows that the underfilling area in the printed geometry is as low as 0.0089% and as high as 0.055% (for the tail portion of the geometry anime character at a 30 mm step-over) for six different geometries. As the step-over increases from 10 mm to 15 mm, the overlapping area significantly increases, varying from approximately 45% to over 80%. Transitioning from

15 mm to 20 mm results in continued growth, although at a more moderate rate, generally ranging from 8% to 22%. The overlapping values stabilize at approximately the 20 mm threshold, exhibiting minimal variations across most geometries. The tendency stabilizes between 20 mm to 25 mm, with certain instances exhibiting minor declines. Ultimately, elevating the step-over to 30 mm results in predominantly minor alterations; nonetheless, the geometry of the anime character displays strong spikes, with increases surpassing 130% due to its tail portion. The data indicates that overlap increases swiftly with minimal step-over values, stabilizing at approximately 20 mm. This underscores the significance of meticulous step-over selection for regulated material deposition.

This investigation indicates that step-over value is crucial in generating a toolpath for AMoC. Among the assessed values, a step-over of 20 mm consistently emerges as the ideal selection. This setting substantially decreases printing time, number of turns, and computing time. Furthermore, underfilling is maintained below or nearly 1.5% across all geometries, ensuring solid material coverage, while overlapping values remain around 3%, avoiding excessive material accumulation. This balance renders 20 mm an efficient and practical step-over for high-quality, continuous toolpath in AMoC applications.

4.3.2. Effect of scale factor

In this section, the effect of the scale factor on four dependent parameters has been analyzed by keeping the value of the growth factor (G) equal to 0.5 and an optimized step-over value of 20 mm. **Large-scale** geometry in AMoC addresses the demand for efficient, customizable, and complex structures. Conventional techniques encounter difficulties with intricate geometries, elevated labor demands, and material wastage—challenges that AMoC addresses via meticulous, layer-by-layer printing. It eliminates formwork, reduces construction time, and utilizes materials economically, rendering it optimal for modern construction and infrastructure. A uniform scale factor (1 to 5) is applied to all six geometries to analyze the growth curve-based toolpath for large-scale geometries. This facilitates uniform assessment of print behavior and performance across various sizes while preserving the proportional integrity of each design. *Figure 4.18* shows the growth curve-based toolpath for Dolphin geometry with a 20 mm step-over and different scale factors.

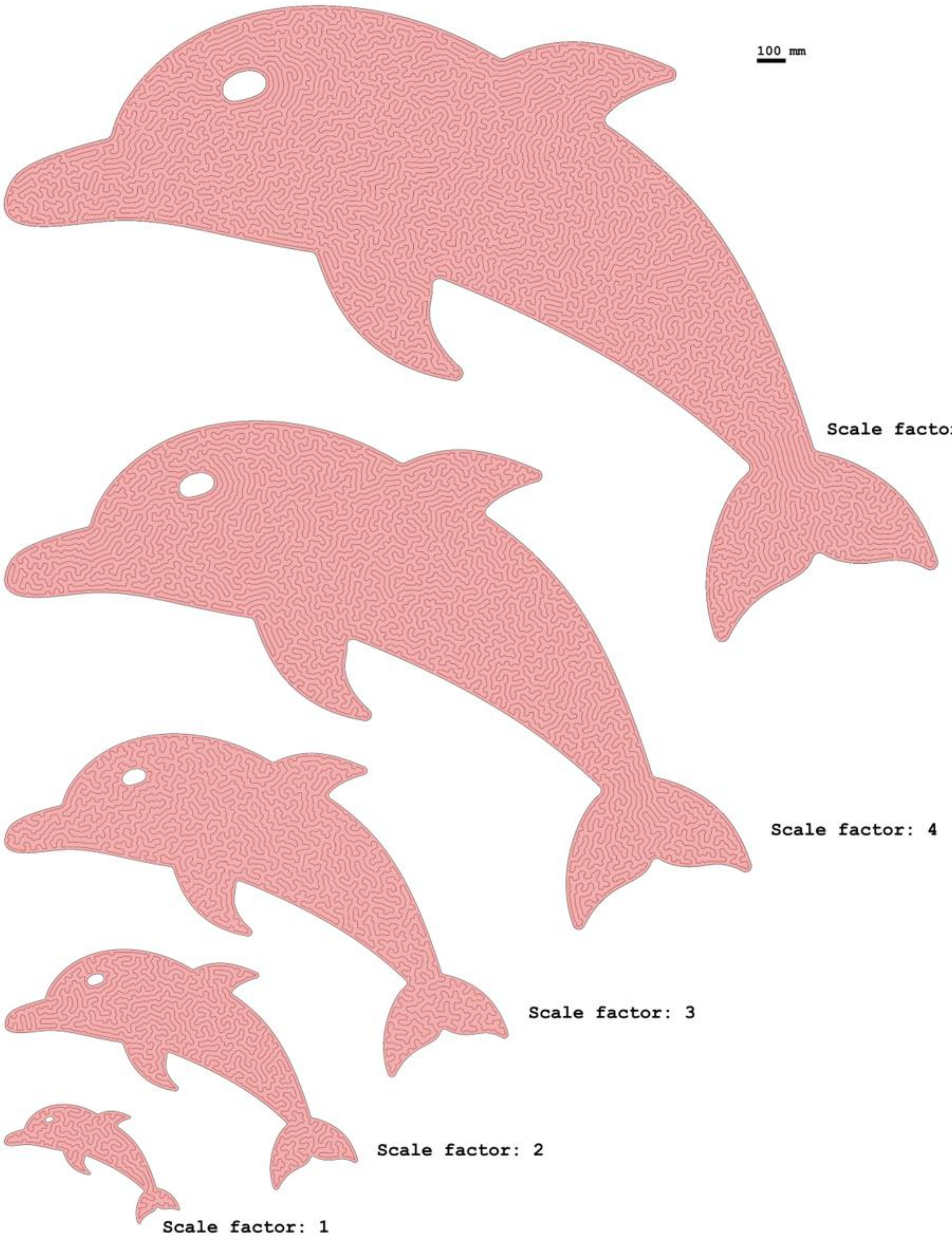

Figure 4.18 Growth curve-based toolpath for Dolphin geometry with a 20 mm step-over and for different scale factors (1 - 5)

The printing time was determined to be directly proportional to the square of the scale factor, consistent with the hypothesis that the printed area rises quadratically with scaling. This relationship is depicted in *Figure 4.19(a)*. The number of sharp turns escalated linearly with the scale factor, as larger geometries inherently incorporate more boundary-trimmed sections proportional to the area. This tendency is illustrated in *Figure 4.19(b)*. Computation time showed a quadratic increase with the scale factor, following the area expansion trend, which is illustrated in *Figure 4.19(c)*.

Regarding print quality, the analysis of underfilling values across several scale factors indicates that the variations are modest for all geometries. Regardless of scale changes, the underfilling consistently remains less than 1% as shown in *Figure 4.19(d)*, exhibiting only minor differences across various scenarios. This signifies that the growth curve-based toolpath generation method ensures consistent material distribution, irrespective of the geometry's dimensions. This consistency is essential in AMoC, ensuring constant structural integrity and surface quality without necessitating continual parameter modifications for different scales.

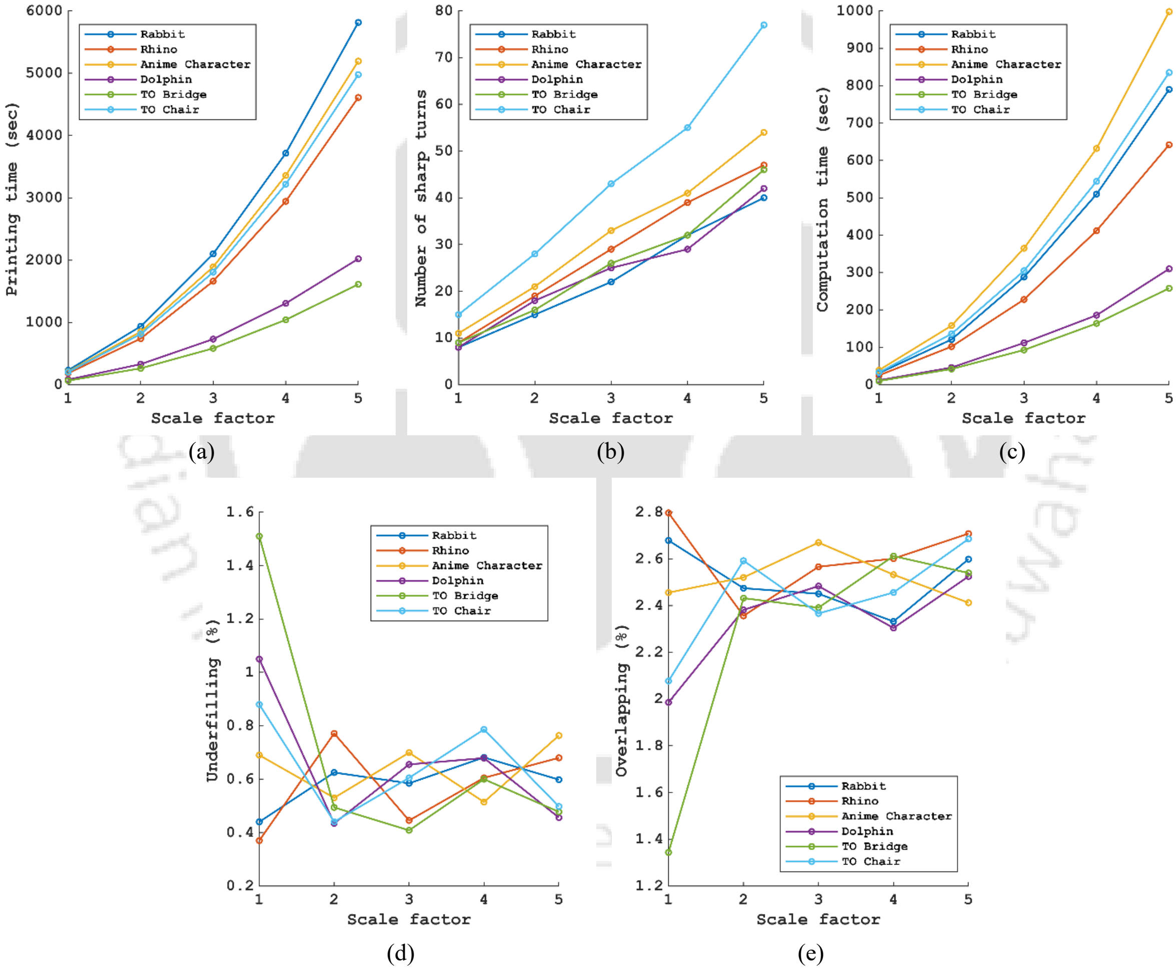

Figure 4.19 Effect of scale factor: (a) Printing time, (b) Number of sharp turns, (c) Computation time, (d) Underfilling, and (e) Overlapping

A comparable tendency is evident in the overlapping values across several scale factors. Despite showing slightly more variance than the underfilling data, the changes remain within a relatively limited and acceptable range across all geometries. The overlapping percentages remain remarkably steady, oscillating between roughly 2% and 3% as shown in *Figure 4.19(e)*.

No substantial variations have been observed that suggest inconsistency or the potential for over-deposition. This indicates that, regardless of scaling, the growth curve-based toolpath generation method efficiently controls material overlap. This stability ensures consistent print quality, reducing hazards such as surface bulging or material waste, which is crucial for achieving uniform and precise constructions in AMoC.

This section emphasizes that the growth curve-based print method provides better print quality with underfilling <0.015 and overlapping <0.03, for large-scale geometries in AMoC. Nevertheless, while it has better print quality the computational time for large-scale geometries is excessive. Consequently, additional optimization of the toolpath is essential to enhance computation time efficiency for large-scale geometries.

4.3.3. Effect of growth factor

The growth function is kept linear from the start, so the study of different factors on various parameters can be established. This linear growth function has a constant growth factor of 0.5 in the previous sections. This section analyzes the effect of the growth factor on the same four dependent variables. Growth factor (G) theoretically can be anything greater than 0 to $\left(\frac{S}{2} - l\right)$ here, l is the initial segment length of the input curve. The lower the growth factor, the greater the number of iterations (t) required by the growth curve to fill an area and vice versa. As the number of iterations increases, the computation time also increases. The first parameter, printing time, depends only on step-over and scale factor values, but not on the growth factor, hence omitting it from the analysis. *Figure 4.20* shows the growth curve-based toolpath for Dolphin geometry with different growth factors starting from 0.5 and then divided into four equal parts up to $\left\{\left(\frac{20}{2} - 4.19\right) or\ 5.81\right\}$. For dolphin geometry, input the curve's initial segment length (l) is 4.19 mm, and a growth factor below 0.5 has been omitted from this study as it will increase the computation time.

As the initial segment's length (l) and the number of segments (N) of the input curve of each geometry are not the same, thus, to establish this study, the growth factor set to varies from 0.5 to 4 with an interval of 0.5, so that there are 2-3 extra iterations available for the growth curve to expand completely within the target area.

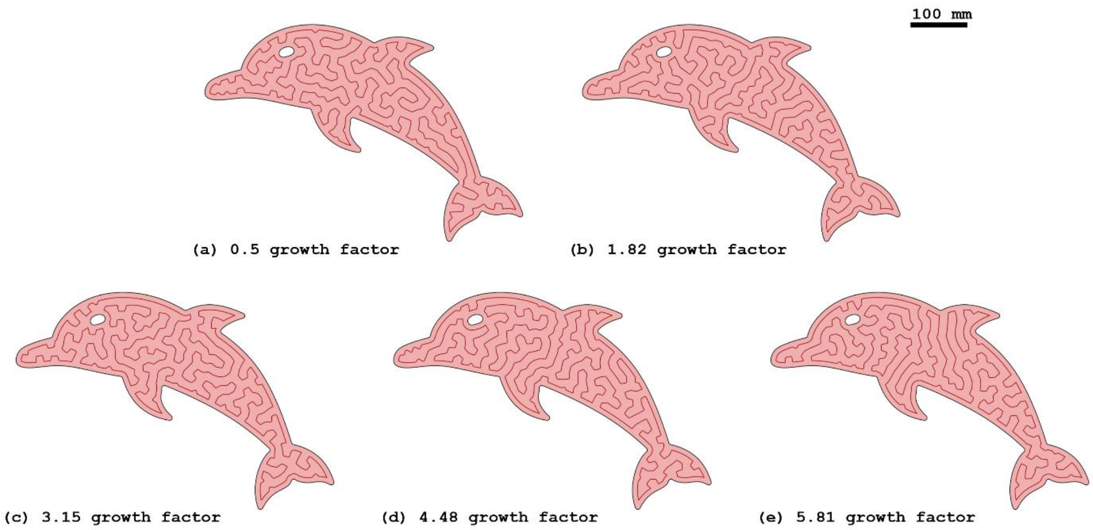

Figure 4.20 Growth curve-based toolpath for Dolphin geometry with different growth factors

Figure 4.21(a) demonstrates that the number of sharp turns remains consistently stable across all geometries, irrespective of variations in growth factor values. *Figure 4.21(b)* illustrates the effect of the growth factor on computational time. As the growth factor increases, the computation of time uniformly diminishes across all geometries; however, the degree of reduction fluctuates with each increment. As the growth factor rises from 0.5 to 1, the computation time diminishes by 16.7% to 36.0%. The reduction varies from 16.7% to 31.3% as the growth factor increases from 1 to 1.5, followed by a further decline of 14.3% to 27.3% when the growth factor increases from 1.5 to 2. A slight reduction is noted as the growth factor rises from 2 to 2.5, with computation time decreasing by 0.0% to 20.0%. Exceeding a growth factor of 2.5 does not noticeably alter computation time, suggesting a saturation point in computational efficiency. This investigation was conducted at a scale factor of 1, where the decrease in time required for computation is less significant, as all toolpaths were generated within 40 seconds.

Figure 4.21(c) illustrates that, at a scale factor of 5, the increase of the growth factor significantly affects computation time, particularly inside the lower growth factor spectrum. As the growth factor escalates from 0.5 to 1.0, the computation time decreases considerably by 47.3% to 48.5%. The reduction continues from 1.0 to 1.5, with a decrease of 31.3% to 33.8%, succeeded by a more pronounced loss of 40.0% to 45.5% from 1.5 to 2.0. Nonetheless, as the growth factor escalates, the rate of decrease declines. Between 2 and 2.5, computation time varies from a modest rise of 3.3% to a drop of 5.6%. The transition from 2.5 to 3.0 ranges from a 3.9% increase to a 2.4% decrease. The pattern is consistent from 3.0 to 3.5 and 3.5 to 4.0, with slight rises and minimal reductions in computation time. This investigation demonstrates that growth curve-based toolpath creation for large-scale structures is computationally efficient, significantly reducing computation time.

The analysis of underfilling values across various growth factors indicates that the variations in print quality are minimal for all geometries. Despite variations in growth factor, underfilling constantly remains below 1.5%, as illustrated in *Figure 4.21(d)*, exhibiting only negligible variations across various scenarios. A comparable pattern is noted in the overlapping values among several growth factors. The overlap demonstrates marginally greater variance than underfilling; however, the discrepancies remain within a limited and acceptable range for all geometries. The overlapping remains stable, varying between 1.2% and 3%, as depicted in *Figure 4.21(e)*. No substantial variances have been observed, suggesting problems such as over-deposition or inconsistency in material deposition.

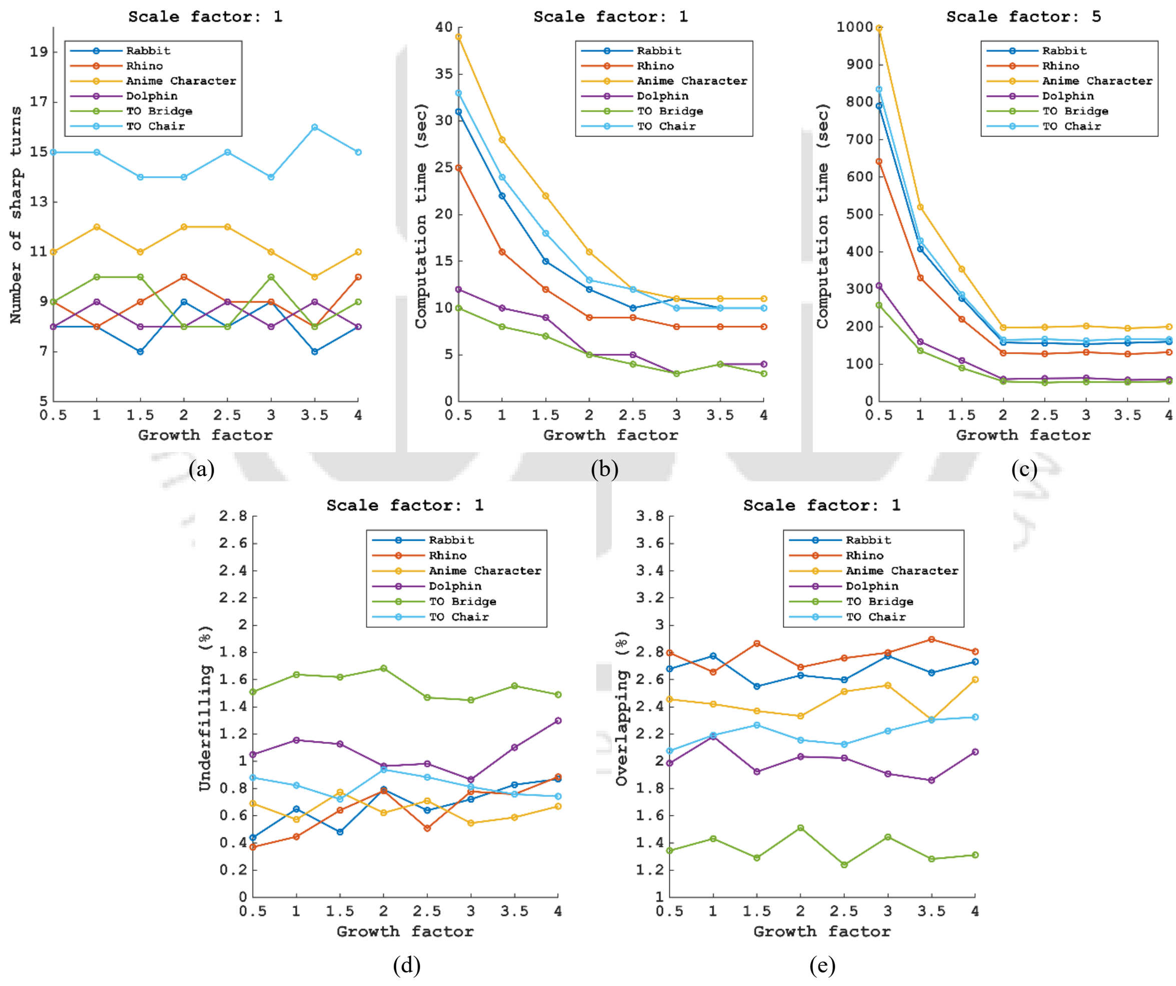

Figure 4.21 Effect of growth factor: (a) Number of sharp turns, (b)Computation time (Scale factor: 1), (c) Computation time (Scale factor: 5), (d) Underfilling, and (e) Overlapping

This section highlights that the growth curve-based toolpath generation method ensures exceptional print quality for all growth factor values. Nonetheless, although print quality remains outstanding, computational efficiency exhibits a distinct turning point. In large-scale geometries, the computation time decreases markedly as the growth factor rises, attaining peak efficiency at 2. Beyond this point, the computation time stabilizes, yielding minimal to no further advantage. This signifies that growth factor 2 achieves optimal computation.

Figure 4.22 illustrates the growth curve-based toolpaths for all six geometries using consistent input configurations. Each geometry was processed with a 20 mm step-over and a scale factor of 1, utilizing a contour offset as the input curve. The employed growth function was linear, with a growth factor of 2, identified as the ideal number for maximizing computing efficiency while maintaining print quality. The resultant toolpaths illustrate the method's capacity to ensure complete coverage of the target area while conforming to uniform material distribution requirements.

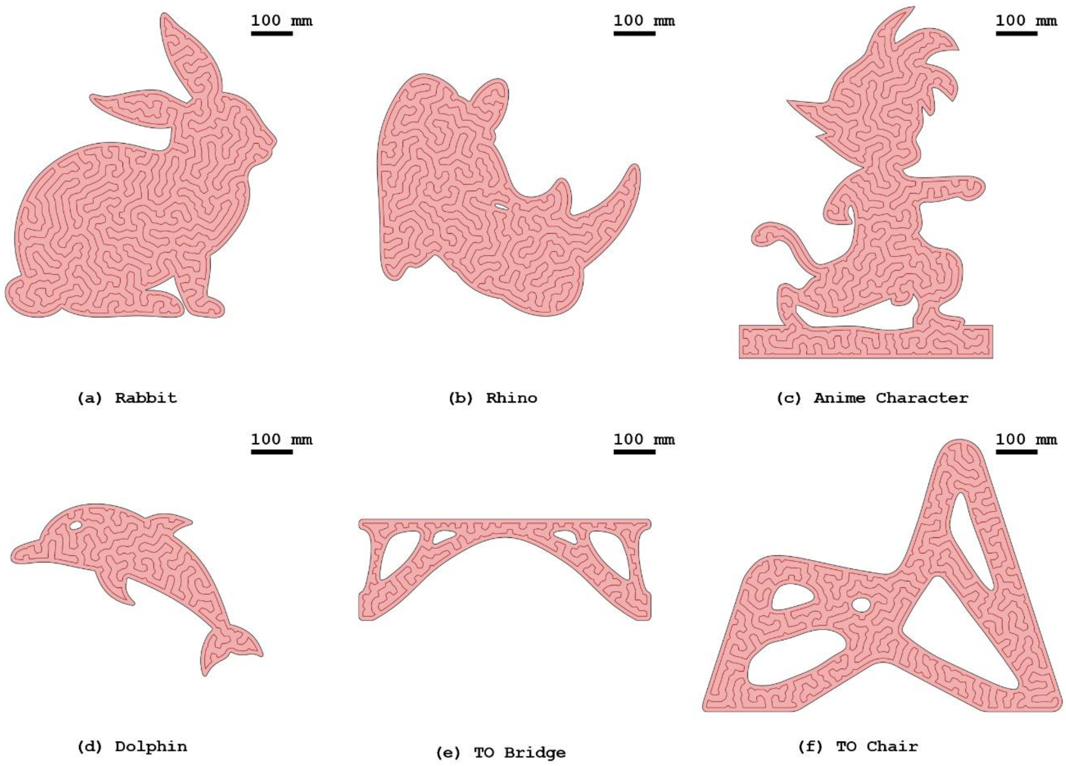

Figure 4.22 Growth curve-based toolpath for six geometries for a 20 mm step-over, with scale factor 1 and growth factor 2

4.4. Comparative analysis

This section compares the growth curve-based toolpath and three distinct area-filling methods, evaluated at two scale factors: 1 and 5. Among these strategies, two conventional approaches in AM—zigzag and contour parallel—are generally utilized for their simplicity and ease of implementation. The third approach is a continuous toolpath based on the TSP, devised by the authors in their previous work (Sahu & Panda, 2025) to improve continuity, print quality, and eliminate non-printing motions. This analysis compares these strategies to the growth curve-based strategy, emphasizing their relative effectiveness in printing time, path continuity, print quality, and computational efficiency across various geometries and scales. To ensure fairness and accuracy in performance assessment, all comparisons were conducted under consistent hardware settings on the same machine, which included an Intel(R) Core(TM) i7-11700K processor, 32 GB of RAM, and a NVIDIA Quadro T600 4GB GDDR6 Graphics Card. *Table 4.1* presents the analytical data used to compare different parameters for all six geometries.

Table 4.1 Analytical data for comparing different area-filling toolpath strategies.

Toolpaths →	**Scale factor 1**				**Scale factor 5**			
Parameters ↓	***Zigzag***	***Contour parallel***	***TSP***	***Growth curve***	***Zigzag***	***Contour parallel***	***TSP***	***Growth curve***
	Rabbit							
Printing time (sec)	255.15	301.93	**230.25**	*232.73*	5836.54	6103.48	**5811.64**	5815.05
Number of lifts	5	14	**1**	**1**	5	57	**1**	**1**
Number of sharp turns	77	66	**9**	**8**	352	296	**46**	**40**
Underfilling (%)	0.0451	0.0354	0.0268	**0.0044**	0.0127	0.0137	0.0298	**0.0059**
Overlapping (%)	0.0869	0.0998	0.0973	**0.0263**	0.0901	0.0880	0.0896	**0.0259**
Computation time (sec)	**3**	4	35	10	**18**	25	3150	160
	Rhino							
Printing time (sec)	222.40	238.88	**182.56**	184.07	4650.25	4892.01	**4606.87**	4610.41
Number of lifts	8	11	**1**	**1**	8	55	**1**	**1**
Number of sharp turns	78	76	**8**	**9**	366	328	**41**	**47**
Underfilling (%)	0.0527	0.0382	0.0288	**0.0037**	0.0193	0.0146	0.0246	**0.0067**
Overlapping (%)	0.0958	0.0878	0.0826	**0.0269**	0.0853	0.0993	0.0898	**0.0270**
Computation time (sec)	**3**	4	30	8	**16**	22	2700	132
	Anime Character							
Printing time (sec)	268.41	321.29	**208.65**	211.38	5253.41	5562.29	**5189.65**	5193.45
Number of lifts	12	22	**1**	**1**	12	72	**1**	**1**
Number of sharp turns	144	164	**12**	**11**	563	797	**62**	**54**
Underfilling (%)	0.0598	0.0306	0.0246	**0.0069**	0.0132	0.0173	0.0302	**0.0076**
Overlapping (%)	0.0880	0.0925	0.0956	**0.0233**	0.0825	0.0918	0.0978	**0.0221**
Computation time (sec)	**4**	5	57	11	**21**	28	5130	200
	Dolphin							
Printing time (sec)	116.4	122.5	**81.54**	82.05	2063.5	2162.04	**2018.68**	2021.00
Number of lifts	7	8	**1**	**1**	9	28	**1**	**1**
Number of sharp turns	53	47	**7**	**8**	199	138	**35**	**42**
Underfilling (%)	0.0436	0.0319	0.0233	**0.0105**	0.0169	0.0135	0.0254	**0.0045**
Overlapping (%)	0.0947	0.0897	0.0845	**0.0203**	0.0884	0.0916	0.0889	**0.0252**
Computation time (sec)	**2**	**2**	16	4	**11**	12	1440	54
	TO Bridge							
Printing time (sec)	153.76	135.8	**64.12**	65.50	1669.41	1865.65	**1609.65**	1612.04
Number of lifts	18	14	**1**	**1**	12	50	**1**	**1**
Number of sharp turns	21	25	**10**	**9**	325	144	**52**	**46**
Underfilling (%)	0.0579	0.0347	0.0262	**0.0151**	0.0181	0.0159	0.0226	**0.0047**
Overlapping (%)	0.0912	0.0880	0.0845	**0.0123**	0.0918	0.0856	0.0846	**0.0213**
Computation time (sec)	**2**	3	22	3	**9**	14	1980	59
	TO Chair							
Printing time (sec)	269.7	302.38	**199.98**	202.423	5052.24	5443.60	**4972.56**	4977.26
Number of lifts	14	20	**1**	**1**	16	92	**1**	**1**
Number of sharp turns	151	51	**16**	**15**	647	253	**84**	**77**
Underfilling (%)	0.0493	0.0395	0.0212	**0.0088**	0.0149	0.0168	0.0240	**0.0049**
Overlapping (%)	0.0862	0.0909	0.0623	**0.0212**	0.0903	0.0899	0.0954	**0.0278**
Computation time (sec)	**5**	7	82	10	**23**	32	7380	166

4.4.1. Printing time and time interval

The comparative analysis of printing time at scale factor 1 indicates that the growth curve-based toolpath significantly enhances efficiency compared to traditional methods. The growth curve-based method reduces printing time by 8.8% to 57.4% compared to the zigzag strategy, demonstrating a significant enhancement in speed across all geometries. Compared to the contour parallel strategy, it shows considerable enhancement, with reductions between 22.9% and 51.8% in printing time. Compared to the TSP-based continuous toolpath, the growth curve-based strategy has comparable performance, with a marginal increase in printing time ranging from 0.6% to 2.2%. This indicates that although the growth curve method is exceptionally effective compared to conventional toolpath strategies, it aligns with the highly optimized TSP-based strategy. For a scale factor of 5, the growth curve-based strategy exhibits negligible variations in printing time relative to zigzag and TSP strategies. Yet, it provides a significant decrease of 4.7% to 13.6% compared to the contour parallel strategy.

The mechanical performance of 3D-printed concrete depends upon the strategic positioning of the start and end points of the toolpath, which must be established before printing starts. Research conducted by Le et al., (2012), Feng et al., (2019), and Nerella et al., (2019) indicates that the interfacial bond strength of 3D-printed concrete diminishes as the time intervals between consecutive layers increase. The growth curve-based toolpath technique employs a consistent start and end point, facilitating uniform time intervals between layer depositions throughout the process. This method promotes improved consistency in interfacial bond performance in AMoC, potentially enhancing the overall structural integrity of the printed components.

4.4.2. Toolpath continuity

In AMoC, ensuring continuity in the toolpath is crucial for attaining optimal structural integrity and effective material deposition. The growth curve-based toolpath resolves this issue by minimizing interruptions by decreasing unnecessary nozzle lifts and retractions, which are frequently linked to defects like weak or cold joints. This method ensures consistent material flow, minimizing transition times, decreasing the likelihood of nozzle blockage, and enhancing overall print quality. *Table 4.1* demonstrates that the number of nozzle lifts in the growth curve-based technique is eliminated, closely corresponding with the continuous TSP-based toolpath. Conversely, traditional methods such as zigzag and contour necessitate frequent nozzle lifts, rendering them more prone to printing defects and inefficiencies.

The growth curve-based toolpath consistently exhibits a notable decrease in sharp turns and directional changes at both scale factor 1 and scale factor 5. As shown in *Table 4.1*, at the lower scale, it attains a reduction of 57.1% to 92.4% compared to the zigzag strategy, and 64.0% to 93.3% relative to the contour parallel strategy, yielding a more streamlined and efficient path configuration. Compared to the TSP-based strategy, the variations are minimal, from an 11.1% decrease to a 14.3% rise, indicating that both strategies maintain low sharp turn counts. The same pattern continues on a larger scale, with sharp turns diminished by 78.9% to 90.4% compared to zigzag and 68.1% to 93.2% relative to contour parallel, underscoring its enhanced path continuity. Relative to TSP, the variation spans a 13.0% decrease to a 20.0% rise, signifying comparable performance. The results validate the efficacy of the growth curve-based strategy in reducing directional deviations, facilitating more uniform deposition, and enhancing structural uniformity across various sizes.

4.4.3. Print quality

The underfilling and overlapping areas measure print quality; both should be as minimal as possible for excellent print quality. At a scale factor of 1, the growth curve-based toolpath attains the minimal underfilling area across all geometries, with values consistently below 0.015. Zigzag and contour parallel toolpath exhibit higher underfilling regions, reaching up to 0.060, while the TSP-based toolpath performs better but still ranges between 0.021 and 0.030. This underscores the growth curve method's enhanced control over material deposition. At a scale of 5, the underfilling values for the growth curve strategy range from 0.0045 to 0.0076. Zigzag varies from 0.0127 to 0.0193, contour from 0.0135 to 0.0173, and TSP from 0.0226 to 0.0302. The growth curve approach remains best despite the decrease in the underfilling area at larger scales for all the strategies.

When it comes to overlapping, at a scale factor of 1, the growth curve-based strategy consistently exhibits the lowest overlapping values, ranging from 0.0123 to 0.0269. In contrast, zigzag has an overlap between 0.0862 and 0.0958, contour between 0.0880 and 0.0998, and TSP between 0.0623 and 0.0973. A similar tendency of overlap was observed at a scale factor of 5. This signifies that the growth curve toolpath allows greater control over material overlap, diminishing the risk of over-deposition and affirming its efficacy in achieving precise material placement, even at larger scales.

4.4.4. Computation time

Conventional toolpath generating strategies rely on straightforward, non-optimized algorithms, yielding minimal computation time, even at large scales. This renders them far more computationally efficient than complex solutions that utilize optimization, such as those based on the TSP and growth curve-based toolpaths. *Table 4.1* illustrates that these conventional strategies surpass continuous strategies regarding time for computation.

At a scale factor of 1, the growth curve-based technique markedly reduces the computation time relative to the TSP-based strategy across all six geometries. The TSP approach requires 16 to 82 seconds, but the growth method finishes computations in 3 to 11 seconds. This signifies a decrease between 71.4% and 87.8%. The significant reduction in time required for computation underscores the efficacy of the growth curve-based strategy. At a scale factor of 5, the growth curve-based strategy substantially reduces computation time relative to the TSP-based strategy. The computation time for TSP varies from 1,440 to 7,380 seconds, but the growth curve-based technique accomplishes toolpath development in about 54 to 200 seconds. This yields a 94.9% to 97.3% decrease in computation time, demonstrating that the growth curve-based approach is highly effective for large-scale geometry processing, substantially reducing computational needs without sacrificing print quality.

4.4.5. Mechanical property

Concrete blocks measuring 160 × 160 × 160 mm^3 (length × width × height) were made utilizing four toolpath strategies: zigzag, contour parallel, TSP-based, and growth curve-based. Following manufacturing, directional markers were added to the surfaces of each specimen. Following a 28-day curing period, the blocks were compressed on a hydraulically operated compression testing machine (CTM) with a load capability of 2000 kN. The load was applied continuously at a rate of 1000 N/s until failure occurred. To assess the anisotropic behavior of 3D-printed objects, specimens were compressed in the X, Y, and Z dimensions using each toolpath technique.

Section 3.2.6 describes how to determine the anisotropic coefficient (I_{3D}) of printed specimens. Section 2.2 describes the material composition and printing method, as the compressive strength of 3D-printed items is largely reliant on layer orientation for a given process-material combination. Each value reported is the median of three replicates. *Figure 4.23(a)* shows that the Z-direction compressive strengths of all four toolpaths are nearly equivalent, which may be attributable to the comparable toolpath length deposited by layer. As depicted in *Figure*

4.23(c), under X and Y loading directions, weak vertical planes arise due to voids between filaments, which function as favored crack propagation sites, resulting in poor compressive performance. This directional difference causes the observed anisotropy in 3D-printed concrete (Figure 4.23(b)).

When the anisotropy levels were evaluated across the four methods, the Growth curve-based toolpath showed the least directional fluctuation, with an anisotropy reduction of 56.0% compared to Zigzag, 54.6% compared to Contour parallel, and 25.7% compared to the TSP-based toolpath. This demonstrates that the growth curve-based technique is the most effective at reducing anisotropic behavior in 3D-printed concrete.

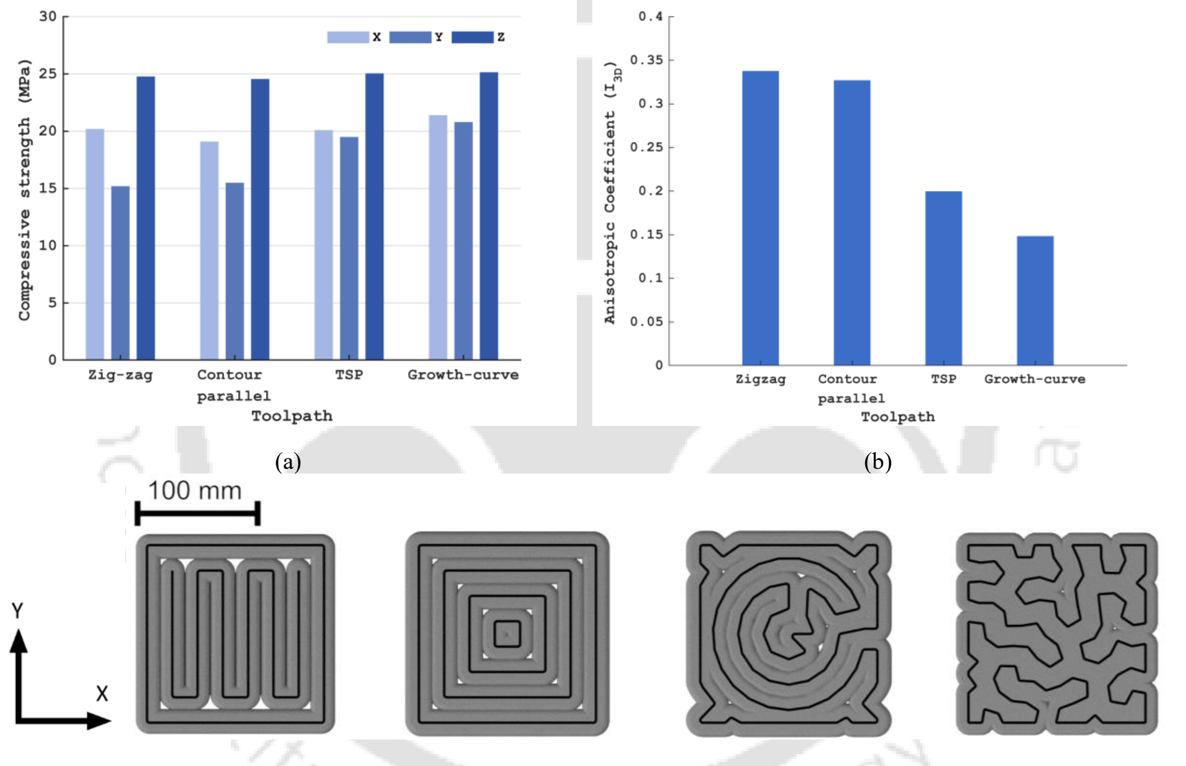

Figure 4.23 The effect of toolpaths on (a) 28-day compressive strength, (b) Anisotropic coefficient, and (c) Voids at the inter-filament vertical planes

4.5. Experimental validation and discussion

Experiments were carried out using a gantry printer and 3D mortar material mix as discussed in section 2.2.2, on four different geometries: Rabbit, Rhino, Anime Character, and Dolphin. These geometries were additively manufactured by utilizing the growth curve-based toolpath with a 20 mm step-over, as shown in Figure 4.24. The print quality of the manufactured components was evaluated and compared to the analytical results presented in Table 4.2. The discrepancies between the experimental and analytical results were minimal, therefore experimentally corroborating the proposed methodology for attaining good print quality (underfilling <0.015 and overlapping <0.03) in large-scale 3D printed geometries. Regarding the results of print quality, Underfilling is calculated using image processing of pixels with different colors. In contrast, the overlapping was kept the same by assuming the bead width deposited equals the step-over of 20 mm.

Table 4.2 Print quality validation for growth curve-based toolpath

	Analytical data		Experimental data	
Geometries	***Underfilling (%)***	***Overlapping (%)***	***Underfilling (%)***	***Overlapping (%)***
Rabbit	0.0044	0.0208	0.0051	0.0208
Rhino	0.0037	0.0270	0.0082	0.0270
Anime Character	0.0069	0.0233	0.0078	0.0233
Dolphin	0.0105	0.0203	0.0145	0.0203

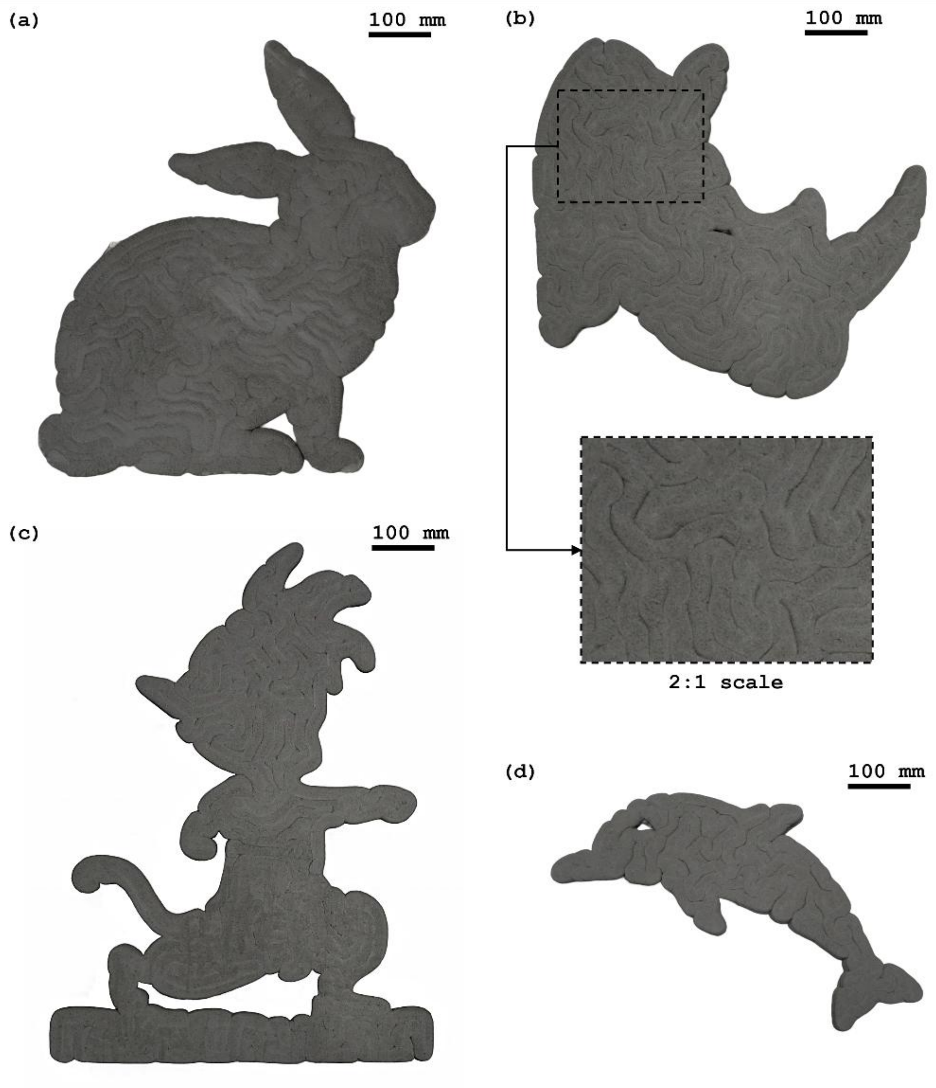

Figure 4.24 Concrete 3D printed geometries: (a) Rabbit, (b) Rhino, (c) Anime Character, and (d) Dolphin

The challenge of serrated or jagged boundaries in printed structures can be efficiently handled using a contour offset approach mentioned in Figure 4.2, which smoothens the outer edges by more precisely aligning the toolpath with the required geometry, improving surface quality and dimensional accuracy.

The growth curve-based toolpath ensures precise coverage in thin features, overcoming underfilling limitations of existing methods, by effectively filling even areas where only one pass can be made, improving the overall print quality and structural integrity. In this case, the position of the user-defined input curve (yellow in *Figure 4.25*) is critical. The user has to provide the input curve's position so that the curve passes through all the thin features available within the structure while making a closed loop. *Figure 4.25* shows three examples for a 20 mm step-over: (a) Swiss cheese slice, (b) Voronoi pattern, and (c) Flower pattern with thin features highlighted by shapes with dashed lines. While *Figure 4.25(d)* shows the structure with the Voronoi pattern, fabricated with a 20 mm step-over value.

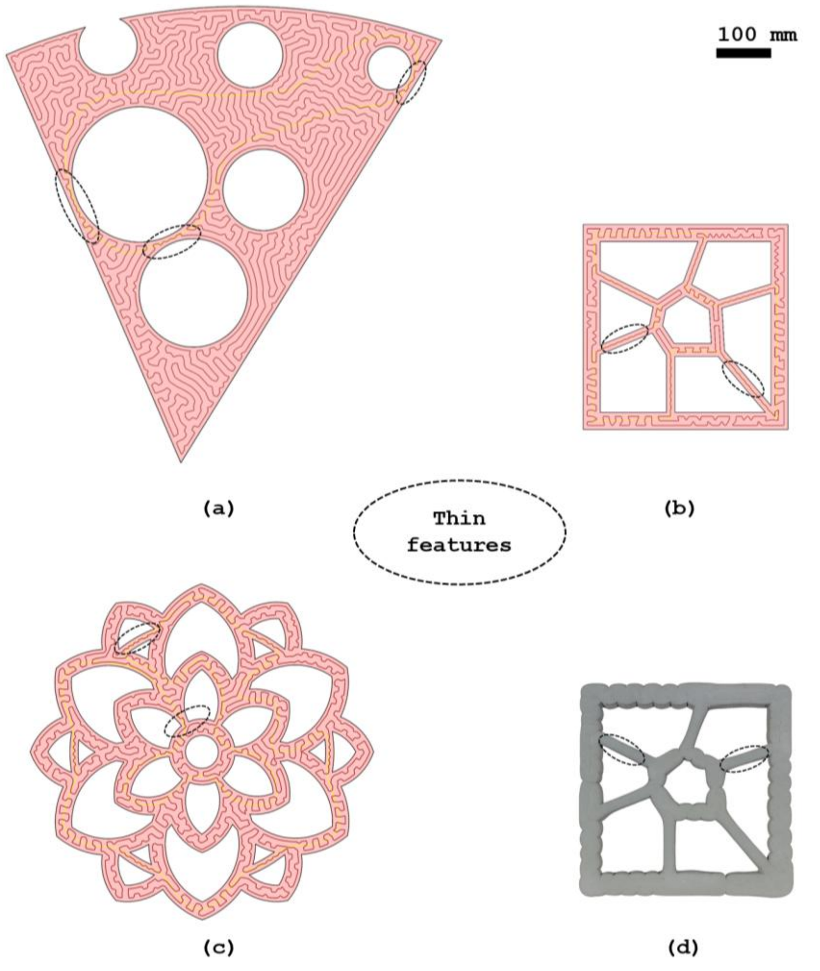

Figure 4.25 Growth curve-based toolpath (20 mm step-over) for structures with thin features: (a) Swiss cheese slice, (b) Voronoi pattern, (c) Flower pattern, and (d) Structure with the Voronoi pattern, fabricated using a 20 mm step-over

The experimental and numerical analyses clearly demonstrate that the growth curve-based continuous toolpath strategy consistently outperforms the two conventional approaches—zigzag and contour-parallel, irrespective of the scale. When compared with the TSP-based toolpath strategy, the growth curve method exhibits comparable performance in terms of printing time and the number of sharp turns. However, it demonstrates superior performance in both print quality and computation time, establishing its advantage as a more efficient and precise toolpath generation technique.

An additional strength of the growth curve-based continuous toolpath strategy lies in its ability to adjust part infill density effectively. The infill pattern adheres to the same underlying principles as the primary toolpath and is typically complemented by solid top and bottom layers to preserve surface integrity. Here, the target area 'A_T' for deposition can be selected according to the user-specified infill density (d_i). Based on this density value, a new segment length is calculated as '$((^{s}/_{2})/d_i)'$, which establishes the necessary number of segments 'N_d'. The length of this segment is directly proportional to the designated infill density. *Figure 4.26* illustrates the Dolphin geometry fabricated with varying infill densities of 25%, 50%, 75%, and 100%, generated using a 15 mm step-over. These variations demonstrate the flexibility of the growth curve-based toolpath strategy in achieving controlled infill patterns, enabling efficient material utilization while maintaining geometric fidelity.

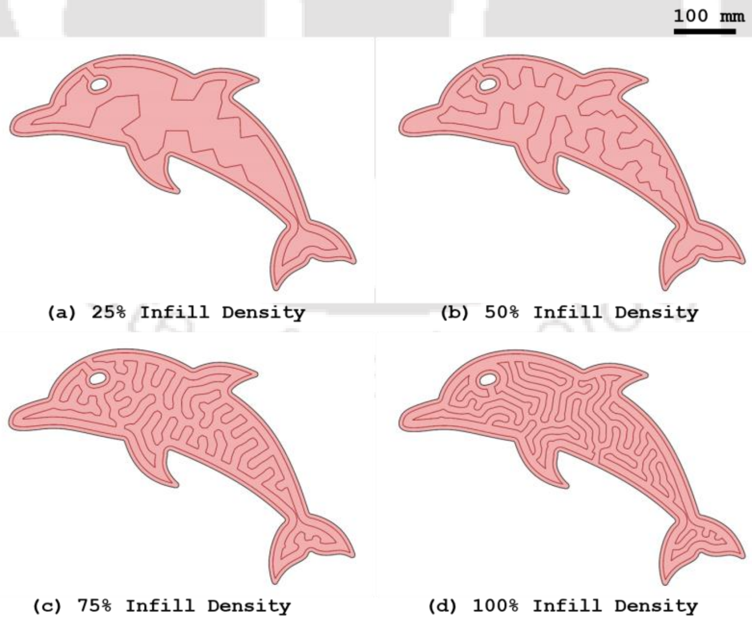

Figure 4.26 Growth curve-based toolpath for different infill densities (a) 25%, (b) 50%, (c) 75%, and (d) 100%

The user-defined input curve plays a critical role in the proposed growth curve–based toolpath planning. To enable uniform propagation of the growth curve across the target area, the input curve must pass through all geometric segments and form a closed loop. Geometries containing thin internal channels smaller than the nozzle diameter cannot be processed, as the input curve cannot enter these confined regions to generate a continuous toolpath. In areas where the available spacing is smaller than the prescribed stepover, the method may produce overlapping toolpaths, as observed in the anime character's tail at higher step-over values *(Figure 4.17(e))* and in the dolphin's narrow tail region when the boundary offset is used *(Figure 4.26)*. The method also requires the input curve to pass through all thin-feature segments and to form a closed loop, as illustrated in *Figure 4.25*. Furthermore, for geometries containing thin features, the approach is not fully automatic, as the user must carefully define the input curve to satisfy all input-curve conditions described in the manuscript. In this study, a boundary-offset input curve is adopted to reduce variability and ensure consistency for solid infill applications

4.6. Summary

Compared to the TSP-based approach, the growth curve method results in similar printing time, toolpath continuity, and computation time at smaller scales while achieving better print quality with underfilling <0.015 and overlapping <0.03. On a larger scale, the growth curve-based strategy outperforms both the conventional methods in terms of printing time, toolpath continuity, computation time, and print quality, while performing neck to neck with the TSP-based toolpath strategy in terms of printing time and toolpath continuity, and outperforms it regarding print quality and computation time at a large scale. Analytical and experimental validation across numerous geometries demonstrates the method's scalability, robustness, and adaptability. The strategy achieves optimized toolpath by carefully adjusting important parameters, particularly step-over and growth factor, which reduce printing time, minimize sharp turns, eliminate unnecessary interruptions, improve print quality, and computation efficiency.

The growth curve-based toolpath strategy provides a scalable, computation-efficient, and high-quality continuous path planning solution for AMoC, achieving optimal performance at a 20 mm step-over and growth factor of 2, with very low underfilling (<0.015) and overlapping (<0.03), while maintaining competitive printing time and continuity across scales. This establishes the method as a strong alternative to both conventional and TSP-based strategies for large-scale, complex, and architecturally relevant concrete printing applications.

Chapter 5: Investigation into a Non-Planar Growth Curve-based Toolpath Strategy

This chapter extends the growth curve-based method to non-planar area filling. It investigates the feasibility of generating continuous deposition toolpath on arbitrary non-planar meshes, thereby enabling the fabrication of complex surfaces beyond conventional layer-by-layer deposition. The proposed strategy lays the groundwork for non-planar AMoC applications using robotic systems.

A portion of this chapter has been submitted.

Sahu, A., Panda, B., & Ror, C.K. (2026). Utilization of a growth curve-based strategy for generating non-retractable and non-planar toolpath for additive manufacturing of concrete. *CIRP Journal of Manufacturing Science and Technology.* **(Submitted)**

5.1. Abstract

This study investigates the feasibility of a growth curve–based toolpath strategy for non-planar AMoC. Conventional concrete printing on flat build platforms often results in toolpath discontinuities and limited design freedom, restricting the fabrication of geometrically complex curved components. To overcome these limitations, a non-planar printing approach is proposed in which material deposition is performed on curved sand–sodium silicate support beds, enabling the toolpath to directly conform to concave, convex, and doubly curved surfaces. The proposed methodology integrates growth curve–based toolpath planning with recyclable sand supports to generate continuous and collision-free deposition paths, ensuring uniform material extrusion while maintaining dimensional fidelity to the corresponding CAD geometry. This study focusses on architectural elements where surface smoothness and dimensional correctness are essential for assembly and aesthetic appeal. For smooth fitting and structural stability, applications like modular structural elements and interconnecting non-planar facades require exact geometric conformance. This work attempts to achieve high-accuracy surface deposition, minimize geometric deviations, and provide dependable manufacture of complicated architectural shapes by utilizing the growth curve-based non-planar printing technique. This work establishes a practical pathway for advancing non-planar concrete printing toward complex curved components with improved accuracy and design flexibility.

5.2. Methodology

The suggested methodology for non-planar AMoC combines computerized process planning with experimental sand-bed-supported fabrication, as shown in *Figure 5.1*. The method begins by creating a non-planar CAD model of the target part and the supporting bed *Figure 5.1*. From here, the process splits into two complementary streams. The first stream *Figure 5.1* uses the part's non-planar CAD model *Figure 5.1* to extract a non-planar surface *Figure 5.1*, which is subsequently transformed into a mesh *Figure 5.1*. On this non-planar mesh, a growth-curve-based continuous toolpath is generated *Figure 5.1*, which is then post-processed and translated into G-codes for printing.

In parallel, the second stream *Figure 5.1* creates the non-planar sand support bed. A digital model of the bed surface *Figure 5.1* is made; this surface is utilized to construct a non-planar raster toolpath *Figure 5.1*, and the bed profile is physically realized using a sand-shaper tool *Figure 5.1*. The bed is made of sodium-silicate-mixed and compacted sand, which is then cured and hardened into a non-planar sand support surface *Figure 5.1*. Finally, both streams converge at *Figure 5.1*, where the cementitious material mix is deposited over the constructed sand bed using the growth-curve toolpath to create the non-planar concrete component. This integrated technique shows how computational path planning and sand-bed manufacturing may work together to provide continuous, collision-free concrete deposition on non-planar sand surfaces.

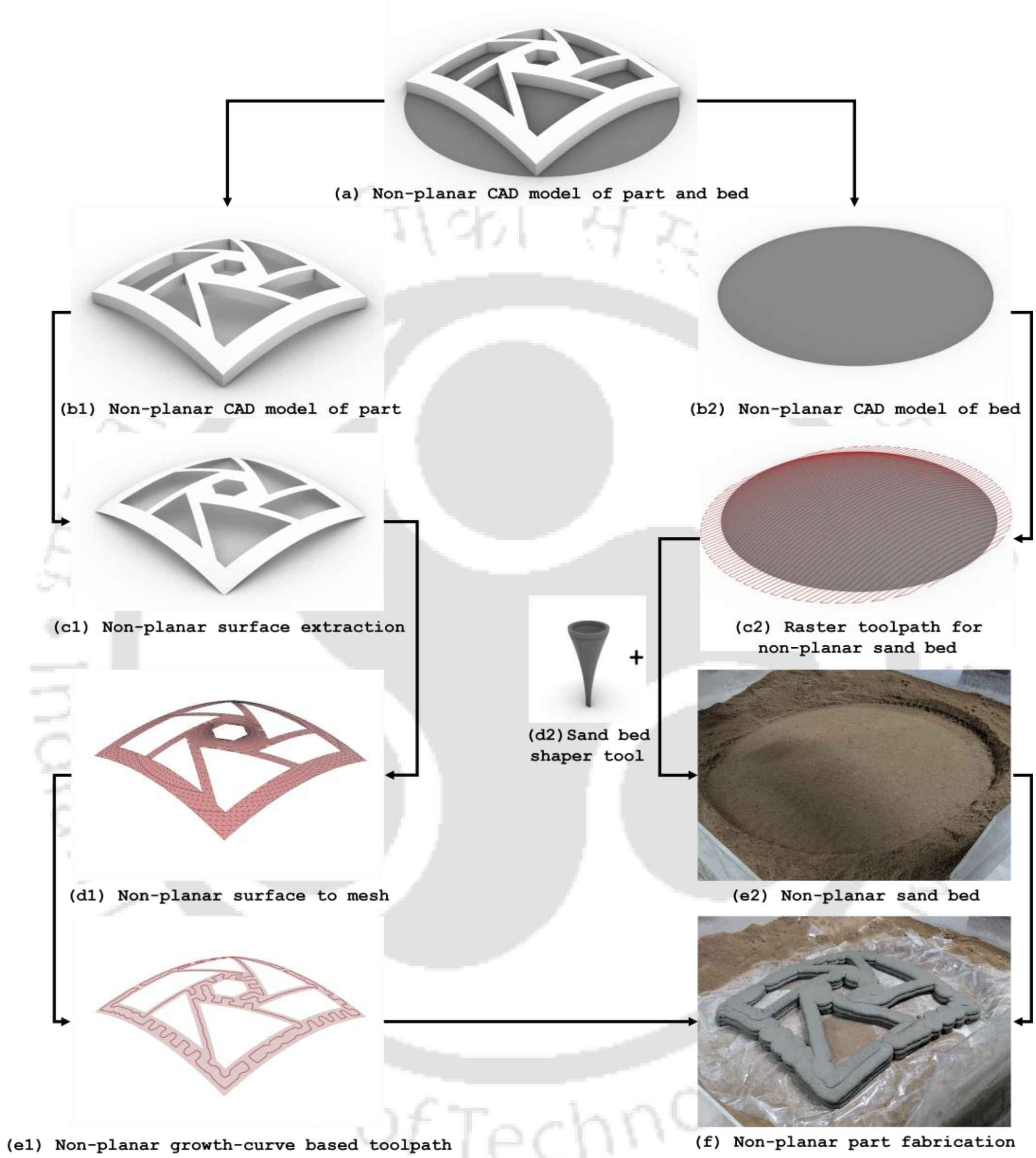

Figure 5.1 Process flow of non-planar growth curve –based toolpath generation

5.2.1. Sand bed fabrication

In this investigation, a non-planar sand-based support was employed to construct the print bed, consisting of fine river sand, sodium silicate, and water in a ratio of 100:6:2. The mixture was compacted and shaped with a sand-shaper tool (*Figure 5.1(d2)*) guided by a non-planar raster toolpath (*Figure 5.2*, top row), the sand is compacted and shaped within a 5 mm thick acrylic container measuring 800 mm × 800 mm × 300 mm. The sand bed can be cured instantly with

CO_2 gas or left to harden naturally with ambient exposure. When utilizing the same sand for a second or third time for bed fabrication under atmospheric curing, the sodium silicate and water ratio was modified to 100:2:6 to retain enough binding while assuring recyclability. A gantry-based concrete printer was used to create a variety of non-planar sand beds, including cylindrical concave, cylindrical convex, and completely convex geometries, as shown in *Figure 5.2*, bottom row, resulting in versatile support profiles for subsequent concrete depositions. Despite having a little staircase effect owing to raster shaping, the sand bed was recyclable, easily accessible, and suited for recurrent non-planar bed fabrication, making it the chosen choice in this study.

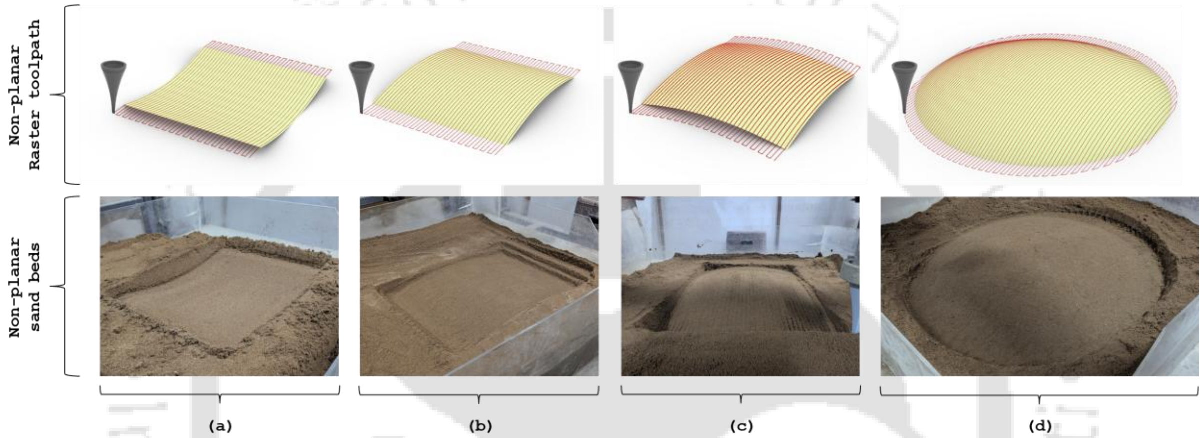

Figure 5.2 Non-planar raster toolpath (top row) and fabricated sand bed (bottom row); (a) Cylindrical concave, (b) Cylindrical convex, and (c) & (d) Convex

5.2.2. Toolpath generation

The growth curve-based toolpath generation method is similar to the one described in the preceding chapter, but with some adjustments to address the issues of non-planar deposition. In this case, the traditional slicing method, which divides the geometry into a stack of parallel planar layers, is unnecessary. Instead, the bottom surface of the part is removed and utilized using B-rep deconstruction, which ensures that the actual contact interface between the printed component and the supporting bed is used to generate toolpaths. This extracted surface is then turned into a non-planar mesh, which serves as the target area for the growth curve to propagate across. Using this method, the resulting toolpath automatically adapts to the curved shape of the supporting surface, removing the need for complicated intermediary slicing processes.

Another essential modification is replacing the circle-collision operation in the planar case with a sphere-collision operation for non-planar cases. This assures that the toolpath is equidistant from itself in three dimensions, resulting in consistent filament spacing even on curved or doubly curved surfaces. Such an adaptability is critical for preventing underfilling and overlapping in non-planar printing, where variations in curvature might otherwise result in uneven material deposition. Following these alterations, the remaining steps—conditional checks for area filling, and path optimization—are carried out the same way as in the planar workflow. These modifications enable the growth curve-based strategy to be applied smoothly to non-planar geometries, resulting in a continuous, collision-free toolpath that increases the quality and reliability of non-planar AMoC. *Figure 5.3* (top row) shows the CAD model of non-planar parts, and *Figure 5.3* (bottom row) shows the non-planar growth curve-based toolpath for the same parts.

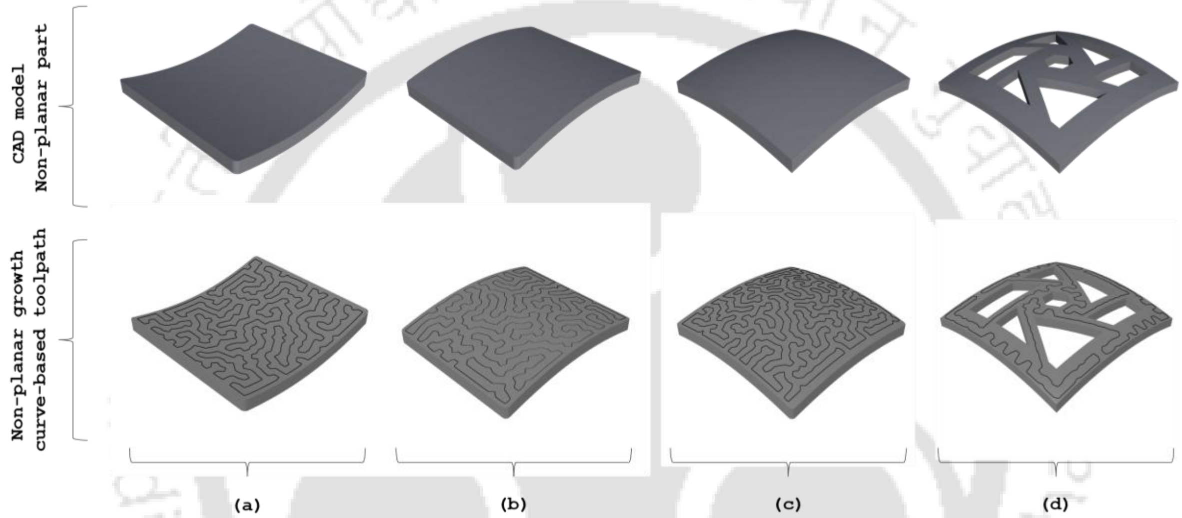

Figure 5.3 CAD model of non-planar parts (top row) and non-planar growth curve-based toolpath (bottom row); (a) Cylindrical concave, (b) Cylindrical convex, (c) Convex, and (d) Thin-featured convex

Figure 5.4 depicts the non-planar toolpath used to create an artificial brain coral reef structure from cementitious material. The customized toolpath begins with the growth curve-based toolpath, which fills the entire area of the defined circular convex region for the first two layers, shown in black. From the third layer, the toolpath is modified to reach a 50% infill density for the following two or three layers, as shown in blue, resulting in the distinctive brain coral reef-like texture on top of the fully dense non-planar base. *Figure 5.4(a)* exhibits the created artificial brain coral reef, whereas *Figure 5.4(b)* shows a version of the same structure with three integrated cavities.

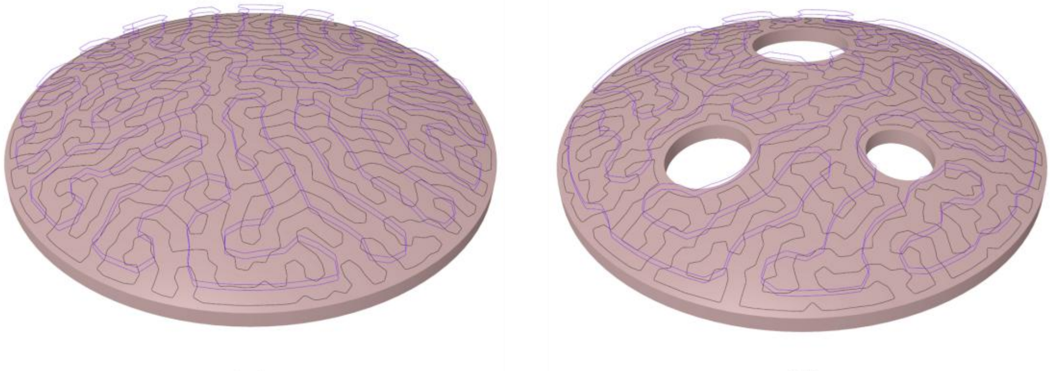

Figure 5.4 Non-planar growth curve-based toolpath for (a) Artificial brain coral reef structure, and (b) Artificial brain coral reef structure with three cavities.

5.3. Experimental validation and analysis

This section presents the experimental validation of the proposed non-planar toolpath methodology. Following the fabrication of non-planar sand beds with different non-planar profiles, corresponding concrete parts were produced using a gantry 3D printer and 3D mortar material mix presented in Section 2.2. These digital designs were subsequently realized through the non-planar growth curve-based toolpath executed over the prepared sand beds, resulting in the physical parts. *Figure 5.5(a)*, *Figure 5.5(b)*, and *Figure 5.5(c)* show how a single non-planar sand bed is used to create separate pieces, especially cylindrical concave, cylindrical convex, and convex-shaped facade components. *Figure 5.5(d)* shows that a single sand bed can be utilized to fabricate numerous non-planar parts, including a convex thin-feature facade structure *(Figure 5.5(d1),* an artificial brain coral reef *(Figure 5.5(d2))*, and an artificial brain coral reef with cavities *(Figure 5.5(d3))*. This indicates that the sand bed keeps its geometry and structural integrity once fully cured throughout multiple prints. The successful fabrication of these components highlights the feasibility of synchronizing growth curve path planning with sand-bed-supported deposition, continuous non-planar AMoC.

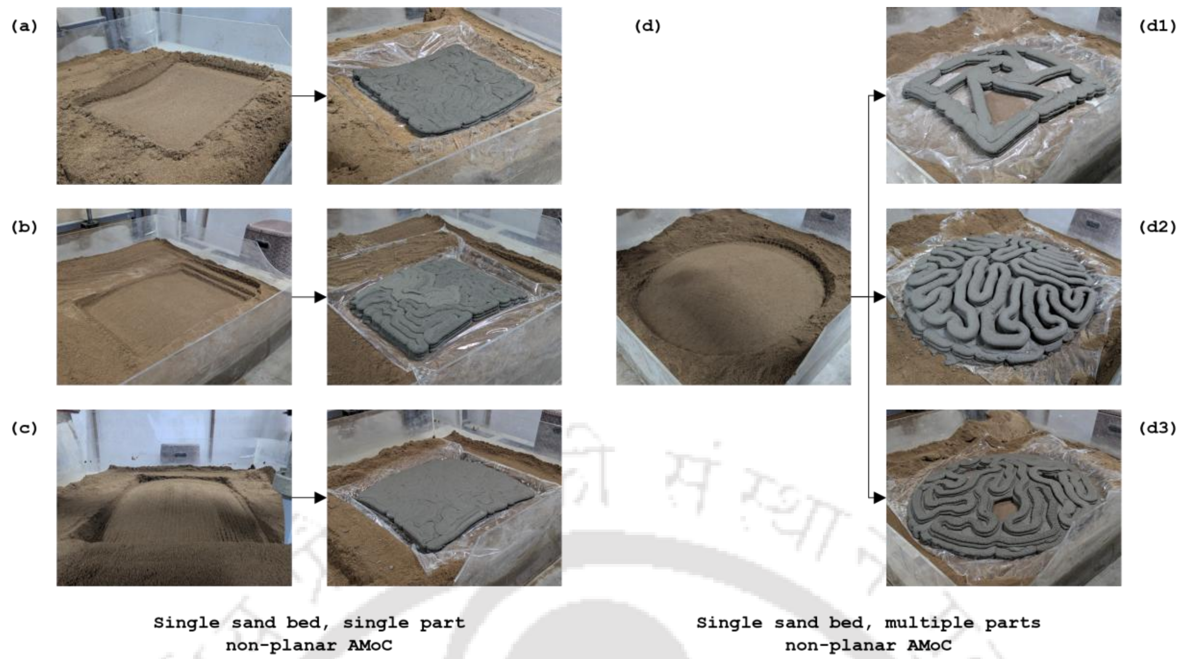

Figure 5.5 Non-planar fabricated parts: (a) Cylindrical concave, (b) Cylindrical convex, (c) Convex, and (d) Multiple convex: (d1)Thin feature structure, (d2) Artificial brain coral reef, and (d3) Artificial brain coral reef with cavities

After the fabrication of the non-planar concrete parts, an analysis of dimensional accuracy was conducted to evaluate the fidelity of the printed geometries. An API portable laser scanner was used to capture high-resolution 3D scans of the fabricated components, as shown in Figure 5.6. The scanned data was then processed and aligned with the corresponding CAD models using open-source software, enabling a direct comparison between the designed and fabricated geometries. This approach provided a quantitative assessment of geometric deviations and surface conformity, serving as a validation step for the proposed non-planar toolpath methodology.

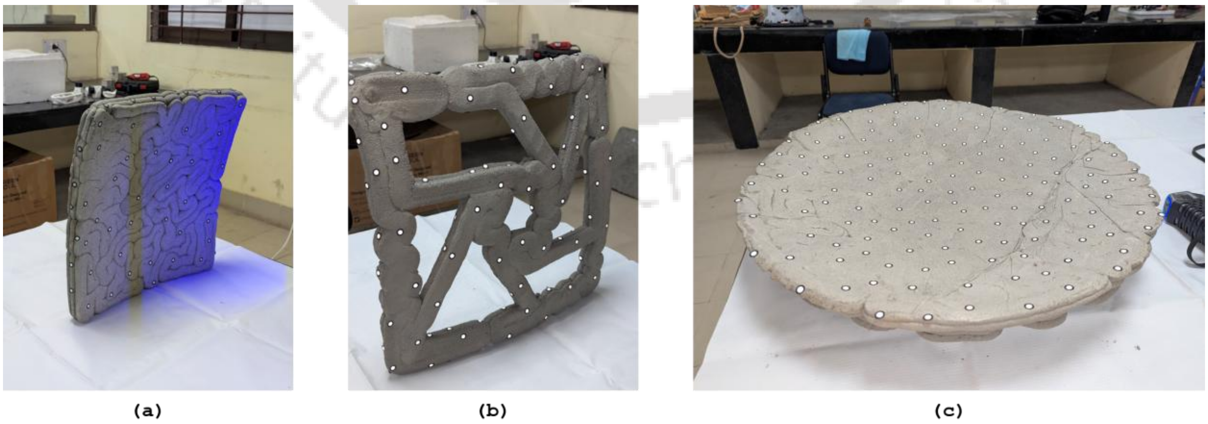

Figure 5.6 Laser scanning of the fabricated non-planar parts: (a) Convex, (b) Thin feature structure, and (c) Base of the artificial brain coral.

5.3.1. Sand bed analysis

The bottom portion of the artificial brain coral reef base was selected for the investigation to evaluate the accuracy of the constructed non-planar sand bed compared to the CAD model. This section was scanned using the API portable laser scanner, and the generated point cloud was aligned with the CAD surface of the non-planar base. The comparison allowed for an assessment of how closely the sand bed conformed to the planned shape, providing information on the raster shaping process's success and the sodium-silicate-treated sand's curing stability. The comparison findings are as follows; The Gaussian distribution of deviations between the convex surface CAD model and the fabricated sand bed scan indicates a small negative mean shift (≈ –0.43 mm) with a standard deviation of ≈ 0.77 mm, suggesting that while the fabricated surface largely follows the CAD geometry, there is a consistent slight inward deviation and moderate variability across the surface as shown in *Figure 5.7.*

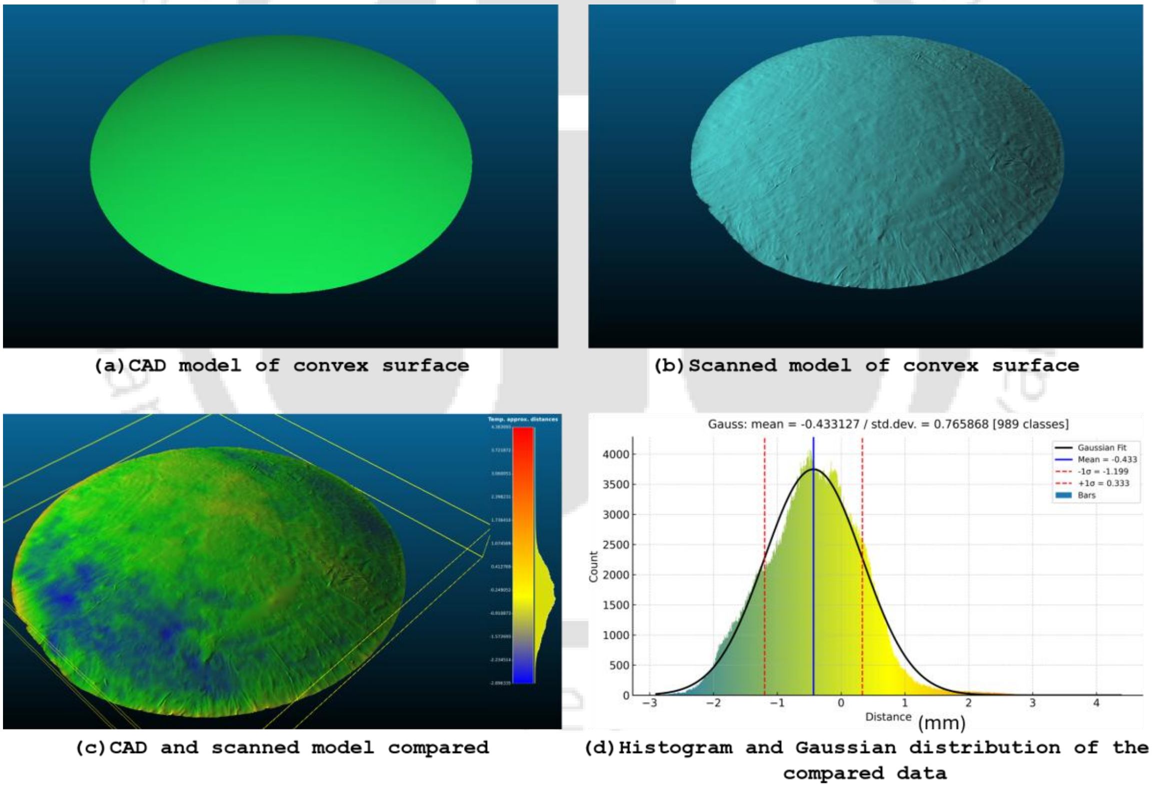

Figure 5.7 Geometric deviation analysis of the convex surface CAD model and the fabricated sand bed surface by utilizing the lower surface of the fabricated artificial brain coral reef structure

5.3.2. Fabricated part analysis

To assess the dimensional deviation of the fabricated parts in relation to their CAD models, two 3D printed parts, a convex portion and a thin-featured structure, were scanned, and the dimensional accuracy was analyzed. The comparison of CAD and 3D printed convex parts revealed both positive and negative deviations. The non-planar convex geometry recorded a positive mean deviation of approximately 0.65 mm with a standard deviation of about 1.01 mm, indicating that most regions lie slightly above the design surface. However, localized underfilling (down to -6 mm) was observed due to irregularities in deposition, as shown in *Figure 5.8*.

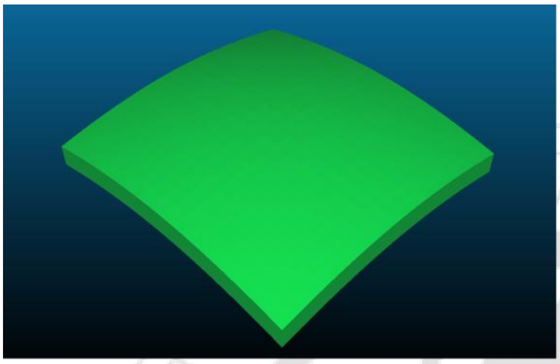

(a) CAD model of convex part

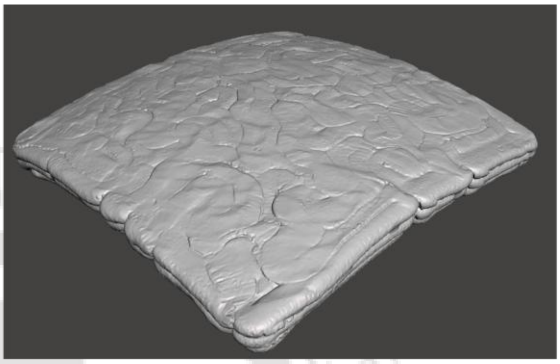

(b) Scanned model of convex part

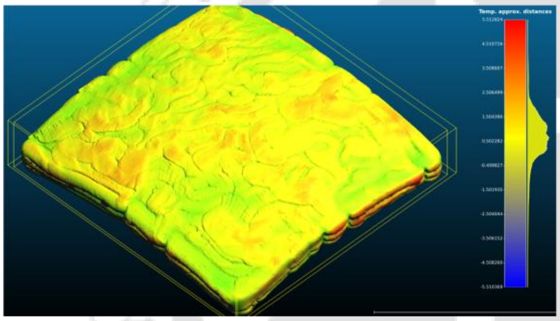

(c) CAD and scanned model compared

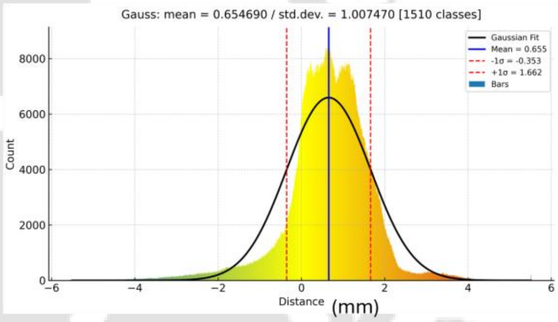

(d) Histogram and Gaussian distribution of the compared data

Figure 5.8 Geometric deviation analysis of a convex CAD model and a concrete 3D printed convex part

The thin-featured structure had a negative mean deviation of around -0.30 mm and a higher standard deviation of around 1.75 mm, indicating that the fabricated geometry often lies below the CAD reference and displays greater variability due to deposition challenges in gantry-based systems. The observed deviation range of ±6 mm is within acceptable tolerance limits for 3DCP, indicating the practicality of the suggested technique. Nonetheless, our findings suggest that using robotic arm-based non-planar printing technologies might result in even higher accuracy as shown in *Figure 5.9*.

(a) CAD model of thin feature structure

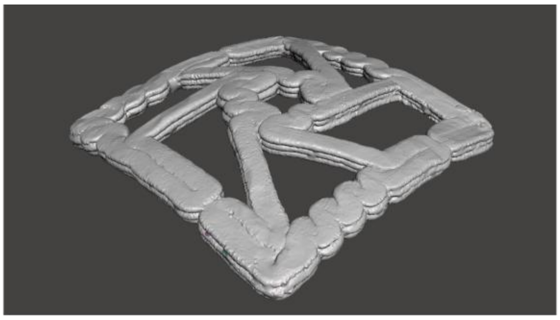

(b) Scanned model of thin feature structure

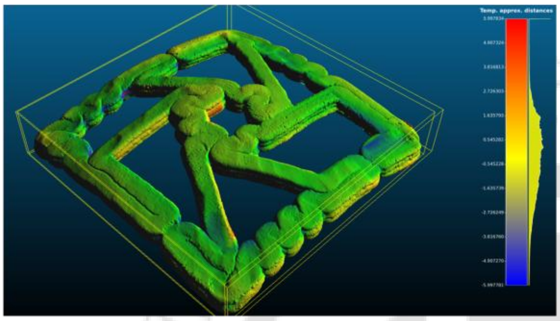

(c) CAD and scanned model compared

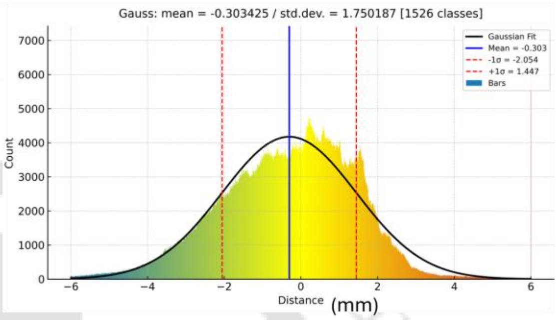

(d) Histogram and Gaussian distribution of the compared data

Figure 5.9 Geometric deviation analysis of a thin feature CAD model and a concrete 3D printed thin feature structure

5.4. Summary

The growth curve-based toolpath strategy has been validated for fabricating non-planar structures on sand–sodium silicate beds with reliable dimensional accuracy. The recyclable and easily shaped sand beds effectively replicated the intended non-planar surfaces, offering a practical and sustainable platform that can be reused multiple times for non-planar fabrication. Furthermore, the concrete 3D printed non-planar parts exhibited consistent dimensional accuracy, remaining within ±6 mm of their CAD models.

By combining growth curve-based non-planar toolpath planning with reusable sand–sodium silicate support beds, this study achieves high geometric fidelity (±3 mm for supports, ±6 mm for printed parts) and establishes a sustainable, accurate, and scalable workflow for non-planar AMoC, enabling the fabrication of complex curved architectural components without permanent formwork.

Chapter 6: Conclusions and Scope of Future Work

This chapter summarizes the research findings, contributions, and limitations of the developed frameworks and strategies. It also outlines future research directions.

6.1. Conclusions

Conclusions for all the chapters are as follows:

6.1.1. Design for Additive Manufacturing of Concrete (DfAMoC) Framework

DfAMoC is a novel, structured design framework developed to address challenges related to overhang constraints, material limitations, and printer capacity in additive manufacturing of concrete. The framework enables optimized part orientation, strategic modularization, and the fabrication of large-scale, complex geometries.

The proposed approach was successfully validated on planar, non-planar, and embossed/debossed surfaces. Overhang control allows the fabrication of functional surfaces without support structures by enforcing height-dependent critical angle constraints.

The ACAP-based toolpath planning reduces nozzle lift operations and idle time, while simultaneously enhancing interlayer bonding quality. Dimensional accuracy was preserved, with geometric deviations limited to within ±6 mm relative to the CAD models. Mechanical performance was demonstrated through splitting tensile strength values ranging from 1.42 to 1.52 MPa.

6.1.2. Investigation into a TSP-based Toolpath Strategy for Area Filling

The TSP-based strategy is a continuous toolpath planning workflow developed for solid (space-filling) additive manufacturing of concrete designs.

Operational efficiency was achieved by minimizing print-head travel distance, resulting in a substantial reduction in total printing time.

Print quality enhancement was demonstrated through smoother trajectories, fewer abrupt direction changes, and reduced strength anisotropy compared with conventional toolpath strategies. Material efficiency was improved by integrating the TSP-based workflow with topology-optimized designs, thereby reducing concrete consumption and associated costs.

Scalability of the approach was validated across a range of geometric complexities; the use of large nozzle diameters ensures that TSP computations remain feasible on standard computing platforms. The key limitations include exponentially increasing computational time with higher point densities due to the NP-hard nature of the TSP, as well as additional post-processing requirements to smooth sharp turns in the generated toolpaths.

6.1.3. Development of a Growth Curve-based Toolpath Strategy for Area Filling

The growth curve strategy is a continuous toolpath generation method developed for solid geometries, thin-walled features, and structures with spatially varying infill densities. Operational advantages include minimized underfilling (< 0.015) and overlap (< 0.03), along with a reduction in sharp turns and printing interruptions. Optimal process parameters were established through a parametric investigation, identifying a 20 mm step-over and a growth factor of 2 as optimal for linear growth functions.

Comparative evaluation against zigzag and contour-parallel strategies demonstrates superior performance in printing time, toolpath continuity, and surface quality across multiple geometric scales. Benchmarking against the TSP-based strategy indicates comparable performance in terms of printing time and continuity, while delivering improved print quality and significantly reduced computational cost at larger scales.

The growth curve-based toolpath exhibits the lowest mechanical anisotropy, achieving reductions of 56.0% relative to zigzag, 54.6% relative to contour-parallel, and 25.7% relative to TSP-based strategies, establishing it as the most effective approach for anisotropy mitigation in AMoC.

Robustness of the method was confirmed through combined analytical and experimental validation, with no significant limitations observed when compared with existing continuous toolpath strategies.

6.1.4. Investigation into a Non-Planar Growth Curve-based Toolpath Strategy

Non-planar validation of additive manufacturing of concrete was successfully demonstrated the applicability of growth curve-based toolpaths while fabricating complex concrete geometries on non-planar support beds.

Sustainable support systems were realized using sand–sodium silicate beds, which are recyclable, easily shapeable, and reusable over multiple cycles without loss of geometric accuracy. Support-bed accuracy was experimentally verified, with sand-bed dimensional deviations limited to within ±3 mm of the corresponding CAD surfaces.

Printed component accuracy confirmed that the fabricated concrete elements matched the digital models within a ±6 mm deviation, satisfying industry tolerances for large-scale 3D concrete printing. Geometric fidelity results indicate that the integration of growth curve-based toolpath planning with reusable non-planar sand support provides a robust and high-precision solution for non-planar additive manufacturing of concrete. *Figure 6.1* Schematic illustration summarizing the overall conclusions of the study.

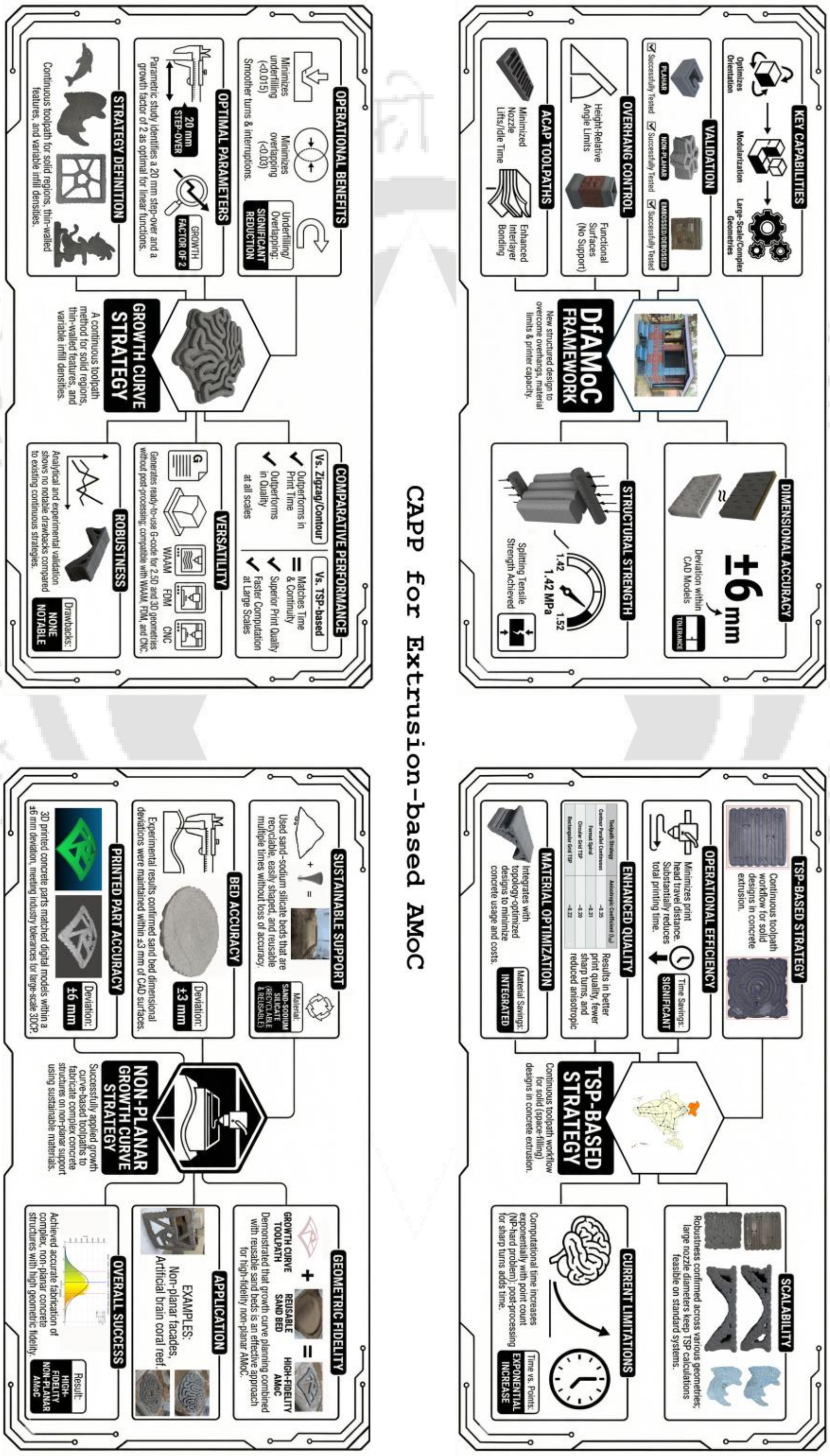

Figure 6.1 Schematic illustration summarizing the overall conclusions of the study

6.2. Future scope and recommendations

- **Integration of DfAMoC with parametric design environments**

Future work can focus on embedding the DfAMoC framework within parametric modelling platforms to directly link design and process planning. By incorporating process-specific constraints such as nozzle diameter, layer height, and extrusion rate during geometry creation, real-time printability assessment can be achieved. This integration would significantly reduce manual iterations and enable automated generation of AMoC-compliant designs. Platforms such as Rhino–Grasshopper can further support visualization of layer-wise deposition and enhance structural continuity during the design phase.

- **Directional strength enhancement through TSP-based toolpath alignment**

The TSP-based continuous toolpath strategy can be extended to align material deposition with principal load paths to improve directional mechanical performance. By embedding structural orientation and load-transfer mechanisms into toolpath planning, interlayer bonding can be enhanced and weak planes minimized. This approach enables functionally graded material behavior through path optimization rather than material variation. Such a strategy is particularly promising for beams, shells, and curved concrete elements subjected to non-uniform loading.

- **Bioinspired interior architectures using growth-curve-based generative design**

The growth-curve approach can be further developed as a generative design tool to create regulated, bioinspired internal architecture. By locally varying the growth-curve spacing, porous networks resembling coral or bone structures can be fabricated with controlled cavity sizes and distributions. These geometries offer potential improvements in material efficiency, load distribution, and functional performance. Applications include artificial coral reefs, lightweight architectural components, and environmentally responsive structures.

- **Non-planar growth-curve printing for large-scale facade and modular components**

Future research can extend non-planar growth-curve printing to fabricate modular facade panels with continuous surface finishes and enhanced structural integrity. Deposition along curved toolpaths can reduce the stair-step effect and minimize the need for support structures. This approach enables the integration of shading, ventilation, and aesthetic features directly into the printed geometry. Scaling this strategy for 3D concrete printing could support efficient production of architecturally complex, high-performance building envelopes.

Appendix

A1. Development of a DfAMoC framework

A1.1. Different geometries in AMoC and problems with commercial slicing packages

In the context of AMoC, addressing three distinct geometries that demand consideration is noteworthy. These geometries encompass planar geometry (2.5D), non-planar geometry (3D), and non-planar geometry with embossing or debossing features 3D) (all three geometries shown in Figure A1.1). Implementing a continuous toolpath is essential in AMoC because it facilitates materials' uniform and durable deposition, creating a resilient and enduring structure. The structural integrity of the material deposition may be compromised due to the presence of gaps or irregularities resulting from a discontinuous toolpath when the aforementioned solid CAD model of the geometry is processed using FDM-based tools like Simplify3D and Ultimaker Cura. Table A1.1 describes these geometries and details the error when these geometries are processed using an FDM-based slicer such as Simplify3D and Ultimaker Cura (shown in Figure A1.2 in green and red, respectively).

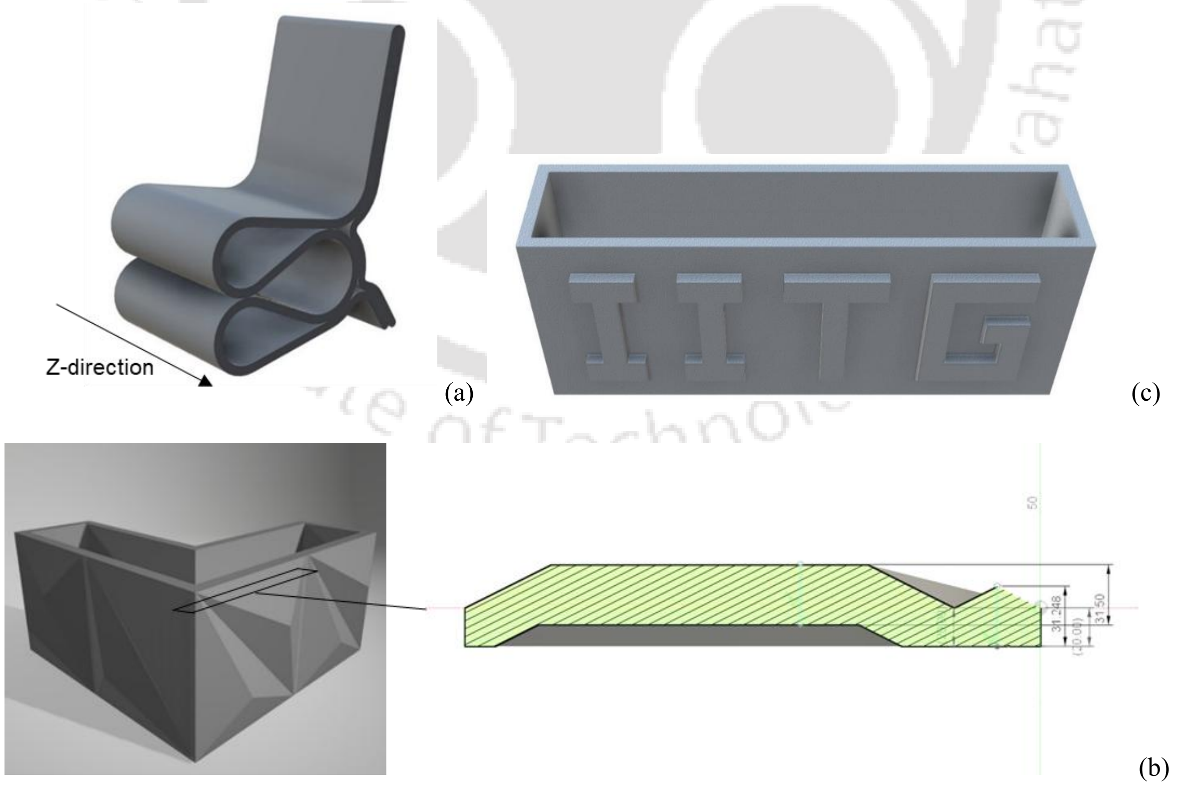

Figure A1.1 CAD model of (a) Planar geometry (2.5D), (b) Non-planar geometry (3D), and (c) Non-planar geometry with embossing and debossing features (3D)

Table A1.1 Geometry types and Error details

Description	Error Details	
Planar geometry (2.5D)		
Sequentially layered 2D components to form quasi-3D items. Lack of full 3D intricacy. Figure A1.1(a)	- Discontinuous toolpath - Patch deposition - Insufficient material deposition	Figure A1.2(a)
Non-planar geometry (3D)		
Fully 3D structures with inclined features result in non-uniform thicknesses in horizontal layers. Figure A1.1(b)	- Inaccuracies in G-codes due to uneven dimensions in the XY plane - Excessive deposition at greater widths - Inconsistent deposition width and discontinuous deposition within the same layer - Vibrations and structural failures in constructions over 800 mm in height	Figure A1.2(b)
Non-planar geometry with embossing and debossing features (3D)		
Raised or protruding features like embossed/debossed text or the Brand's logo. Figure A1.1(c)	- Unsupported deposition - Discontinuous deposition due to the absence of support structures in AMoC - Structural failure due to vibrations from discontinuities in the path for components with a height of around 800 mm	Figure A1.2(c)

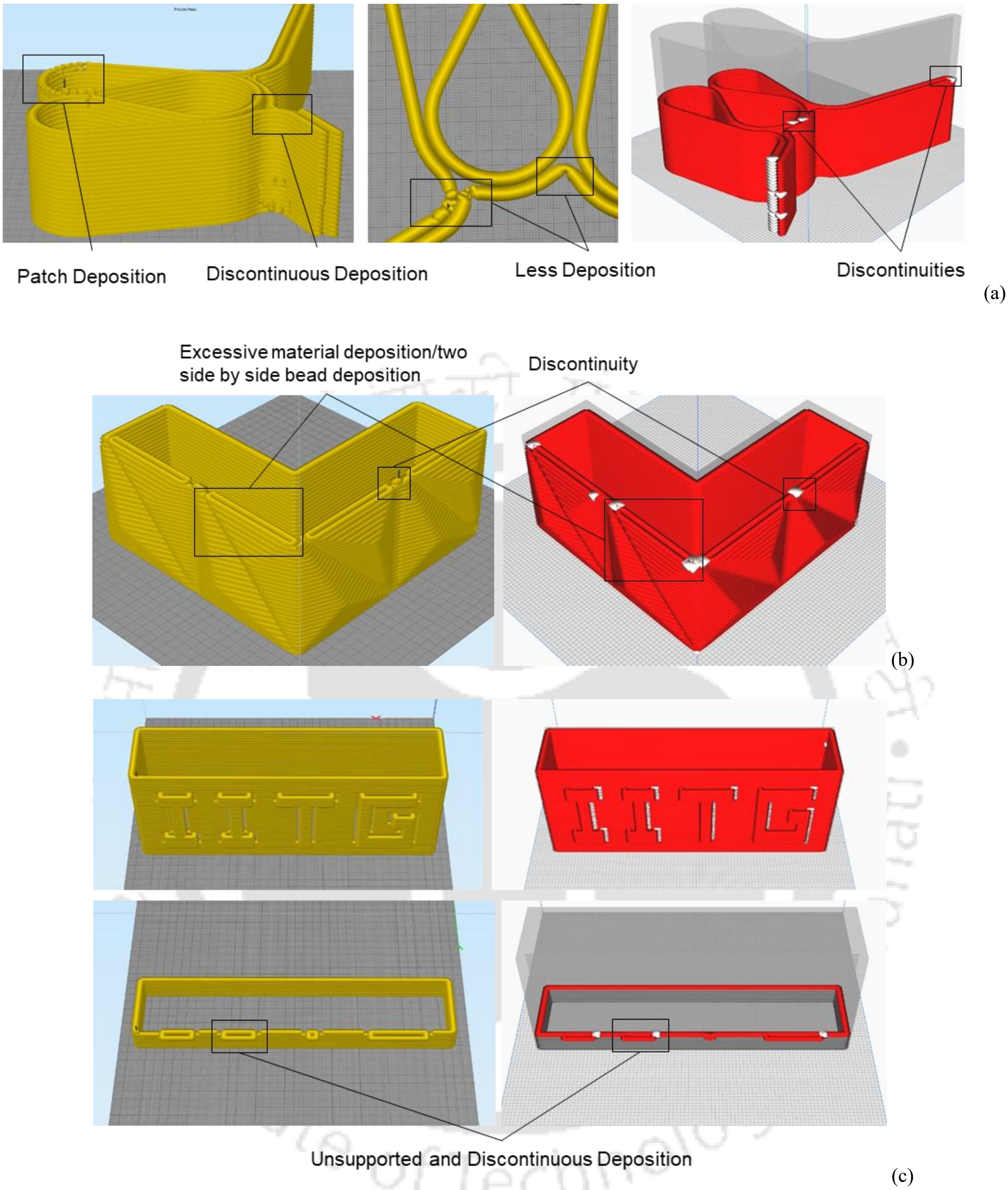

Figure A1.2 Error details when geometries are processed using an FDM-based slicer, Simplify3D (green) and Ultimaker Cura (red). (a) Planar geometry, (b)Non-planar geometry (3D), and (c) Non-planar geometry with embossing and debossing features (3D)

These problems occur because the produced toolpath has been optimized for the FDM process, where a continuous toolpath is less critical owing to variables like material properties, layer adhesion, and the reduced chance of nozzle obstruction. Nonetheless, in the AMoC method, these difficulties pose considerable hurdles during the printing phase. Discontinuous toolpaths, inconsistent deposition, and inconsistent material flow result in nozzle blockage, interrupting the AMoC process.

A1.2. Dimensional accuracy measurement of additively manufactured concrete structures

Figure A1.3(a) shows the CAD model of a brick-patterned wall element with specific dimensions, whereas Figure A1.3(b) shows the corresponding surface model created using the DfAMoC method. Figure A1.3(c) shows the printed result, with the final dimensions highlighted. The measured dimensional variations varied within ±6 mm, demonstrating that, when correctly executed, the proposed methodology can produce geometrically accurate components.

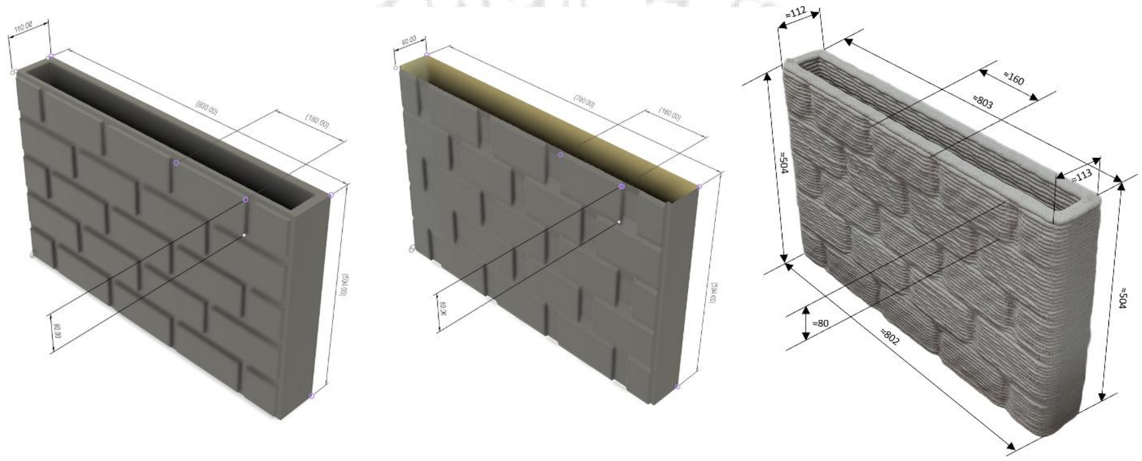

(a) (b) (c)

Figure A1.3 (a) CAD model of a brick-patterned wall element, (b) Surface model created using the DfAMoC method, and (c) Printed brick-patterned wall element, with the final dimensions

A2. Investigation into a TSP-based toolpath strategy

A2.1 Toolpath Continuity

In this section, we examined the continuity of a TSP toolpath alongside four available toolpath strategies (paintbrush, zigzag, contour parallel, and spiral). These four toolpath strategies are illustrated in Figure A2.1.

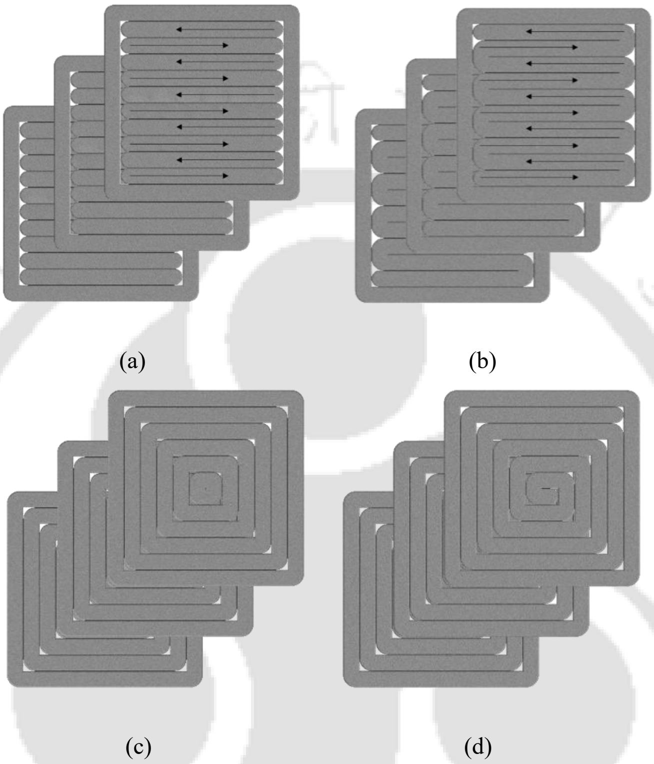

Figure A2.1 Available toolpath strategies in additive manufacturing: (a) paintbrush, (b) zigzag, (c) contour parallel, and (d) spiral

A comparative analysis regarding the number of lifts of the print head is presented in Table A2.1. The numerical result we obtained shows that the TSP toolpath .

Table A2.1 *Comparison of discontinuity present in different toolpath strategies*

Toolpath	TSP toolpath (rectangular or circular grid)	Available AM toolpath strategies			
		Paintbrush	Zigzag	Contour Parallel	Spiral
Square	**1**	20	**1**	9	18
Human face	**1**	47	2	14	52
Rhino face	**1**	64	7	14	48
Arch bridge	**1**	55	6	12	80
Chair	**1**	110	10	28	118

A2.2 TSP toolpath for lattice infill

Initially devised for area filling, the TSP toolpath can be repurposed for lattice infill by simply adjusting the stepover distance 's.' By varying the stepover distance and keeping bead width constant, intricate lattice structures can be achieved within the filled area. This adaptation leverages the inherent efficiency and optimization capabilities of the TSP algorithm to generate lattice infill that offers a balance between structural integrity and material savings. Figure A2.2 illustrates the lattice infill patterns for the rectangular grid (row 1) and circular grid (row 2) corresponding to the TSP toolpath. In Figures A2.2(a) to A2.2(d), the stepover distance varied from 20 mm for complete infill to 30 mm, 40 mm, 50 mm, and 60 mm for lattice infill for the rectangular grid. For these stepovers, the obtained densities are 61%, 55%, 48%, and 38%, respectively. In contrast, Figures A2.2(e) to A2.2(h) showcase the stepover distance varying from 20 mm for complete infill to 30 mm, 40 mm, 50 mm, and 60 mm for lattice infill for the circular grid. For these stepovers, the obtained densities are 66%, 61%, 44%, and 39%, respectively.

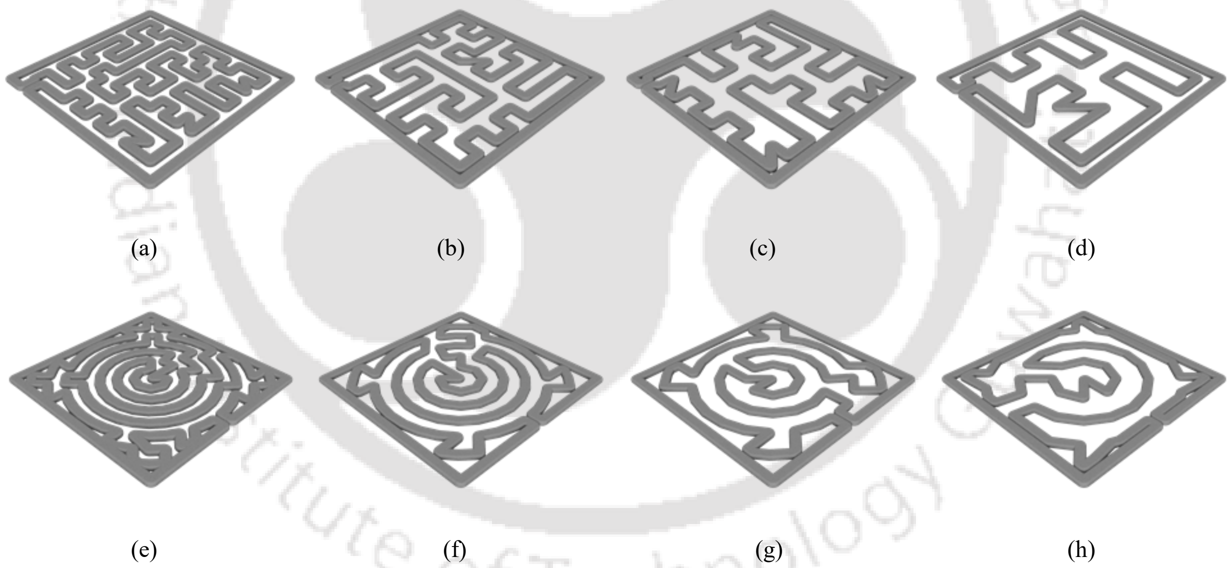

Figure A2.2 TSP toolpath for lattice infill; (a), (b), (c), and (d) for rectangular grid with 30 mm, 40 mm, 50 mm, and 60 mm stepover distances; and (e), (f), (g), and (h) for circular grid with 30 mm, 40 mm, 50 mm, and 60 mm stepover distances

A2.3 Close loop and Interlayer time interval in the TSP-based toolpath

A closed-loop TSP algorithm is a method that produces a continuous toolpath, ensuring the print head starts and stops material deposition at the same point. This closed-loop circuit reduces disruptions throughout the printing process, resulting in more uniform interlayer bond strength without any cold joints, which can affect structural performance.

The interlayer time interval is defined as the time between the deposition of the consecutive layers of material. A regular time interval between layers guarantees that each layer has the same amount of time before the next layer is deposited over it. We have determined the tensile strength of the same specified material at various time intervals. Figure A2.3 illustrates the variation in material properties between two layers resulting from the variation in moisture levels produced by the time interval. The absence of contact at the material interface diminishes the adhesive strength of the substance. Hence, the temporal interval between layers impacts the overall mechanical characteristics of the structure. To address this problem, it is essential to maintain a regular and equal time interval between each layer, resulting in a more reliable and robust connection between the layers.

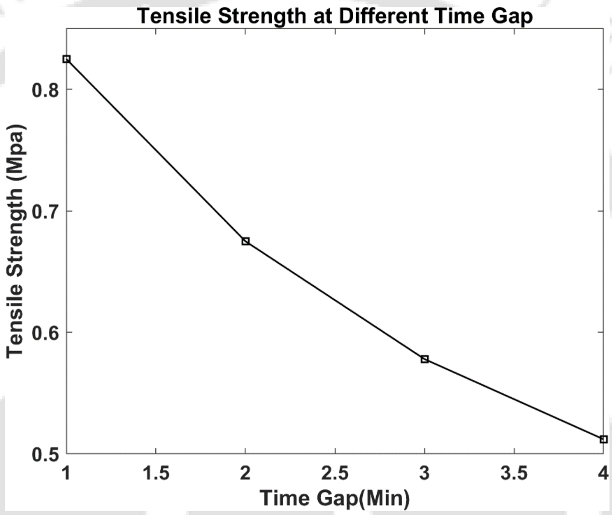

Figure A2.3 Tensile strength at different time intervals

A2.4 Print quality comparison

Two approaches can be compared with noticeable results regarding printed part quality. The rhino model printed using a continuous TSP rectangular grid toolpath (Figure A2.4(a)) is used, exhibiting a consistent and smooth finish. By comparison, the printed geometry exhibits a lot of discontinuities and inconsistencies when the same model is printed with a non-continuous traditional zigzag toolpath (Figure A2.4(b)) under the same printing conditions and material specifications. The part's structural integrity is compromised by the zigzag toolpath's discontinuities, which cause changes in bead width anytime the printer stops and resumes. These findings unequivocally show that a closed-loop TSP toolpath performs noticeably better than the traditional zigzag toolpath, guaranteeing the printed part's higher quality and structural integrity.

(a) (b)

Figure A2.4 3D Printed Rhino using (a) Continuous TSP rectangular grid toolpath and (b) Non-continuous conventional zigzag toolpath.

When using the conventional zigzag toolpath, area filling is insufficient, as seen in Figure A2.5(b), compared to the continuous TSP rectangular grid toolpath (Figure A2.5(a)). In Figure A2.5(b), white patches draw attention to the areas the conventional zigzag toolpath cannot fill.

(a) (b)

Figure A2.5 Demonstration of area filling capabilities of (a) TSP rectangular grid toolpath, (b) Conventional zigzag toolpath

To summarize, employing a closed-loop TSP algorithm improves the structural integrity and quality of 3D-printed concrete objects by ensuring a consistent time interval between each layer. These principles tackle significant problems in AM by guaranteeing uninterrupted material deposition and constant layer-setting times. As a result, concrete constructions become more robust, dependable, and of superior quality.

References

3D Printed Bridge – Barcelona. (2016). Retrieved from https://iaac.net/projects/3d-printed-bridge-development/

Ambily, P. S., Kaliyavaradhan, S. K., & Rajendran, N. (2024). Top challenges to widespread 3D concrete printing (3DCP) adoption–A review. European Journal of Environmental and Civil Engineering, 28(2), 300-328.

Anton, A., Reiter, L., Wangler, T., Frangez, V., Flatt, R.J. and Dillenburger, B. (2021). A 3D concrete printing prefabrication platform for bespoke columns. Automation in Construction, 122, 103467.

Architizer. (2024). Boulder Park, the first 3D concrete printed playground. Retrieved from https://architizer.com/projects/boulder-park-the-first-3d-concrete-printed-playground/

Banihashemi, S., Akbarnezhad, A., Sheikhkhoshkar, M., Bril El Haouzi, H., & Rolfe, B. (2025). 3D printing in construction: sustainable technology for building industry. Progress in Additive Manufacturing, 1-34.

Bi, M., Tran, P., Xia, L., Ma, G., & Xie, Y. M. (2022). Topology optimization for 3D concrete printing with various manufacturing constraints. Additive Manufacturing, 57, 102982.

Bi, M., Xia, L., Tran, P., Li, Z., Wan, Q., Wang, L., Shen, W., Ma, G. and Xie, Y.M. (2022), Continuous contour-zigzag hybrid toolpath for large format additive manufacturing, Additive Manufacturing, Vol. 55, p. 102822.

Blakey-Milner, B., Gradl, P., Snedden, G., Brooks, M., Pitot, J., Lopez, E., ... & Du Plessis, A. (2021). Metal additive manufacturing in aerospace: A review. Materials & Design, 209, 110008.

Breseghello, L., & Naboni, R. (2022). Toolpath-based design for 3D concrete printing of carbon-efficient architectural structures. Additive Manufacturing, 56, 102872.

Breseghello, L., Hajikarimian, H., Jørgensen, H. B., & Naboni, R. (2023). 3DLightBeam+. Design, simulation, and testing of carbon-efficient reinforced 3D concrete printed beams. Engineering Structures, 292, 116511.

Buswell, R., Xu, J., De Becker, D., Dobrzanski, J., Provis, J., Kolawole, J. T., & Kinnell, P. (2022). Geometric quality assurance for 3D concrete printing and hybrid construction manufacturing using a standardised test part for benchmarking capability. Cement and Concrete Research, 156, 106773.

Buswell, R. A., Da Silva, W. L., Bos, F. P., Schipper, H. R., Lowke, D., Hack, N., ... & Roussel, N. (2020). A process classification framework for defining and describing Digital Fabrication with Concrete. Cement and Concrete Research, 134, 106068.

Buswell, R. A., Soar, R., Gibb, A., & Thorpe, A. (2005). The potential of freeform construction processes.

Buswell, R. A., De Silva, W. L., Jones, S. Z., & Dirrenberger, J. (2018). 3D printing using concrete extrusion: A roadmap for research. Cement and concrete research, 112, 37-49.

Chen, H., Zhang, D., Chen, P., Li, N., & Perrot, A. (2023). A review of the extruder system design for large-scale extrusion-based 3D concrete printing. Materials, 16(7), 2661.

Costanzi, C. B., Ahmed, Z. Y., Schipper, H. R., Bos, F. P., Knaack, U., & Wolfs, R. J. M. (2018). 3D Printing Concrete on temporary surfaces: The design and fabrication of a concrete shell structure. Automation in construction, 94, 395-404.

Delta System. (2020). Delta WASP 3MT CONCRETE. Retrieved from https://www.3dwasp.com/stampante-3d-cemento-delta-wasp-3mt-concrete/

Dey, D., Van, V. N., Xuan, H. N., Srinivas, D., Panda, B., & Tran, P. (2023). Flexural performance of 3D printed concrete structure with lattice infills. Developments in the Built Environment, 16, 100297.

Diggs-McGee, B. N., Kreiger, E. L., Kreiger, M. A., & Case, M. P. (2019). Print time vs. elapsed time: A temporal analysis of a continuous printing operation for additive constructed concrete. Additive Manufacturing, 28, 205-214.

Dolen, M., & Yaman, U. (2014). New morphological methods to generate two-dimensional curve offsets. The International Journal of Advanced Manufacturing Technology, 71(9), 1687-1700.

Duarte, G., Duarte, J. P., Memari, A., Brown, N., & Gevaudan, J. P. (2023). Towards a model for structural performance in concrete printing based on buildability and toolpath design. Journal of Building Engineering, 69, 106325.

Dunlavey, M. R. (1983). Efficient polygon-filling algorithms for raster displays. ACM Transactions on Graphics (Tog), 2(4), 264-273.

Feng, P., Meng, X., Chen, J. F., & Ye, L. (2015). Mechanical properties of structures 3D printed with cementitious powders. Construction and Building Materials, 93, 486-497.

Foust, M., Thomsen, D., Stickles, R., Cooper, C., & Dodds, W. (2012). Development of the GE aviation low emissions TAPS combustor for next-generation aircraft engines. In 50th AIAA aerospace sciences meeting including the new horizons forum and aerospace exposition (p. 936).

Gamage, K., Fawzia, S., Zahra, T., Teixeira, M. B. F., & Ramli Sulong, N. H. (2024). Advancement in sustainable 3D concrete printing: A review on materials, challenges, and current progress in Australia. Buildings, 14(2), 494.

Gantry Printer. (2021). Sustainable Resources for Additive Manufacturing Laboratory. Retrieved from https://iitg.ac.in/mech/research/facilities/3d-concrete-printing/

Gibson, I., Rosen, D., Stucker, B., Khorasani, M., Rosen, D., Stucker, B., & Khorasani, M. (2021). Additive manufacturing technologies (Vol. 17, pp. 160-186). Cham, Switzerland: Springer.

Gonçalves, F. A., Fonseca, A. C., Domingos, M., Gloria, A., Serra, A. C., & Coelho, J. F. (2017). The potential of unsaturated polyesters in biomedicine and tissue engineering: Synthesis, structure-properties relationships and additive manufacturing. Progress in Polymer Science, 68, 1-34.

Gosselin, C., Duballet, R., Roux, P., Gaudillière, N., Dirrenberger, J., & Morel, P. (2016). Large-scale 3D printing of ultra-high performance concrete–a new processing route for architects and builders. Materials & Design, 100, 102-109.

Helsgaun, K. (2000). An effective implementation of the Lin–Kernighan traveling salesman heuristic. European journal of operational research, 126(1), 106-130.

Hernández Vargas, J. (2023). Design for 3D Concrete Printing: Optimisation Through Integrated Workflows (Doctoral dissertation, KTH Royal Institute of Technology).

Hwang, D., & Khoshnevis, B. (2005). An innovative construction process-contour crafting (CC). In Proceedings of the International Symposium on Automation and Robotics in Construction (IAARC). International Association for Automation and Robotics in Construction (IAARC).

Hybrid system. (2019). Students' 3D-printed Concrete Choreography pillars provide a stage for dancers. Retrieved from https://www.dezeen.com/2019/07/24/3d-printed-concrete-choreography-pillars-design/

Hyperion robotics. (2021). Foundations built smarter. Retrieved from https://www.hyperionrobotics.com/product-catalogue/foundations/

Jin, Y., He, Y., Fu, G., Zhang, A., & Du, J. (2017). A non-retraction path planning approach for extrusion-based additive manufacturing. Robotics and Computer-Integrated Manufacturing, 48, 132–144.

Jin, Y. A., He, Y., Fu, J. Z., Gan, W. F., & Lin, Z. W. (2014). Optimization of tool-path generation for material extrusion-based additive manufacturing technology. Additive manufacturing, 1, 32-47.

Kapil, S., Joshi, P., Yagani, H. V., Rana, D., Kulkarni, P. M., Kumar, R., & Karunakaran, K. P. (2016). Optimal space filling for additive manufacturing. Rapid Prototyping Journal, 22(4), 660–675.

Keating, S. J., Leland, J. C., Cai, L., & Oxman, N. (2017). Toward site-specific and self-sufficient robotic fabrication on architectural scales. Science robotics, 2(5), eaam8986.

Khoshnevis, B. (2004). Automated construction by contour crafting—related robotics and information technologies. Automation in construction, 13(1), 5-19.

Khoshnevis, B., Hwang, D., Yao, K. T., & Yeh, Z. (2006). Mega-scale fabrication by contour crafting. International Journal of Industrial and Systems Engineering, 1(3), 301-320.

Kim, T. K., Nguyen, D. C., & Shim, C. S. (2023, March). Digital Fabrication for DfMA of a Prefabricated Bridge Pier. In Proceedings of The 17th East Asian-Pacific Conference on

Structural Engineering and Construction, 2022: EASEC-17, Singapore (pp. 305-310). Singapore: Springer Nature Singapore.

Kloft, H., Gehlen, C., Dörfler, K., Hack, N., Henke, K., Lowke, D., ... & Raatz, A. (2021). TRR 277: Additive manufacturing in construction. Civil Engineering Design, 3(4), 113-122.

Laovisutthichai, V., Lu, W., & Low, S. P. (2025). Design for excellence (DfX) for high-rise modular buildings: from DfX considerations to module design guidelines using the case of Hong Kong. Architectural Engineering and Design Management, 21(3), 430-449.

Le, T. T., Austin, S. A., Lim, S., Buswell, R. A., Law, R., Gibb, A. G., & Thorpe, T. (2012). Hardened properties of high-performance printing concrete. Cement and concrete research, 42(3), 558-566.

Leschok, M., Cheibas, I., Piccioni, V., Seshadri, B., Schlüter, A., Gramazio, F., ... & Dillenburger, B. (2023). 3D printing facades: Design, fabrication, and assessment methods. Automation in Construction, 152, 104918.

Lim, J. H., Weng, Y., & Pham, Q. C. (2020). 3D printing of curved concrete surfaces using adaptable membrane formwork. Construction and Building Materials, 232, 117075.

Lim, S., Buswell, R. A., Le, T. T., Austin, S. A., Gibb, A. G., & Thorpe, T. (2012). Developments in construction-scale additive manufacturing processes. Automation in construction, 21, 262-268.

Lin, X. T., Xu, S., & Chen, X. (2025). Optimization of building structures based on additive manufacturing: A review. Journal of Building Engineering, 113813.

Lin, Z., Fu, J., Shen, H., Gan, W., & Yue, S. (2015). Tool path generation for multi-axis freeform surface finishing with the LKH TSP solver. Computer-Aided Design, 69, 51-61.

Liu, J., Nguyen-Van, V., Panda, B., Fox, K., du Plessis, A., & Tran, P. (2022). Additive manufacturing of sustainable construction materials and form-finding structures: a review on recent progresses. 3D Printing and Additive Manufacturing, 9(1), 12-34.

Liu, Z., Wang, Y., Wu, B., Cui, C., Guo, Y., & Yan, C. (2019). A critical review of fused deposition modeling 3D printing technology in manufacturing polylactic acid parts. The International Journal of Advanced Manufacturing Technology, 102(9), 2877-2889.

Loughborough University. (2025, July). Concrete 3D printed canopy. Retrieved from https://www.lboro.ac.uk/research/beyond3dcp/the-canopy/

Loughborough University. (2011). Beyond 3D concrete printing. Retrieved from https://www.lboro.ac.uk/research/beyond3dcp/about/

Lowke, D., Anton, A., Buswell, R., Jenny, S. E., Flatt, R. J., Fritschi, E. L., ... & Kloft, H. (2024). Digital fabrication with concrete beyond horizontal planar layers. Cement and Concrete Research, 186, 107663.)

Malaeb, Z., AlSakka, F., & Hamzeh, F. (2019). 3D concrete printing: machine design, mix proportioning, and mix comparison between different machine setups. In 3D Concrete printing technology (pp. 115-136). Butterworth-Heinemann.

Mata Falcón, J., Gebhard, L., Lee, M., & Bischof, P. (2023). Advances in Structural Applications of Digital Fabrication With Concrete. Visions and Strategies for Reinforcing Additively Manufactured Constructions 2023, 3.

Mechtcherine, V., Nerella, V. N., Will, F., Näther, M., Otto, J., & Krause, M. (2019). Large-scale digital concrete construction–CONPrint3D concept for on-site, monolithic 3D-printing. Automation in construction, 107, 102933.

Mechtcherine, V., Bos, F. P., Perrot, A., Da Silva, W. L., Nerella, V. N., Fataei, S., ... & Roussel, N. (2020). Extrusion-based additive manufacturing with cement-based materials–production steps, processes, and their underlying physics: a review. Cement and Concrete Research, 132, 106037.

Mohammad, M., Masad, E., & Al-Ghamdi, S. G. (2020). 3D concrete printing sustainability: a comparative life cycle assessment of four construction method scenarios. Buildings, 10(12), 245.

Montali, J., Overend, M., Pelken, P. M., & Sauchelli, M. (2018). Knowledge-Based Engineering in the design for manufacture of prefabricated façades: current gaps and future trends. Architectural Engineering and Design Management, 14(1-2), 78-94.

Murcia, D. H., Genedy, M., & Taha, M. R. (2020). Examining the significance of infill printing pattern on the anisotropy of 3D printed concrete. Construction and Building Materials, 262, 120559.

Murr, L. E., Gaytan, S. M., Medina, F., Lopez, H., Martinez, E., Machado, B. I., ... & Bracke, J. (2010). Next-generation biomedical implants using additive manufacturing of complex, cellular and functional mesh arrays. Philosophical Transactions of the Royal Society A: Mathematical, Physical and Engineering Sciences, 368(1917), 1999-2032.

NC Viewer. (2025). Retrieved from https://ncviewer.com/

Nerella, V. N., & Mechtcherine, V. (2019). Studying the printability of fresh concrete for formwork-free concrete onsite 3D printing technology (CONPrint3D). In 3D concrete printing technology (pp. 333-347). Butterworth-Heinemann.

Nguyen, D. C., Park, S. J., & Shim, C. S. (2022). Digital engineering models for prefabricated bridge piers. Smart Struct. Syst, 30(1), 35-47.

Omrani, S., & Iordanova, I. (2023). A conceptual framework for design for adaptability based on modularity, DfMA, digital design, and fabrication. In Canadian Society of Civil Engineering Annual Conference (pp. 189-202). Cham: Springer Nature Switzerland.

Pajonk, A., Prieto, A., Blum, U., & Knaack, U. (2022). Multi-material additive manufacturing in architecture and construction: A review. Journal of Building Engineering, 45, 103603.

Park, S. C., & Choi, B. K. (2000). Tool-path planning for direction-parallel area milling. Computer-Aided Design, 32(1), 17–25.

Prasittisopin, L. (2024). How 3D printing technology makes cities smarter: a review, thematic analysis, and perspectives. Smart Cities, 7(6), 3458-3488.

Leal, R., Barreiros, F. M., Alves, L., Romeiro, F., Vasco, J. C., Santos, M., & Marto, C. (2017). Additive manufacturing tooling for the automotive industry. The International Journal of Advanced Manufacturing Technology, 92(5), 1671-1676.

Rajan, V. T., Srinivasan, V., & Tarabanis, K. A. (2001). The optimal zigzag direction for filling a two-dimensional region. Rapid Prototyping Journal, 7(5), 231–241.

Raphael, B., Senthilnathan, S., Patel, A., & Bhat, S. (2023). A review of concrete 3D printed structural members. Frontiers in Built Environment, 8, 1034020.

Ren, F., Sun, Y., & Guo, D. (2009). Combined reparameterization-based spiral toolpath generation for five-axis sculptured surface machining. The international journal of advanced manufacturing technology, 40(7), 760-768.

Robotic system. (2017). DuBox to showcase the first 3D printed concrete element in the UAE. Retrieved from https://www.dubox.me/dubox-showcase-first-3d-printed-concrete-element-uae/

Sadakorn, W., Prasertsuk, S., & Prasittisopin, L. (2022). 3D Cement Printing: DFMA Guideline of Patterned Load-Bearing Walls for Small Residential Units. In International Conference on Civil Engineering and Architecture (pp. 19-28). Singapore: Springer Nature Singapore.

Sadakorn, W., Prasertsuk, S., & Prasittisopin, L. (2024). Improving the structural efficiency of textured three-dimensional concrete printing wall by architectural design. Frontiers of Structural and Civil Engineering, 18(5), 699-715.

Sahu, A., & Panda, B. (2025). A TSP-based continuous path planning for additive manufacturing of concrete. Progress in Additive Manufacturing, 10(4), 2205-2226.

Sai, G. M., & Aravindan, A. (2020). A comparative study on newly emerging type of formwork systems with conventional type of form work systems. Materials Today: Proceedings, 33, 736-740.

Schipper, R., Costanzi, C. B., Bos, F., Ahmed, Z., & Wolfs, R. (2017). Double curved concrete printing: printing on non-planar surfaces. SPOOL, 4(2), 17-21.

Sevcik, M. J., Golson, J., Bjerke, G., Snyder, I., Taylor, G., Wilson, F., ... & Eliasson, V. (2024). Dual feed progressive cavity pump extrusion system for functionally graded direct ink write 3D printing. HardwareX, 17, e00515.

Shakor, P., Nejadi, S., Paul, G., & Malek, S. (2019). Review of emerging additive manufacturing technologies in 3D printing of cementitious materials in the construction industry. Frontiers in Built Environment, 4, 85.

Shapely User Manual — Shapely 1. 8.1. post1 documentation, (n.d.). Retrieved from https://shapely.readthedocs.io/en/stable/manual.html

Shin, Y., Kim, T., Cho, H., & Kang, K. I. (2012). A formwork method selection model based on boosted decision trees in tall building construction. Automation in Construction, 23, 47-54.

Sika Group. (2025). Contoured components. Retrieved from https://www.sika.com/en/knowledge-hub/3d-concrete-printing.html

Singh, S., Singh, A., Kapil, S., & Das, M. (2022). Utilization of a TSP solver for generating non-retractable, direction favouring toolpath for additive manufacturing. Additive Manufacturing, 59, 103126.

Singh, S., Singh, A., Kapil, S., & Das, M. (2024). Generation of continuous and sparse space filling toolpath with tailored density for additive manufacturing of biomimetics. Computer-Aided Design, 173, 103718.

Spool. (2017). Double curved concrete printing. Retrieved from https://spool.ac/index.php/spool/article/view/59

Srinivas, D., Ventrapragada, D. P., Panda, B., & Sitharam, T. G. (2025). A study on the effect of mixture constituents on washout resistance, mechanical, and transport properties in the context of underwater 3D concrete printing. Journal of Sustainable Cement-Based Materials, 14(3), 446-465.

Steuben, J. C., Iliopoulos, A. P., & Michopoulos, J. G. (2016). Implicit slicing for functionally tailored additive manufacturing. Computer-Aided Design, 77, 107-119.

Sunil Bhandari. (2025). slice_stl_create_path(triangles,slice_height), MATLAB Central File Exchange, Retrieved from https://www.mathworks.com/matlabcentral/fileexchange/62113-slice_stl_create_path-triangles-slice_height

Takva, Ç., Top, S. M., Gökgöz, B. İ., Gebel, Ş., İlerisoy, Z. Y., İlcan, H., & Şahmaran, M. (2024). Applicability of 3D concrete printing technology in building construction with different architectural design decisions in housing. Journal of Building Engineering, 98, 111257.

Traveling Salesman Problem, (n. d.). Retrieved from http://www.math.uwaterloo.ca/tsp/index.html

Tuvayanond, W., & Prasittisopin, L. (2023). Design for manufacture and assembly of digital fabrication and additive manufacturing in construction: a review. Buildings, 13(2), 429.

Vantyghem, G., De Corte, W., Shakour, E., & Amir, O. (2020). 3D printing of a post-tensioned concrete girder designed by topology optimization. Automation in Construction, 112, 103084.

Vertico. (2023). Hexastone. Retrieved from https://www.vertico.com/projects/hexastone

Vertico. (2025). The Future of 3D Printed Facades: How Concrete Printing is Transforming Architecture. Retrieved from https://www.vertico.com/wiki/3d-printed-facades-architecture

Vertico. (2023). Facades. Retrieved from https://www.vertico.com/projects/sand-mould-facades

Wan, Q., Wang, L., & Ma, G. (2020). Adaptable tool-path planning method for 3D concrete printing based on the mapping method. In Proceedings of the International Conference on Computational Design and Robotic Fabrication (pp. 255–264). Springer, Singapore.

Wan, Q., Wang, L., & Ma, G. (2022). Continuous and adaptable printing path based on transfinite mapping for 3D concrete printing. Automation in Construction, 142, 104471.

Wang, H., Jang, P., & Stori, J. A. (2005). A metric-based approach to two-dimensional (2D) tool-path optimization for high-speed machining. Journal of Manufacturing Science and Engineering, 127(1), 33–48.

Wei, Y., Han, S., Chen, Z., Lu, J., Li, Z., Yu, S., ... & Yan, P. (2024). Numerical simulation of 3D concrete printing derived from printer head and printing process. Journal of Building Engineering, 88, 109241.

Weng, Y., Mohamed, N.A.N., Lee, B.J.S., Gan, N.J.H., Li, M., Jen Tan, M., Li, H. and Qian, S. (2021), Extracting BIM information for lattice toolpath planning in digital concrete printing with developed dynamo script: A case study, Journal of Computing in Civil Engineering, Vol. 35 No. 3, p. 05021001.

Wu, H., Li, Z. I. Y. A. N., Zhou, X. I. N. J. I. E., Wu, X. I. N. Y. U., Bao, D. I. N. G. W. E. N., & Yuan, P. F. (2022). Digital design and fabrication of a 3D concrete printed funicular spatial structure. In Proceedings of the 27th International Conference of the Association for Computer-Aided Architectural Design Research in Asia (pp. 71-80).

Wu, P., Wang, J. and Wang, X. (2016), A critical review of the use of 3-D printing in the construction industry, Automation in Construction, Vol. 68, pp. 21-31.

Xiao, J., Ji, G., Zhang, Y., Ma, G., Mechtcherine, V., Pan, J., ... & Du, S. (2021). Large-scale 3D printing concrete technology: Current status and future opportunities. Cement and Concrete Composites, 122, 104115.

XtreeE. (2017). Krypton, a column in Aix-en-Provence. Retrieved from https://www.xtreee.com/uses-cases/krypton%2C-a-column-in-aix-en-provence

XtreeE. (2018). The X-Reef welcomes its first dwellers. Retrieved from https://www.xtreee.com/news/news-title-01

XtreeE. (2025). The Large-Scale 3D Printing. Retrieved from https://xtreee.com/

Xu, J., Buswell, R. A., Kinnell, P., Biro, I., Hodgson, J., Konstantinidis, N., & Ding, L. (2020). Inspecting manufacturing precision of 3D printed concrete parts based on geometric dimensioning and tolerancing. Automation in Construction, 117, 103233.

Xu, J., Ding, L., Love, P. E. D., & Li, H. (2015). Digital reproduction of historical building ornamental components: From 3D scanning to 3D printing. Automation in Construction, 76, 85–96.

Yabanigül, M. N., & Gulec Ozer, D. (2024). Exploring Architectural Units Through Robotic 3D Concrete Printing of Space-Filling Geometries. Buildings, 15(1), 60.

Ye, J., Cui, C., Yu, J., Yu, K., & Dong, F. (2021). Effect of polyethylene fiber content on workability and mechanical-anisotropic properties of 3D printed ultra-high ductile concrete. Construction and Building Materials, 281, 122586.

Zaid, O., & El Ouni, M. H. (2024). Advancements in 3D printing of cementitious materials: A review of mineral additives, properties, and systematic developments. Construction and Building Materials, 427, 136254.

Zareiyan, B., & Khoshnevis, B. (2017). Effects of interlocking on interlayer adhesion and strength of structures in 3D printing of concrete. Automation in Construction, 83, 212-221.

Zhang, J. (2009). Contour crafting process planning and optimization (Doctoral dissertation, University of Southern California).

Zhang, N., & Sanjayan, J. (2025). Concrete 3D printing and digital fabrication technologies for bridge construction. Automation in Construction, 179, 106485.

Zhao, H., Gu, F., Huang, Q. X., Garcia, J., Chen, Y., Tu, C., Benes, B., Zhang, H., Cohen-Or, D., & Chen, B. (2016). Connected Fermat spirals for layered fabrication. ACM Transactions on Graphics (TOG), 35(4), 1–10.

Publications

Journals

[1] **Sahu, A.**, & Panda, B., (2025). A TSP-based continuous path planning for additive manufacturing of concrete. *Progress in Additive Manufacturing*, *10*(4), 2205-2226. https://doi.org/10.1007/s40964-024-00746-2

[2] **Sahu, A.**, & Panda, B., (2025). An additive manufacturing-oriented design approach for digital construction. *Rapid Prototyping Journal.* https://doi.org/10.1108/RPJ-04-2025-0159

[3] **Sahu, A.**, & Panda, B., (2026). Growth curve-based continuous toolpath for improving the performance of the additively manufactured concrete. *Progress in Additive Manufacturing* https://doi.org/10.1007/s40964-025-01515-5

[4] **Sahu, A.**, Panda, B., & Ror, C.K., (2026). Utilization of a growth curve-based strategy for generating non-retractable and non-planar toolpath for additive manufacturing of concrete. *CIRP Journal of Manufacturing Science and Technology.* **(Submitted)**

Conferences, Posters, and Book chapters

[1] **Sahu, A.**, Panda, B., Dey, D., & Dodda, S., (2022). Trajectory Planning for Additive Manufacturing of Concrete, *12th International Conference on Precision, Meso, Micro, and Nano Engineering, IIT Kanpur. (Poster)*

[2] Dey, D., **Sahu, A.**, Prakash, S., & Panda, B., (2023). A study into the effect of material deposition methods on hardened properties of 3D printed concrete. *Materials Today: Proceedings. (Book chapter)*

[3] **Sahu, A.**, Akshay, M., & Panda, B., (2024). A Design for Additive Manufacturing (DfAM) Method for Modular Concrete 3D Printing. *ICGNT 2024, IIT Madras, International Conference on next generation technologies: design and manufacturing (Poster)*

[4] **Sahu, A.**, Sharma, D., & Panda, B., (2025). Tailoring Topology-Optimized Lightweight Concrete Beam Design for Additive Manufacturing. *ICoRD 2025, IIT Hyderabad. Lecture Notes in Mechanical Engineering. Springer, Singapore. (Book chapter)*